POLITECNICO DI TORINO

Collegio di Ingegneria Energetica

Master of Science Course
in Energy and Nuclear Engineering

Master of Science Thesis

Multiphysics model of a novel high-temperature solid oxide battery system with integrated phase-change material for heat storage

Candidate: Francesca Angeletti,

Matricola: 232138

Tutor: Massimo Santarelli

Supervisors: Christopher Graves, Maria Navasa, Henrik Lund Fransen

(Technical University of Denmark)

April 2018

Abstract

There is a rapidly growing need to balance the consumption of electricity and its production from renewable energy sources, since the power demand rarely coincides with the power generation. Therefore electricity storage technologies have been highly studied during the last decades. One recently proposed, promising storage technology is an iron-air battery that utilizes a reversible solid oxide electrochemical cell (RSOC) coupled with iron as a thermochemical storage medium, which operates at ~700 °C.

The main goal of the project is to model the heat management of a high temperature solid oxide iron air redox battery and use the model to design a novel battery system that integrates a phase-change material (PCM) to provide latent heat storage and improve the round-trip efficiency of this type of battery. The model has been built with the software COMSOL Multiphysics using a three-dimensional geometry with fluid flow and heat transfer physics implemented. The model has been solved with finite element methods (FEM). The model was used to design a compact system in an insulated box that includes a heat exchanger, a phase change material and the RSOC stack. Therefore, the balance of plant is minimized, integrating the thermal storage in direct contact with the stack and using a simple heat exchanger.

Firstly, a simpler model was designed using a heater instead of the PCM, in order to obtain a baseline configuration in steady state conditions that could manage the heat fluxes both modes of operation, exothermic discharge (fuel-cell) mode and endothermic charge (electrolysis) mode. Afterwards, the PCM was added to recover the heat released in discharge operation and to use it in charge, and this system was studied using a time-dependent solution.

By using the PCM instead of the heater, the round-trip efficiency increased from 58% to 83% at low current density operating conditions. At higher current density conditions the integration of the PCM does not enhance the efficiency significantly (61.7% with PCM and 57.8% with the heater) because the charge mode is nearly isothermal and cannot utilize the stored heat. Moreover, with the PCM the oxygen overblow factor could be eliminated, which otherwise needed to be 40 times higher to provide cooling during exothermic operation.

Eventually, the amount of Iron and of Aluminum that is needed per hour of storage capacity has been analyzed, and the amount of Aluminum is much greater than that of the Iron, e.g. in order to have 3 hours of storage capacity, 3.3 kg of Iron are needed and 12.5 kg of Aluminum. Regarding the cost of the material per kWh of storage capacity, the Aluminum is higher than Iron, e.g. in order to store 3 kWh the Aluminum costs 35 $ and the Iron 3 $, therefore the cost of the electrical storage medium is almost negligible compared to that of the Aluminum.

Acknowledgements

This thesis concludes my Master degree in Energy and Nuclear Engineering, and it is the product of five months spent at the Technical University of Denmark, more precisely, at the Risø Campus in Roskilde, at the Department of Energy Conversion and Storage.

First of all, I would like to thank all my passionate supervisors: Christopher Graves, who accepted my request for this project and guided me with his teachings through all this path; Maria Navasa, whose door was always open whenever I was in trouble or had a question; Henrik Lund Fransen, for his advice and help; and of course thanks to Professor Massimo Santarelli, my tutor in Politecnico di Torino, who gave me the opportunity to go abroad.
I would like to thank all the people that I met in Risø, who made great this experience, and among them a special thanks to Andrea, Corrado and Mohamad.

Thanks to Rodolfo, my boyfriend, who is always there if I have a problem and gives me support and encouragement. Thanks to Sara, Russo and Zilio for their company and the best support for over 10 years. Thanks to my friends who have shared with me the engineering path, Francesca, Stefania, Marco and Ettore from the very beginning. Thanks to all my friends Andrea, Simone, Levri, Audi, Maria, Ludovico, and Brogna.

Eventually, I would like to thank my family, especially my parents and my sister, for always supporting me, encouraging me through my years of study, and for making this experience possible.

Nomenclature

A	Area $[m^2]$
AU	Air utilization $[-]$
C	Specific heat $[J/kg/K]$
c_p	Heat capacity at a constant pressure $[J/K/kg]$
D_h	Hydraulic diameter $[m]$
d_{in}	Diameter of the inner pipe $[m]$
D_{out}	Diameter of the outer pipe $[m]$
F	Faraday's constant, 96485.3 $[C/mol]$;
ΔG	Gibbs free energy difference $[J]$
Δg	Molar Gibbs free energy difference $[J/mol]$
h_{conv}	Convective heat transfer coefficient $[W/(m^2 \cdot K)]$
ΔH	Enthalpy difference $[J]$
Δh	Molar enthalpy difference $[J/mol]$
h_{cell}	Height of the cell $[m]$
h_{stack}	Height of the stack $[m]$
I	Faraday current $[A]$
i	Current density $[A/cm^2]$
k	thermal conductivity $[W/(m \cdot K)]$
L	Length of the pipe $[m]$
Q_{latent}	Specific latent heat of the phase change $[J/kg]$
m	Mass $[kg]$
$\dot{m}$	Mass flow rate $[kg/s]$
$\dot{n}$	Molar flow rate $[mol/s]$
$ncell$	Number of cells $[-]$
Nu	Nusselt number $[-]$
P	Electrical power $[W]$
p_i	Partial pressure of the specie in $[Pa]$
Pr	Prandtl number $[-]$
Q	Heat source $[W]$
$\bar{R}$	Universal gas constant $[J/(mol \cdot K)]$
Re	Reynolds number $[-]$

S	Base surface area of the stack $[m^2]$
ΔS	Entropy difference $[J]$
Δs	Molar entropy difference $[J/mol]$
T	Temperature $[K]$
t	Time $[s]$
T_f	Temperature of the phase transition $[K]$
ΔT_{ml}	Logarithmic mean temperature difference $[K]$
th	Thickness of the pipe $[m]$
U	Thermal transmittance $\left[\frac{W}{m^2 K}\right]$
u	Velocity of the flow $[m/s]$
V	Cell voltage $[V]$
V_{tn}	Thermoneutral voltage $[V]$
W	Work $[J]$
z	Number of electrons exchanged in the reaction $[-]$

Greek Symbols

ε	Porosity $[-]$
$\eta_{activation}$	Activation overpotential $[V]$
$\eta_{diffusion}$	Diffusion overpotential $[V]$
η_{ohmic}	Ohmic overpotential $[V]$
θ	Fraction of the phase transition $[-]$
κ	Permeability $[m^2]$
μ	Dynamic viscosity of the fluid $[Pa \cdot s]$
ν_i	Generic stoichiometric coefficient $[-]$
ρ	Density $[\frac{kg}{m^3}]$
ϕ	Heat $[J]$

Subscript

c	Cold
el	Electric
eq	Equivalent

h	Hot
i	Index for the species
in	Inlet- inner
irr	Irreversible
l	Liquid state
out	Outlet- outer
ph	Phase transition
$react$	Reaction
s	Solid state
SS	Stainless-Steel
th	Thermal

Acronyms

ASR	Area specific resistance
EL	Electrolysis
FC	Fuel cell
OCV	Open circuit voltage
PCM	Phase change material
RCU	Redox circuit unit
RES	Renewable energy sources
ROB	Rechargeable Oxide battery
RSOC	Reversible solid oxide cells
SOEC	Solid oxide electrolysis cell
SOFC	Solid oxide fuel cell
SOIARB	Solid oxide iron-air redox battery
TES	Thermal energy storage
TSU	Thermal storage unit
1D	One dimension
2D	Two dimensions
3D	Three dimensions

List of figures

List of tables

Table of Contents

1. INTRODUCTION

1.1 Description of the project

In order to mitigate carbon dioxide emissions, a reduction on the dependency on oil, natural gas and fossil fuel must be accomplished. The best solution to achieve this goal should be a reduction of the consumption of energy, energy efficiency improvement and a greater exploitation of the renewable energy sources.

The main issue related to many renewable energy sources (RES), such as wind and solar, is their intermittent nature. In fact, the power produced is subject to daily and seasonal fluctuations, which lead to a grid's stability problem. This will result in discrepancies between power produced by RES-based energy systems and requested power from the load, which means there will be periods of over-production of energy from RES system, and periods of energy shortage of the users.

In order to reduce and control this negative effect, improved network management in terms of transmission capacity and an improvement in storage capacity are needed.

For this reason, the development of a large-capacity electrical energy storage is very important for the realization of a smart grid based on a significant fraction of intermittent RES.

One recently proposed promising energy storage technology, is an Iron-air rechargeable battery that consists of a reversible solid oxide cell (RSOC) coupled to iron as a redox medium, wherein two reactions occur: an electrochemical one at the RSOC, and a thermochemical one at the metal.

RSOCs are electrochemical devices used for energy conversion. The main advantage of this cells is that it is possible to work both as electrical energy producer (fuel cell mode) and as fuel producer (electrolysis mode), therefore it can be used as electrical storage. In electrolysis mode (SOEC), the electrical energy from renewable sources is supplied to split H_2O and/or CO_2 molecules into H_2 and/or CO with very high efficiency. These products can be converted into hydrocarbons and then exploited in industrial processes, or can be reutilized in the RSOC in fuel cell mode (SOFC) to convert back into electrical energy on demand from the chemical energy of H_2 and/or CO.

Then the system provides reversible electricity storage like an open system rechargeable battery, but if it is possible to make it a closed system, like a battery, it would simplify the balance of plant of the system.

Usually, the RSOCs are powered by high purity pre-heated gases, and when the electrolysis produces hydrogen, it should be further processed or synthesized to be stored, increasing the cost of the system and decreasing the efficiency. Moreover, the roundtrip energy storage efficiency of H_2O to H_2 and H_2 to H_2O is not very high and limited by thermodynamics to 70-80%, and around 50% in a practical system.

One interesting closed system is the solid oxide Iron-air redox battery (SOIARB), in which a RSOC is integrated with Fe/FeO. The Iron redox material is a porous structure with high surface area, and it is the electrical storage medium. By integrating the Iron with the RSOC, the hydrogen and the steam can flow in a closed system to reduce and oxidize FeO/Fe and there is no need to supply or remove the gases. Moreover, there is no need to capture and store the hydrogen.

This typology of battery could be attractive because of the following reasons: the cost is reduced because less complex balance of plant is needed, since it works with a mixture of steam and hydrogen in contact with a storage material, it does not require a supply of fuel gas; it is a clean and pollution free technology, it has high energy storage capacity.

However, this type of battery has some drawbacks: the roundtrip efficiency is the same as the H_2O/H_2 system and most system designs involve a still rather complex balance of plant. For these reasons, in this thesis, a compact system which integrates a phase change material (PCM) for latent heat storage has been designed. The system built in this project is an insulated box that consists of a heat exchanger, the RSOC stack, and the PCM. In the first design, a simple heater was implemented instead of the PCM, in order to study the best configuration in terms of geometry and operating conditions for both the operating modes (fuel cell and electrolysis). So the final design was a tradeoff of the two modes, in fact, in electrolysis the aim was to keep the heat inside the system, in fuel cell mode the goal was to shed the heat in order to not overheat the stack.
Afterwards, the PCM was added instead of the heater in order to store the heat in excess during fuel cell mode, and then use it during electrolysis mode, and consequently to improve the round-trip efficiency.

1.2 Aim of the work

The aim of this thesis is to improve the thermal management of the SOIARB by making it more isothermal and avoiding thermal cycles during idle periods. This is achieved by integrating a PCM with the RSOC.

The PCM is a thermal energy storage of latent heat, and it should improve the round-trip efficiency because it would absorb the heat released from the stack during the exothermic fuel cell mode; it would release this heat to maintain the temperature of operation during the idle period and to sustain the reaction, or part of it, during the endothermic electrolysis mode. Moreover, the system need a simpler balance of plant than is required without the PCM, which would make the system cheaper.

Achieving a high efficiency also requires that the heat generated by the RSOC stack and flowed out in the air exhaust must pre-heat the incoming air that should enter the stack. Therefore a heat exchanger has been designed to exploit the heat of the hot air leaving the stack.

Thus, the goal is to design a compact closed system able to control the thermal balance of the rechargeable oxide battery.

1.3 Literature review

The Iron-air redox battery is a rather new technology developed in the last few years, since 2011 several papers have been written on this new battery [1]–[8].

Different physics of the SOIARB have been studied. The gas diffusion and the mass transport were investigated, and it was found that the H_2-H_2O is very effective in transporting the oxygen between the RSOC and the Fe/FeO. Furthermore, the kinetics of the different reactions were considered, finding that the oxidation kinetics are much faster than the reduction ones and, when the kinetics of the two reactions (at RSOC and at the redox metal) are almost equal, the terminal voltage is constant. Instead when the redox reaction becomes slower the terminal voltage increases or decreases at the end of the operation, depending if it is in charge or discharge, which leads to limited performances. Moreover, other papers focused on the volume expansion of the redox metal during the discharge operation, concluding that it limits the redox reaction because it reduces the diffusion coefficient. Another important topic was how to

improve the round-trip efficiency, and the solution was to integrate a heat exchanger to pre-heat the inlet air and a thermal storage to recover heat. Moreover, an important point about heat transfer is that the heat released during discharge operation can exceed the cooling provided by air convection, so an enhancement of the air flow rate (overblow of air) is needed. Eventually, it has been analyzed the electrical storage medium as iron and its degrading properties [7], but also the Calcium-Iron has been studied as storage medium because more redox cycles are possible with less degradation [4].

The complete system in previous work [9] (Figure 1a), included a heat exchanger, a Solid oxide iron-air redox battery (SOIARB) and a thermal storage unit (TSU).

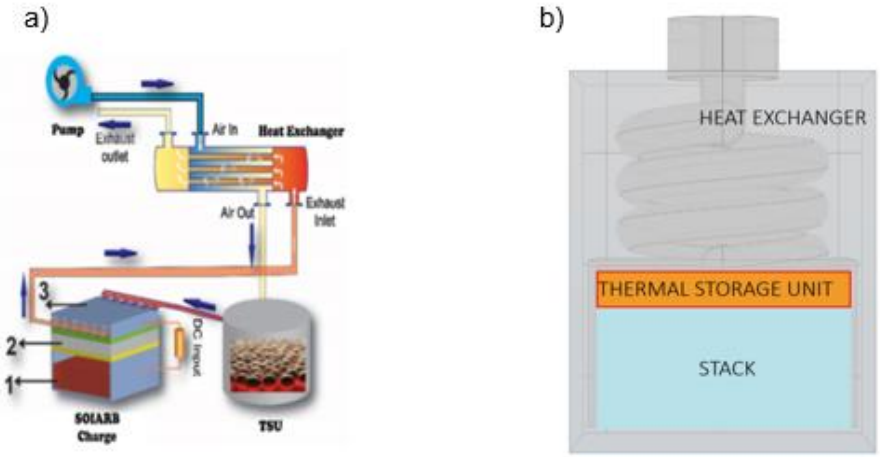

Figure 1 - The system scheme according to [9] (a) and the scheme of the model of this project (b).

The SOIARB system consists of the redox circuit unit (RCU) and the RSOC, and, in this project, they are treated as a single compact unit; the RCU is directly integrated in the solid oxide cell as it is explained in [4]. Moreover, in this project, a latent heat storage has been used, unlike the scheme in Figure 1a that is a rock-bed sensible heat storage. Furthermore, the thermal storage unit and the heat exchanger in the Figure 1a are physically separated from the redox battery and they are connected with pipes; instead, in this thesis, there is a single unit that includes all these components (Figure 1b), and this, as it is possible to notice in Figure 1, allows to reduce the balance of plant and to decrease the heat losses.

The main focus of this work is to study the direct integration of the thermal storage to the stack. In particular, it has been tried to build a single model that includes the heat exchanger, the SOIARB and the thermal storage, and then it has been studied the heat management of this model.

2. THEORETICAL BACKGROUND

2.1 Iron air redox battery

The solid oxide Iron-air redox battery (SOIARB) is a new battery concept which consists of a high temperature reversible solid oxide cell (RSOC) and iron as a redox metal. In this system, two reactions occur simultaneously in different locations, one at the RSOC and the other one at the metal.

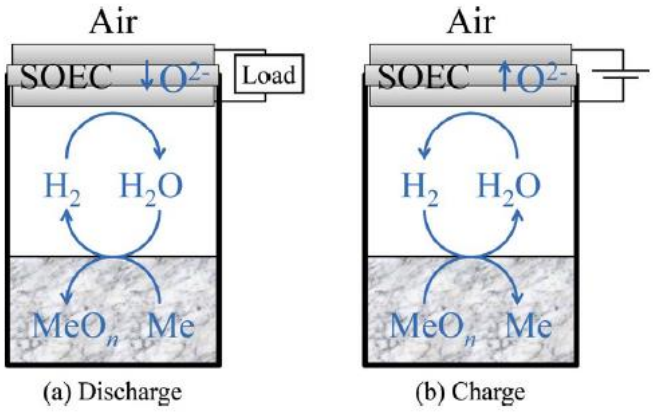

Figure 2 - Discharge (a) and Charge (b) operation in a SOIARB [1][2]

In Figure 2 the redox metal is symbolized as Me as a general metal, since the type of battery can also work with other metals besides Fe. The redox metal is usually made of fine metal particles in order to ensure a large surface area [1]. In this project the RCU is included in the flow channels inside the stack.

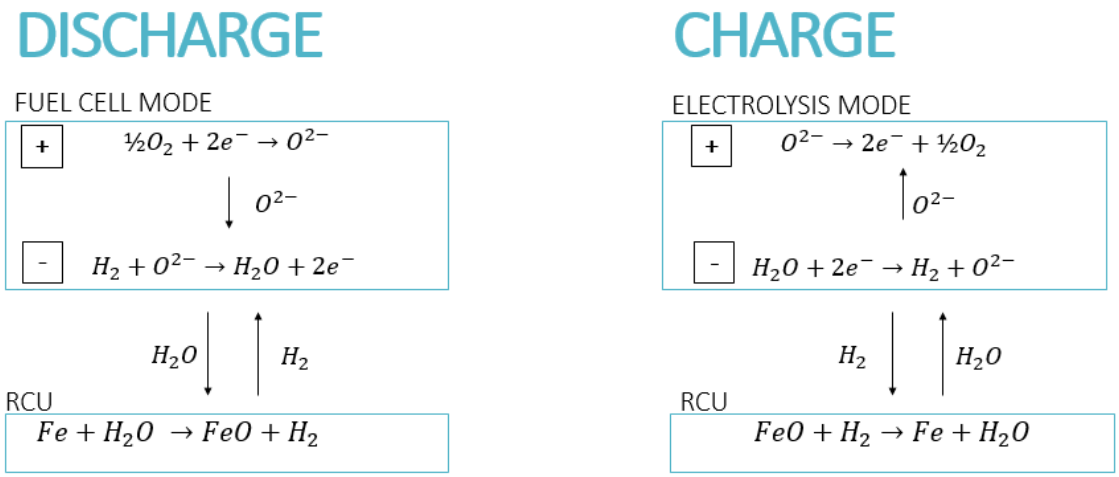

Figure 3 - A scheme of the coupling between the reactions in the redox metal and in the RSOC

As explained in Figure 3, in discharge operation, the RSOC works as fuel cell, the hydrogen is supplied to the SOFC, where steam is produced and transported to the redox metal that oxidizes; thus hydrogen is produced from the redox reaction and it diffuses to the SOFC where is consumed in an electrochemical reaction, and as a result electrical energy is produced [1]–[3] [6]–[10].

The air-electrode or positive-electrode is the cathode where oxygen reduction occurs and ions of oxygen are produced:

$$½O_2 + 2e^- \rightarrow O^{2-} \quad (1)$$

The ions pass through the electrolyte to the fuel-electrode or negative-electrode, which in this mode is the anode where oxidation occurs, and the ions react with hydrogen to produce steam:

$$H_2 + O^{2-} \rightarrow H_2O + 2e^- \quad (2)$$

The steam generated at the fuel-electrode diffuses to the redox metal and oxidizes it:

$$Me + nH_2O \rightarrow MeO_2 + nH_2 \quad (3)$$

This reaction produces hydrogen which is transported to the RSOC fuel-electrode by gas diffusion and it is used as fuel for electricity production.

The overall discharge reaction is therefore:

$$Me + \frac{n}{2}O_2 \rightarrow MeO_n \quad (4)$$

When the metal is totally oxidized the system needs to be recharged, so the reactions go in the opposite direction, which means in charge mode.

In charge operation the steam is supplied to the RSOC and hydrogen is produced consuming electrical energy, by gas diffusion it is transported to the RCU where the thermochemical redox reaction takes place; as a consequence the metal oxide is reduced to metal and the hydrogen is oxidized. The aim is to store energy, then the cell works in electrolysis mode. In this situation, the fuel-electrode is the cathode and the electrochemical reaction is expressed as follows:

$$H_2O + 2e^- \rightarrow H_2 + O^{2-} \quad (5)$$

The ions of oxygen migrate through the electrolyte towards the air-electrode or negative-electrode, which in this mode is the anode:

$$O^{2-} \rightarrow 2e^{-} + ½O_2 \tag{6}$$

The hydrogen generated at the fuel electrode diffuses towards the redox metal in order to reduce the metal oxide. Therefore, the steam behaves as an oxygen carrier, and it accelerates the reduction or the oxidation kinetics.

$$MeO_n + nH_2 \rightarrow Me + nH_2O \tag{7}$$

The total overall charge reaction is therefore:

$$MeO_n \rightarrow Me + \frac{n}{2}O_2 \tag{8}$$

When the metal oxide is totally reduced, the charge is complete.

In this project the Iron has been chosen as redox metal, therefore the thermochemical reaction in which the metal is oxidized becomes:

$$Fe + H_2O \underset{charge}{\overset{discharge}{\rightleftharpoons}} FeO + H_2 \tag{9}$$

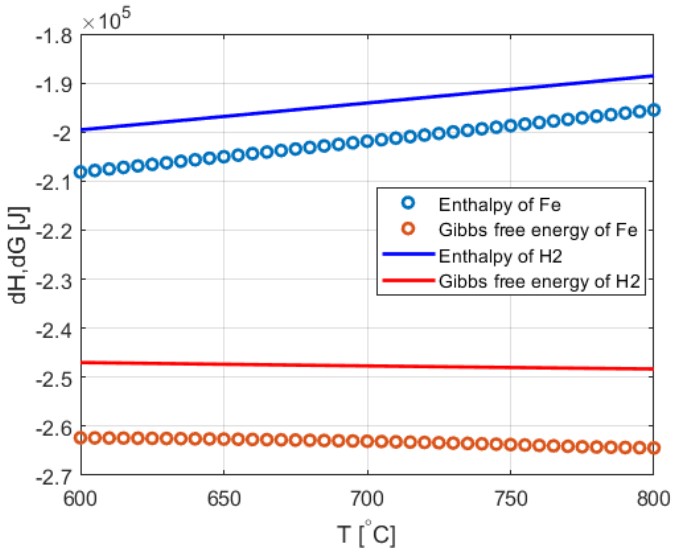

Figure 4 – Enthalpy and Gibbs free energy comparison between the reactions of oxidation of Iron and of hydrogen

In Figure 4, it is possible to see the enthalpy and the Gibbs free energy for the two reactions: Fe+½O2→ FeO and H2+½O2→H2O. The thermodynamic properties of the oxidation of the

hydrogen are always higher than those of the Iron, and they follow a similar trend such that the thermodynamic efficiencies of the two reactions are very similar.

2.2 Solid oxide cell

Reversible solid oxide cells (RSOCs) are electrochemical devices, used to directly convert chemical energy into electrical energy and vice versa, which ensure low irreversibility and high efficiency.

When the transformation of chemical energy into electrical energy occurs, the device is a power generator and it works in a galvanic regime. When it converts electrical energy into chemical energy, it becomes a producer of chemical species and it works in electrolysis mode.

An electrochemical cell is composed of two electrodes and an electrolyte layer. The anode is the electrode where the reaction of oxidation occurs:

$$R_1 \leftrightarrow O_x + e^- \tag{10}$$

The cathode is where the reduction reaction occurs:

$$R_2 + O_x + e^- \leftrightarrow P \tag{11}$$

The electrolyte layer physically separates anode and cathode and it is characterized by low molecular diffusivity, low capability to conduct electrons, and high capability to conduct ions. The reaction can occur even if there is no contact between the two reactants; this is possible thanks to the ions that travel across the electrolyte, and the electrons that travel in an external circuit.

The charge separation gives rise to a generation of an electrical field on both electrodes; therefore a voltage differential is created. By closing the external circuit, the equilibrium at the electrodes is broken and a current is generated by the flow of electrons.

The presence of a current flowing across a voltage gradient generates electrical power:

$$P = \Delta V \cdot I \tag{12}$$

- P is the electric power
- ΔV is the cell potential
- I is the current generated

The current that is generated in the cell is the Faraday's current and it can be expressed as follows:

$$I = \dot{n}_{Fuel} \cdot z \cdot F \tag{13}$$

- F Faraday's constant
- z number of electrons exchanged in the reaction
- $\dot{n}_i$ molar flow rate of the species i

2.3 Thermodynamics of electrochemical cells

The first and second principles of thermodynamics have been applied to the control volume of the stack, which is represented as a black box, under steady state and equilibrium conditions [24].

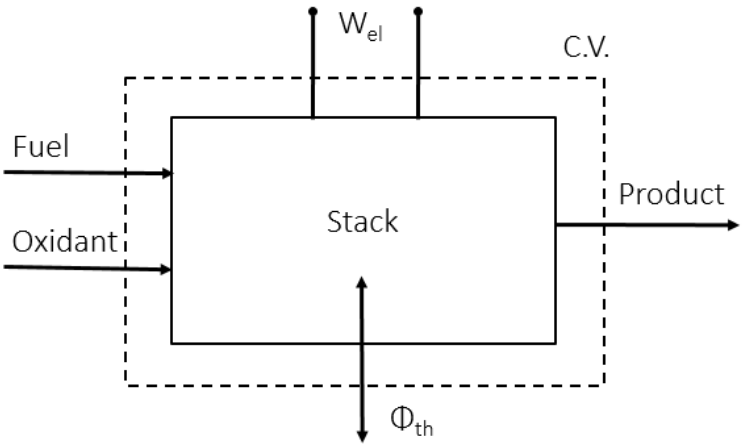

Figure 5 - Control Volume of the stack

Applying the first principle of the thermodynamics for open systems to the control volume leads to:

$$\phi_{th} - W_{el} = \Delta H_{react} \tag{14}$$

- ϕ_{th} is the heat exchanged by the cell with the environment
- W_{el} is the electrical work exchanged by the cell with the environment
- ΔH_{react} is the total enthalpy at temperature and pressure conditions of a state *x,* calculated as:

$$\Delta H_{react} = \dot{n}_{prod} \cdot \bar{h}_{prod}(T, p_i) - \dot{n}_{Fuel} \cdot \bar{h}_{Fuel}(T, p_i) - \dot{n}_{ox} \cdot \bar{h}_{ox}(T, p_i) \quad (15)$$

- h_i is the molar enthalpy of the species i

Afterwards, the second principle of thermodynamics for open systems has been applied to the control volume above, which defines the irreversibility of a process:

$$\frac{\phi_{th}}{T} = \Delta S \quad (16)$$

$$\Delta S = S_{out} - S_{in} - S_{irr} = \Delta S_{react} - S_{irr} \quad (17)$$

$$\phi_{th} + T \cdot S_{irr} = T \cdot \Delta S_{react} \quad (18)$$

- S_{irr} is the entropy generated by the irreversibilities
- ΔS_{react} is the total entropy at temperature and pressure conditions of a state *x,* calculated as:

$$\Delta S_{react} = \dot{n}_{prod} \cdot \bar{s}_{prod}(T, p_i) - \dot{n}_{Fuel} \cdot \bar{s}_{Fuel}(T, p_i) - \dot{n}_{ox} \cdot \bar{s}_{ox}(T, p_i) \quad (19)$$

- s_i is the molar entropy of the species i

Combining these two equations (14) and (18), it is possible to obtain:

$$W_{el} = -\Delta H_{react} - T \cdot \Sigma_{irr} + T \cdot \Delta S_{react} \quad (20)$$

From this equation, it is clear that the maximum work can be obtained when considering a reversible process ($\Sigma_{irr} = 0$).

$$W_{el}^r = -\Delta H_{react} + T \cdot \Delta S_{react} = -\Delta G_{react} \quad (21)$$

Normalizing by the molar flow rate:

$$l_{el}^r = -\Delta \bar{h}_{react} + T \cdot \Delta \bar{s}_{react} = -\Delta \bar{g}_{react} \quad (22)$$

Exploiting the Faraday law:

$$l_{el}^r = \frac{W_{el}^r}{\dot{n}_{Fuel}} = \frac{I \cdot V^r}{\frac{I}{F \cdot z}} = V^r \cdot F \cdot z \quad (23)$$

The only situation in which the cell works in reversible condition is when the circuit is open, therefore there is no generation of entropy.

The voltage measured across the cell in this condition is called open circuit voltage, and looking at the equations above it is possible to obtain the Nernst equation:

$$OCV = -\frac{\Delta \bar{g}_{react}}{F \cdot z} \tag{24}$$

- $\Delta \bar{g}_{react}$ is the total molar Gibbs free energy of the reaction at constant temperature and pressure conditions

The Gibbs free energy is the thermodynamic potential that defines the spontaneity of a reaction at temperature and pressure conditions of a state *x*, and it is minimized when the system reaches the chemical equilibrium. If $\Delta G < 0$ the reaction is spontaneous, this occurs when the reaction is exothermic ($\Delta H < 0$) and the order of the reaction decreases ($\Delta S > 0$); if it is exothermic but the order increases, it is only spontaneous at low temperature; if it is endothermic and the order decreases, only high temperature will make the reaction spontaneous; if none of these conditions is verified the reaction is not spontaneous ($\Delta G < 0$), and so it will not take place.

The larger the Gibbs free energy of the reaction, the larger is the voltage drop that can be generated. As the Gibbs free energy is function of the thermodynamic state, so does the open circuit voltage.

The increase of the temperature makes the Gibbs free energy drop, but even if this would suggest that at lower temperature the system works better, there are always less voltage losses at higher temperature when the hypothesis of reversibility is not considered.

The temperature of the gases under consideration is high enough, so they can be treated as ideal gases.

The Gibbs free energy is defined as follows:

$$\bar{g}_i(T, p_i) = \bar{h}_i(T, p_i) + \bar{s}_i(T, p_i) \tag{25}$$

- p_i partial pressure of the species

The pressure variation, at constant temperature, does not affect the enthalpy:

$$\left(\frac{\partial h}{\partial p}\right)_T = 0 \tag{26}$$

As a consequence of the equation (26), the enthalpy can be written as follows:

$$\bar{h}_i(T, p_0) = \bar{h}_i(T, p_i) \tag{27}$$

- p_i partial pressure of the species
- p_0 reference pressure

Regarding the entropy:

$$\left(\frac{\partial s}{\partial p}\right)_T = -\frac{\bar{R}}{p} \cdot dp \tag{28}$$

From the equation (28), it is possible to obtain:

$$\bar{s}_i(T, p_i) = \bar{s}_i(T, p_0) - \bar{R} \cdot \ln\left(\frac{p_i}{p_0}\right) \tag{29}$$

- $\bar{R}$ universal gas constant

Combining the equations (25)-(27)-(29), it is possible to obtain the expression that describes the Gibbs free energy:

$$\bar{g}_i(T, p_i) = \bar{g}_i(T, p_0) + \bar{R} \cdot T \cdot \ln\left(\frac{p_i}{p_0}\right) \tag{30}$$

As a consequence:

$$OCV(T, p) = -\frac{\Delta \bar{g}_{react}(T, p_0)}{z \cdot F} + \frac{\bar{R} \cdot T}{F \cdot z} \ln\left[\frac{\prod_i^n (\frac{p_i}{p_0})^{\nu_i}}{\prod_i^m (\frac{p_i}{p_0})^{\nu_i}}\right] \tag{31}$$

- ν_i generic stoichiometric coefficient
- m number of products
- n number of reactants

When the circuit is closed, the current is no more equal to zero and it starts to flow in the external circuit breaking the chemical equilibrium at the electrodes. The system is no more in ideal conditions, and the cell voltage will always be lower than the OCV for a galvanic cell and higher for an electrolytic one.

The differences between real and ideal functioning arise due to the occurrence of the mass and charge transport phenomena: charge transfer related to kinetic behavior of electrochemical reactions at the electrodes; charge conduction related to ions conduction through the electrolyte and to electrons conduction in the external circuit; mass transport related to

molecular diffusion in electrodes pores. Due to these effects, losses are generated, and therefore the value of the voltage has to overcome all the resistances.

The relationship between the operation voltage and the intensity of the current flowing through the cell is called polarization curve and such correlation depends on OCV and on all the overpotential that might take place in the cell.

$$V_{cell}(T,p) = OCV(T,p) + \eta_{ohmic} + \eta_{activation} + \eta_{diffusion} \tag{32}$$

It is possible to include all these overpotential effects in a single term known as area-specific resistance (ASR), which is defined as follows [6]:

$$ASR = \frac{\eta_{ohmic} + \eta_{activation} + \eta_{diffusion}}{i} \tag{33}$$

- i is the current density

Therefore the overall voltage of the cell can be calculated as:

$$V_{cell} = OCV - i \cdot ASR \tag{34}$$

The current density is assumed positive for the fuel cell mode, which means that less power is produced due to the resistances, while it is assumed negative for the electrolysis mode, and so more power is absorbed by the source to produce a certain amount of fuel.

The ASR strongly depends on the temperature of operation, in fact, the ohmic voltage drop is a function of the resistivity of the material taken into consideration, which decreases as the temperature increases.

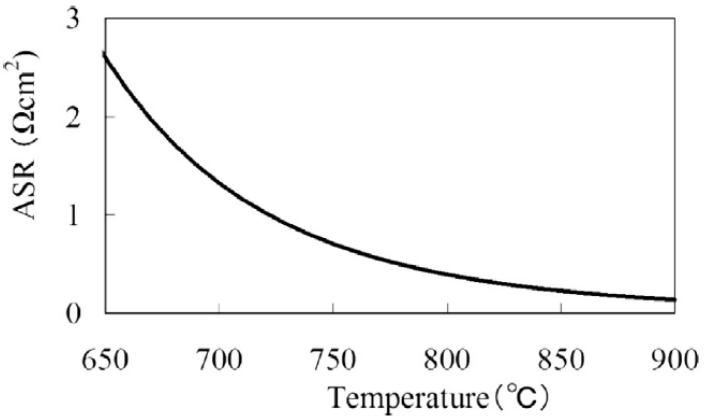

Figure 6 - ASR as a function of the temperature according to [13]

2.4 Heat integration

During cell operation, many thermal fluxes are exchanged within the system. Such heat fluxes are generated by the reaction itself and by the overvoltages. All the overvoltage effects will generate heat; the effects of the thermodynamic reactions will generate an exothermic or an endothermic heat flux, depending on the cell operating mode.

In case of operating under galvanic cell mode, the entropy of the reaction is negative, so there will be a generation of a heat flux equal to $T \cdot \Delta s_{react}$. In case of electrolysis mode of operation the entropy of the reaction is positive, thus there will be absorption of a heat flux equal to $T \cdot \Delta s_{react}$.
As a result, in fuel cell mode there are only heat generating phenomena, therefore it will always be characterized by an exothermic behavior. On the contrary, in electrolysis mode, the cell can work with an endothermic or exothermic behavior depending on the entity of the thermal fluxes; if the system is endothermic there will be a good efficiency of the electrical part, but there will be necessity of heat supply; instead, if the system works in exothermic regime it will operate at lower electrical efficiency.

Therefore, the integration of thermal energy storage (TES) improves economics and the efficiency of a RSOC system.
Thermal energy storage occurs when there is either an absorption or a release of heat from the storage medium. The TES offers the possibility of recovering big amounts of energy that is otherwise wasted. Recovering heat allows every technology to enhance the efficiency of operation.
The heat is transferred to the storage medium during the discharging period and released at a later time during the charge process.

There are three main mechanisms for storing energy: sensible heat storage, latent heat storage and chemical storage [14].

In the sensible heat storage, the energy is accumulated by varying the temperature of a liquid or solid medium without any change of phase in the temperature range of the process. The storage during charge operation is obtained by raising the temperature of the material. Therefore it is important for the medium to have a high specific heat capacity, low cost and long-term stability

under thermal cycling [15]. The drawback is that this storage is strongly dependent on the volume of the media taken into consideration, as a consequence to store a large amount of heat requires a large volume available.

The chemical energy storage is usually performed through a chemical reaction capable of storing thermal energy thanks to its endothermicity and reversibility. The endothermic reaction would store energy and as a consequence the opposite exothermic reaction would release the heat stored, this mechanism can be improved by the integration of a catalyst [14].

The latent heat thermal energy storage is based on the absorption or release of heat when the medium of storage undergoes a phase change, without a significant temperature variation, almost isothermally. The phase change can be either solid to liquid or liquid to gas and vice versa [16]. The materials used for this type of storage are called phase change materials (PCM). However, in real applications it is difficult to work isothermally; therefore the system operates at a temperature range that includes the melting one. Such storage has a higher energy density with respect to the sensible one.

Usually, liquid-gas PCMs have higher specific latent heat than liquid-solid, on the other hand, this transformation involves a large volume variation, and therefore they are not suitable for practical applications. As a consequence, the most common latent heat storage systems are based on the solid-liquid phase change.

The storage capacity of a PCM is the sum of the sensible heat of the solid, from the initial temperature until the melting one, the latent heat and the sensible heat of the liquid, from the melting temperature until the final one:

$$Q = m(C_s(T_f - T_1) + Q_{latent} + C_l(T_2 - T_1)) \tag{35}$$

- m is the mass of the phase change material
- C_s is the specific heat of the solid
- C_l is the specific heat of the liquid phase
- T_1, T_2 initial and final temperature
- T_f temperature of the phase transition
- Q_{latent} is the latent heat of the phase change

To study the behavior of the PCM the heat transfer equation is used, and only the conduction is considered [17]:

$$\rho C_{eq} \frac{\partial T}{\partial t} + \nabla \cdot \left(-k_{eq} \nabla T\right) = Q \tag{36}$$

- ρ is the density of the PCM and it is calculated as:

$$\rho = \theta \rho_{ph1} + (1 - \theta)\rho_{ph2} \tag{37}$$

- θ is the fraction of the phase before the transition, it is equal to 1 before the phase change and equal to 0 after the phase change
- C_{eq} is the equivalent heat capacity at constant pressure of the PCM and it is calculated as:

$$C_{eq} = \frac{(\theta \rho_{ph1} C_{p,ph1} + (1 - \theta)\rho_{ph2} C_{p,ph2})}{\rho} \tag{38}$$

- k_{eq} is the effective thermal conductivity and it is calculated as follows:

$$k_{eq} = \theta k_{ph1} + (1 - \theta) k_{ph2} \tag{39}$$

- Q is the heat source

2.5 Heat storage materials

The parameters to be taken into account when choosing a PCM are an appropriate melting point (which should be close at the operation temperature), high heat of fusion, high specific heat capacity (to exploit the sensible heat), high thermal conductivity to be able to transfer heat with small temperature differences, ability to melt congruently, absence of the supercooling or superheating phenomenon, chemical stability, low cost, low flammability, it must be reversible over several phase change cycles, and without significant degradation [18].

The two main categories of phase change materials are the organic and inorganic materials.

The organic PCMs include paraffin and fatty acids, they have large volume change and low melting point well below the target operation temperature of ~700 °C. In fact at this temperature they could undergo to cracking reactions, so they are not suitable for this project.
The inorganic PCMs include salts, salt hydrates, salt eutectics and metals. Inorganic materials have greater phase change enthalpy, high density, high storage capacity and higher thermal conductivity with respect to the organic ones.

The two materials that have been taken into account for this project are Aluminum, a metal, and Magnesium Chloride, a salt. The salts in general are cheaper, with higher heat of fusion and with usually longer life cycle; on the other hand, they are corrosive and they have lower thermal conductivity. However, they are usually preferred, in fact, the thermal conductivity can be easily enhanced combining the PCM with a higher-thermal-conductivity material.
The first parameter to take into account is the melting point. Magnesium Chloride melts at 714℃, very close to the operation temperature. The other parameters that must be taken into consideration are the density and the specific latent heat, in order to calculate the amount of energy that is possible to store in the volume available.

Heat storage is an important element of this project, and besides the heat storage, it is relevant to study how this heat is transported between the cell and the PCM. Two ways are possible: use a heat carrier or apply the PCM in direct contact with the cells, in order to exploit heat transmission by thermal conduction [18]. In this project, the combination of these two methods has been applied. In fact the PCM is located above the cell stack and the heat carrier used is the air, which is used as working fluid for heat exchange, but it also comes in contact with the electrodes where the reaction takes place.

3. STUDY CASES AND RESULTS

3.1 CASE 1: Heat exchanger

3.1.1 Model description

Two concentric pipes in counter-current with air inside have been sized, since in this project it is needed a preheated air that enters in the stack, and the remaining unused air must come out. Moreover, a greater heat recovery is achieved with a countercurrent design with respect to the co-current one. The inner pipe has cold air entering at ambient temperature (20°C) and coming out nearly at the operation temperature of the stack (700°C), the outer one has hot air that enters at 750°C.

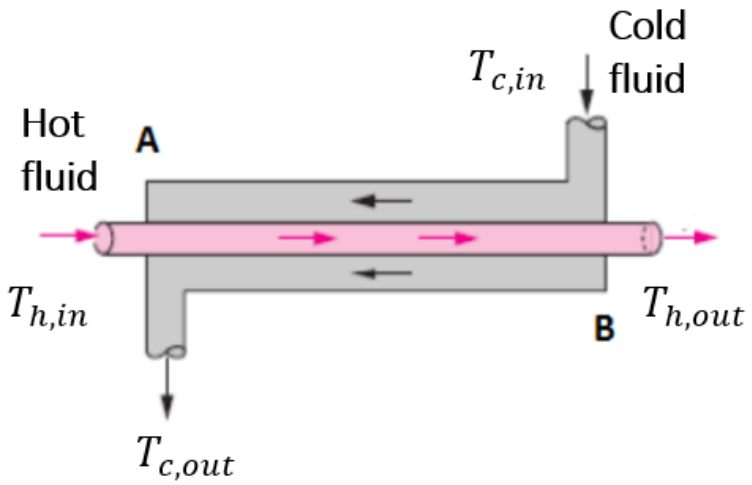

Figure 7 - Counter-Current heat exchanger [19]

In order to calculate how much the hot stream gets cold, the heat exchanged through conduction has been neglected and it has been assumed a perfect insulated system.

The goal of these calculations was to find the minimum length varying the inner and outer mass flow rate and the diameters of the two pipes.

The outlet temperature of the outer pipe has been found equating this two equations:

$$Q = \dot{m}_{in} \cdot cp_{in}\left(T_{c,in} - T_{c,out}\right) \tag{40}$$

$$Q = \dot{m}_{out} \cdot cp_{out}\left(T_{h,in} - T_{h,out}\right) \tag{41}$$

$$T_{h,out} = -\frac{\dot{m}_{in} \cdot cp_{in}\left(T_{c,in} - T_{c,out}\right)}{\dot{m}_{out} \cdot cp_{out}} + T_{h,in} \tag{42}$$

- $\dot{m}$ is the mass flow rate
- c_p is the heat capacity at a constant pressure

To calculate the length this equation has been used:

$$Q = U \cdot \Delta T_{ml} \cdot \pi \cdot d_{in} \cdot L \tag{43}$$

- L is the length of the pipe
- d_{in} is the diameter of the inner pipe
- ΔT_{ml} is the logarithmic mean temperature difference calculated as follow:

$$\Delta T_{ml} = \frac{(\Delta T_1 - \Delta T_2)}{\ln\left(\frac{\Delta T_1}{\Delta T_2}\right)} \tag{44}$$

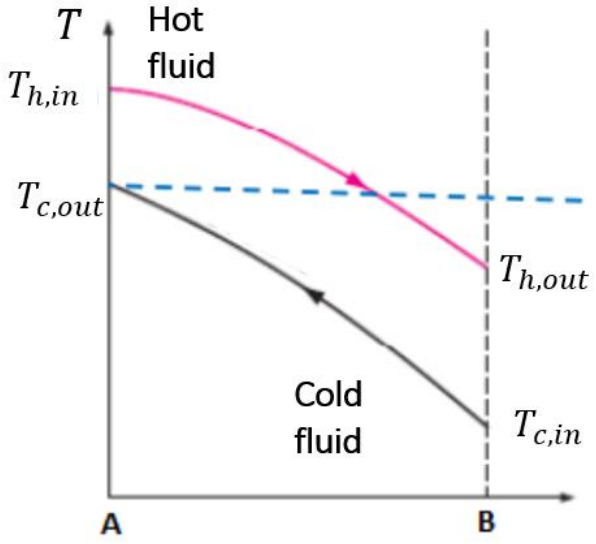

Figure 8 - Temperature variation in a counter-current heat exchanger [19]

$$\Delta T_1 = (T_{h,out} - T_{c,in}) \tag{45}$$

$$\Delta T_2 = (T_{h,in} - T_{c,out}) \tag{46}$$

- U is the thermal transmittance or global heat transfer coefficient:

$$U = \frac{1}{\frac{1}{h_{in}} + \frac{th}{k_{pipe}} + \frac{1}{h_{out}}} \tag{47}$$

- h is the convective heat transfer coefficient for the inlet and the outer pipes
- k is the thermal conductivity of the pipe
- th is the thickness of the pipe

This convective heat transfer coefficient has been obtained from the Nusselt number that has been calculated as an empirical combination of the Reynolds and the Prandtl numbers.

$$Re = \frac{\rho \cdot u \cdot D_h}{\mu} \tag{48}$$

- ρ is the density
- D_h is a characteristic length of the phenomenon considered, in this case it is the hydraulic diameter
- μ is the dynamic viscosity of the fluid
- u is the velocity of the flow

For the inner pipe:

$$D_h = d_{in} \tag{49}$$

For the outer pipe:

$$D_h = d_{out} - d_{in} \tag{50}$$

The Reynolds number can be calculated as a function of the mass flow rate thanks to this correlation:

$$\dot{m} = \rho \cdot v \cdot A \tag{51}$$

- A is the surface area of the base of the cylinder

$$A = \frac{d^2}{4}\pi \tag{52}$$

$$Re = \frac{\dot{m} \cdot 4}{D_h \cdot \mu \cdot \pi} \tag{53}$$

The number of Reynolds allows to evaluate if the fluid flow is in a laminar regime or in turbulent regime. The value that separates the laminar and the turbulent regime depends on the shape of the body in which the fluid passes. For this case, which is the flow inside a cylindrical tube, it is laminar regime for Re<2300 and turbulent regime for Re>4000, the intermediate values correspond to the transition regime.

The number of Reynolds values for the present case represent a laminar regime, so the appropriate correlation for this condition to find the Nusselt number is expressed as follows:

$$Nu = 3.66 + \frac{(0.065 \cdot Re \cdot Pr \cdot \frac{D_h}{L})}{1 + 0.04 \cdot (Re \cdot Pr \cdot \frac{D_h}{L})^{\frac{2}{3}}} \tag{54}$$

- Pr is the Prandtl number:

$$Pr = \frac{\mu \cdot c_p}{k} \tag{55}$$

The Nusselt number expresses the relationship between the flow of heat exchanged by convection and the one exchanged by conduction:

$$Nu = \frac{h \cdot D_h}{k} \tag{56}$$

The length has been varied through an iterative method, until the latter has reached the convergence.

3.1.2 Results

The software that has been used for this project is COMSOL Multiphysics®, a tool for modeling and simulating engineering tasks.

Multiphysics simulations are needed, and therefore a software able to solve coupled phenomena and the corresponding partial differential equation [20].

Each physics used in the software contains predefined equations, however it is possible to modify directly the coefficients of the PDE, and it is possible to define boundary conditions on internal and external boundaries, both Neumann and Dirichlet.

The Navier Stokes equations, which are partial derivative equations that describe the motion of viscous fluid substances with the hypothesis of the fluid continuity, have been solved with the techniques of the finite element method.
The finite element method is a numerical technique used to find approximate solutions to problems described by partial different equations.
For the study of the heat transfer, the heat conservation equation has been used:

$$\rho c_p \frac{\partial T}{\partial t} + \rho c_p u \nabla T + \nabla \cdot (-k \nabla T) = Q \tag{57}$$

- u is the velocity
- t is the time

The first term is the one that represents the variation over time, and it is neglected for the initial models.

The finite element method (FEM), firstly, divides the entire domain into smaller parts, called elements; on each element it describes the relationships among the variables and then it unifies all the elements in order to obtain the relationships among the variables on the whole domain. Therefore the main characteristic of this method is the discretization of the domain, the mesh, through the use of simple geometrical shapes.

An axisymmetric geometry has been chosen for the two concentric pipes, because every point is symmetric to the central axis. By choosing this geometry it is possible to solve the problem in 2-dimensions.
In the 2D the geometry the elements of the mesh are subdivided in triangles or quadrilaterals [21].

Stainless steel is the material which has been used for the thickness of the pipes. The air inside the pipe has been defined as an ideal gas; the density, the constant pressure specific heat, and the thermal conductivity have been calculated as a function of temperature.

The physics that have been used are the 'laminar flow' and the 'heat transfer in solids'.
As flow boundary conditions, the inflow has been imposed in terms of mass flow rate for both outer and inner pipes; the outflow has been set in order to achieve a pressure gradient, between inside the pipe and the external environment, equal to zero; no-slip condition has been imposed at the walls, which implies a null fluid velocity.

The initial conditions for the fluid flow have been set as:

$U_z = 1, U_r = 0$ for the inner pipe

$U_z = -1, U_r = 0$ for the outer pipe

Dirichlet thermal boundary conditions have been imposed for the inlet temperatures of the two pipes, the inner one at 20 ℃ and the outer one at 700℃, as specified in table 1; instead, Neumann boundary conditions have been set for the outflow, imposing thermal flux equal to zero.

The initial condition for the heat transfer has been set at 20℃ for the whole domain shown is Figure 9.

Table 1 - Operating conditions of the counter-current pipe

Geometry parameters		
Parameter	Value	Units
L	20	cm
R_{in}	2	cm
R_{out}	3.8	cm
$th_{SS.in}$	0.3	cm
$th_{SS.out}$	0.4	cm
Operating conditions		
$T_{c,in}$	20	℃
$T_{h,in}$	700	℃
$\dot{m}_{in}$	1.00e-5	kg/s
$\dot{m}_{out}$	1.00e-5	kg/s
$T_{outside}$	20	℃
h_{conv}	20	$W/m/K$

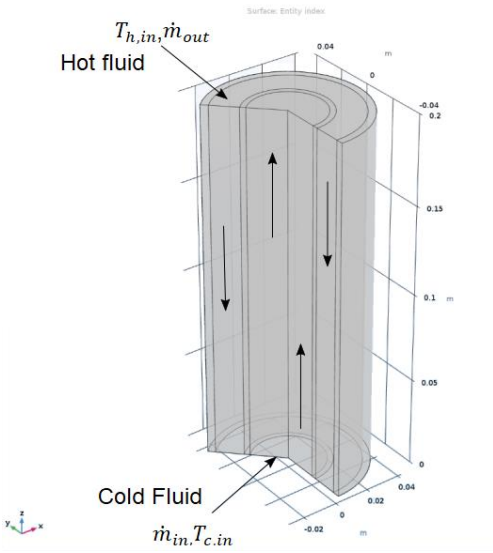

Figure 9 -Boundary Condition of the heat exchanger

The mesh has been built physics- controlled with normal element size and the study is steady state, with a direct Fully Coupled solver.

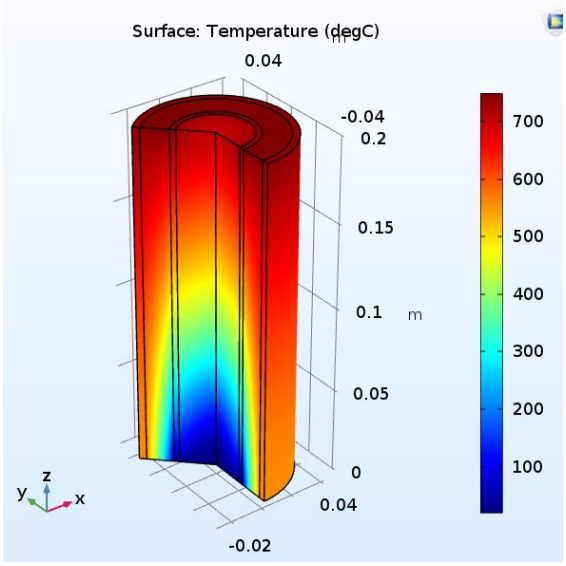

Figure 10 -Temperature distribution of the heat exchanger perfectly insulated

This picture (Figure 10) represents the ideal case, perfectly insulated with no losses to the external environment.

Adding the convection on the external walls of the pipe, the result changes considerably as it is possible to see from Figure 11. The convective heat transfer coefficient has been chosen equal to 20, this value corresponds to a convection with velocity of air of ≈ 2 m/s.

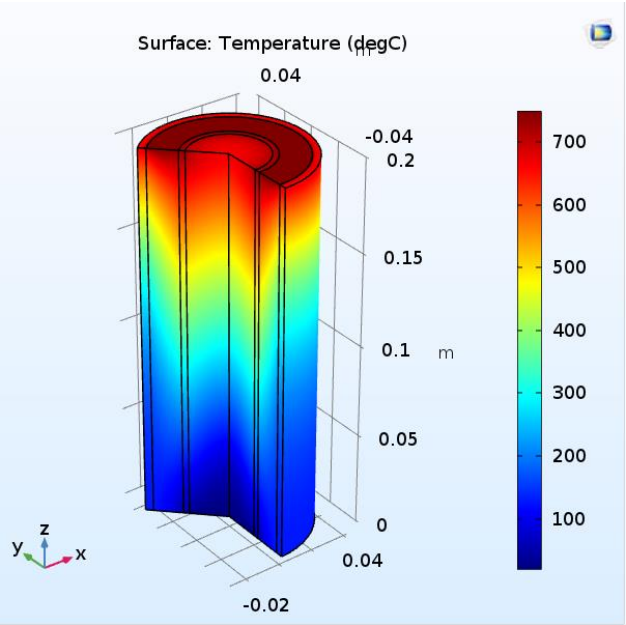

Figure 11 - Temperature distribution of the heat exchanger with convection in the outer wall

The numerical model for the counter-current heat exchanger has been done first in 0-dimension with the calculations seen in section 3.1.1 Model description, later on the same model has been implemented in Comsol Multiphysics as already mentioned, and the two models' results coincided. In fact, in the 0-D model the temperatures were the inputs and the output was the geometry, instead, in the Comsol model the geometry was the input, and the output was the outlet temperature of the cold fluid, which was very close to the value of the first model.

Thanks to the first hand calculations of the Reynolds number, it has been possible to use the hypothesis of laminar flow.

In the Figure 10 the air is completely preheated, but that is the ideal case, with the external walls completely insulated. In Figure 11, a more realistic case is shown, with a weak heat flux on the external walls, and from this image it is possible to see that the temperature gradient is completely different from the ideal case, and the air that flows out is at 680 °C, thus ≈ 20 °C less than previously.

3.2 CASE 2: Integrating a Heat exchanger with a RSOC stack

3.2.1 Model description

Afterwards, the stack has been added to the model with the same parameters calculated for the optimal counter-current heat exchanger.

In this work, the RSOC stack with Fe/FeO is taken into account but it is not physically implemented, and so it is not designed in detail. It is represented as an effective porous medium that produces heat; thus the Comsol physics has been changed into "Heat Transfer in Porous Media", and "Free and Porous Media Flow", which, unlike the laminar flow physics, takes into account also the Darcy´s law.

Inside the stack has been placed an indicative heat source that brings the stack to the temperature of operation.

The porous matrix properties are the porosity and the permeability:

$$\epsilon_p = 0.4 \ , \ \kappa = 10^{-10} \ m^2$$

An insulation material has been put around the stack, in this case the expanded polystyrene board has been used, which has a thermal conductivity of 0.05 $W/m/K$. The geometry of the stack and the insulation are provisional and will be modified in subsequent sections of the thesis.

This first picture (Figure 12) represents the temperature of the stack with a convective heat flux outside of it.

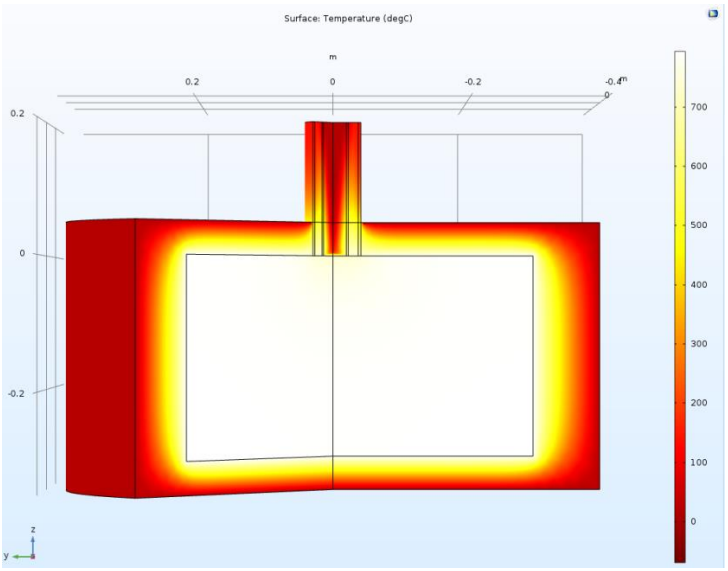

Figure 12 **-** Temperature distribution of the model

In this case there is no longer the inlet of the mass flow rate of the hot stream as in the model with the simple counter-current pipe, in fact, the hot stream is the flow of hot air coming out of the stack, and it should preheat the cold flow before it enters in the porous media.

The remaining boundaries are defined by a convective heat flux as before.

A box of still air around the system has been added to the same model:

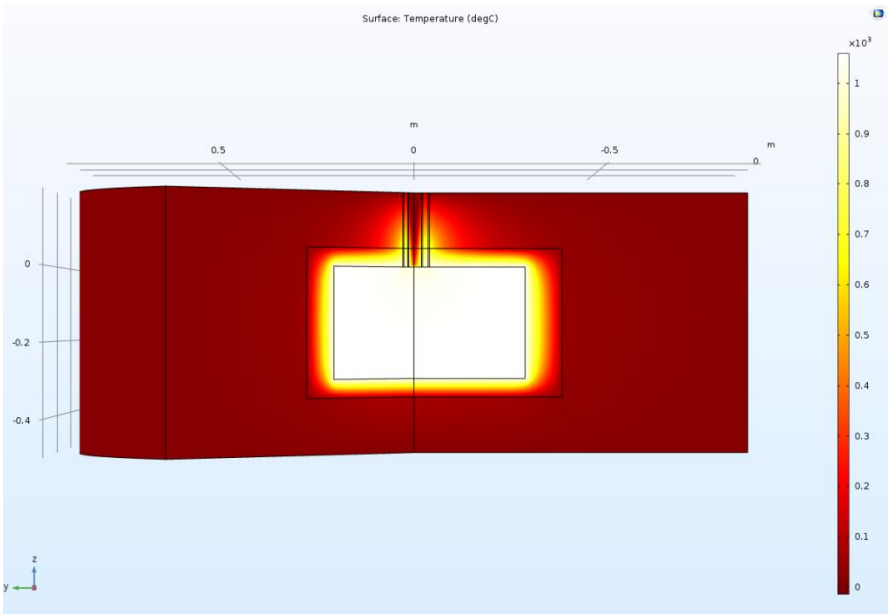

Figure 13 **-**Temperature distribution with still air around the model

As it is possible to notice, with the same heat source inside the stack, the range of temperature changes considerably, because the velocity of the still air has been set equal to 0, instead, the

convective heat transfer coefficient in Figure 12 has been calculated considering the air velocity equal to 2 m/s.

Afterwards, the model has been implemented with more realistic geometries for the stack (height=4 cm and side= 10 cm). As in the previous model, a heat source has been placed in the stack, thus the model is working in fuel cell mode.

A channel of air has been built all around the stack connected with the outer pipe of the heat exchanger, in this way the air can enter the stack from above and exit from below.

In the figure below (Figure 14) half of the entire 3D geometry is reported. Symmetry condition has been imposed, and consequently only half of the entire geometry has been analyzed, this allows to shorten significantly the computational time.

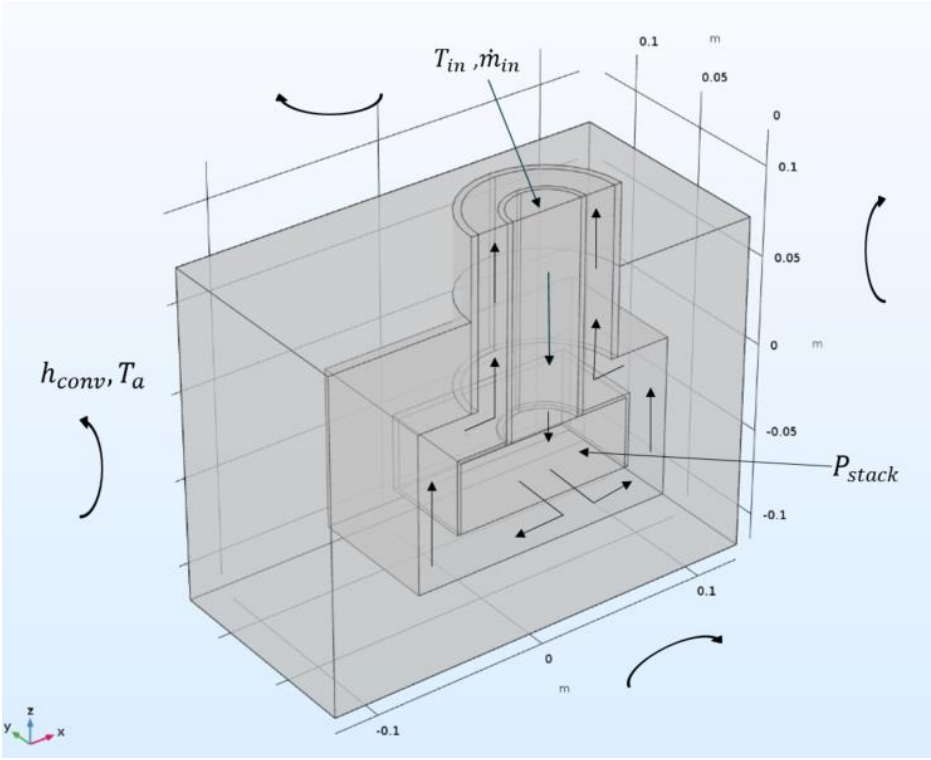

Figure 14 – Geometry and boundary conditions of the 3D model

The cold air enters the system in the outer tube, it goes down and it gets in the stack from above, the stack is a porous medium so that the air can go through it. The stack is releasing heat (P_{stack}), so the air warms up and then, following the channel, the hot air coming out of the stack goes up and exchange heat with the cold inlet air.

In this configuration, the fluid flow has fewer issues and it converges more easily than the previous model in Figure 12-13, in which there is not the channel for the air flow.

On the external walls there is a convective heat flux, as in Figure 12.

The initial conditions for the flow have been set as:

- $U_z = -1, U_r = 0$ for the inner pipe and the stack in the axisymmetric component
- $U_z = 1, U_r = 0$ for the outer pipe and the outer channel of air in the axisymmetric component
- $U_z = -1, U_x = 0,\ U_y = 0$ for the inner pipe and the stack in the 3D component
- $U_z = 1, U_x = 0,\ U_y = 0$ for the outer pipe and the outer channel of air in the 3D component

The initial value of the temperature in the whole domain is set at 20℃.

The mesh is physics- controlled with a coarse size.

The study is stationary and the solver has a Fully Coupled scheme and a direct (MUMPS) method.

Table 2 - Operating conditions of both the 3D and the axisymmetric models

Operating conditions		
T_{in}	20	℃
T_a	20	℃
$\dot{m}_{in}$	0.0001	kg/s
h_{conv}	15	$\frac{W}{K \cdot m^2}$
P_{stack}	70	W
$Molar\ mass\ of\ the\ flow\ rate: air$	28.84	$\frac{kg}{kmol}$

P_{stack} Is the heat power supplied to maintain the temperature of operation (~700 ℃); it represents the heat released by the exothermic reactions in the stack.

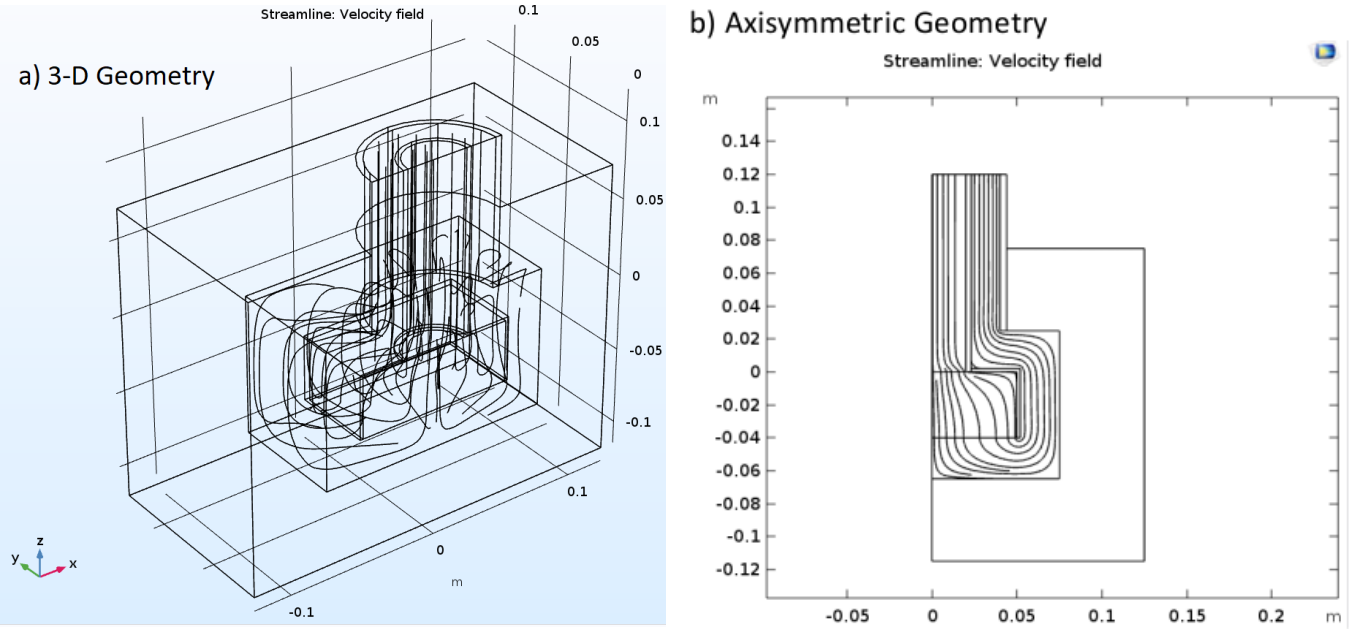

Figure 15 - The path of the fluid in a 3D geometry (a) and in an axisymmetric geometry (b)

The air that comes out from the stack at first is at ~700°C and it should preheat the air that enters in the stack.

The air can flow only from the upper to the bottom part of the stack. A proper stainless steel layer covers the remaining faces of the parallelepiped, in order to not let the air pass.

The model has been built with both an axisymmetric geometry (Figure 16), for the faster computation, and a 3D one (Figure 17).

In the 3D geometry, the elements, in which subdomains are subdivided, can be tetrahedral, hexahedrons or prisms, and the outlines are divided into triangles or quadrilaterals [21].

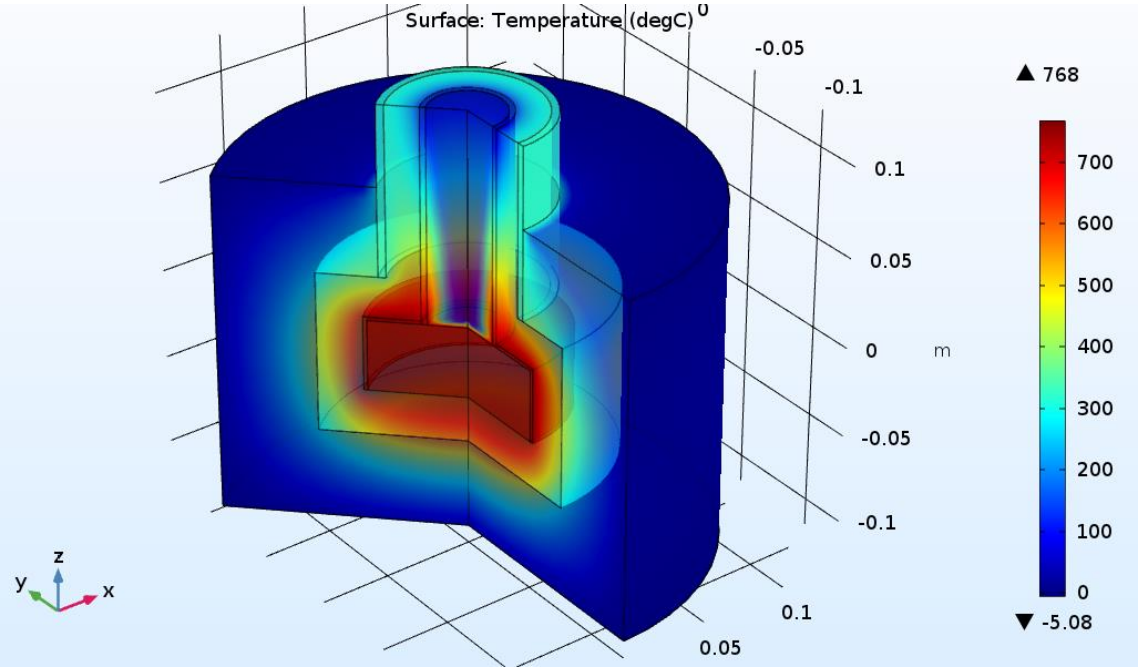

Figure 16 – Temperature distribution in the axisymmetric model

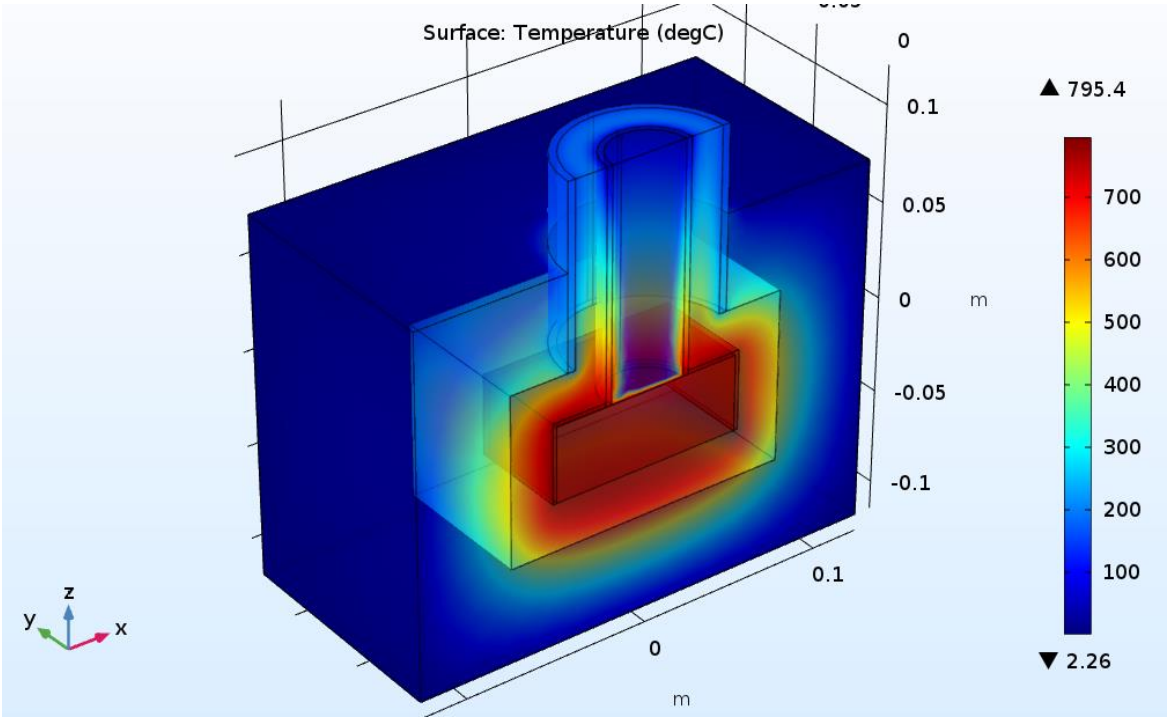

Figure 17 - Temperature distribution in the 3D model

In order to heat the stack to the operating temperature, these two models require a different amount of power, and even if the 3D model has a bigger volume of the stack, it is required less power than the other (70 W for 3D model, 110 W for the axisymmetric). Moreover, as it is possible to notice from the pictures, in the 3D model there is a better heat exchange, in fact the air that comes out is colder.

Although in neither of the two models the air that enters in the stack is heated up, this means that a longer pipe or a better heat exchanger is needed.

3.2.2 Possible Heat exchanger solutions

As is possible to see from the previous pictures, the air that enters in the stack is not well preheated, it is necessary to design a better heat exchanger. Thus, the simple counter-current pipes have been replaced with something more similar to a heat exchanger and different geometries have been considered.

- GEOMETRY n° 1:

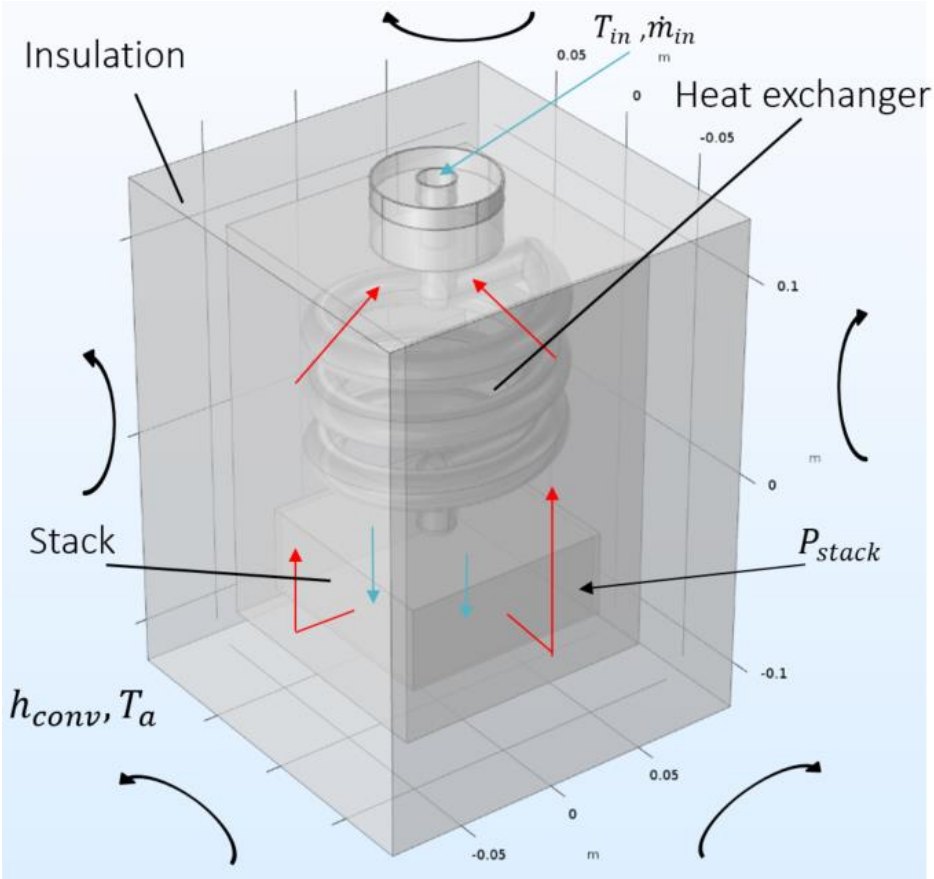

Figure 18 - Helix geometry and boundary conditions

Table 3 - Operating conditions of the 3D helix model

Geometry parameters		
Outer radius of the pipe	2.8	cm
Inner radius	0.8	cm
Major radius of the helix	5	cm
Minor radius of the helix =Inner radius	0.8	cm
Axial pitch of the helix	3	cm
Width and depth of the air box	13	cm
Height of the air box	20	cm
Width and depth of the insulation	19	cm
Height of the insulation	25	cm
Thickness of the pipes	0.1	cm
Height of the stack	4	cm
Side of the stack	10	cm
Thickness of the SS layer	0.2	cm
Operating conditions		
T_{in}	20	℃
T_a	20	℃
$\dot{m}_{in}$	0.0001	kg/s
h_{conv}	15	$\frac{W}{K \cdot m^2}$
P_{stack}	60	W
$Molar\ mass\ of\ the\ flow\ rate: air$	28.84	$\frac{kg}{kmol}$

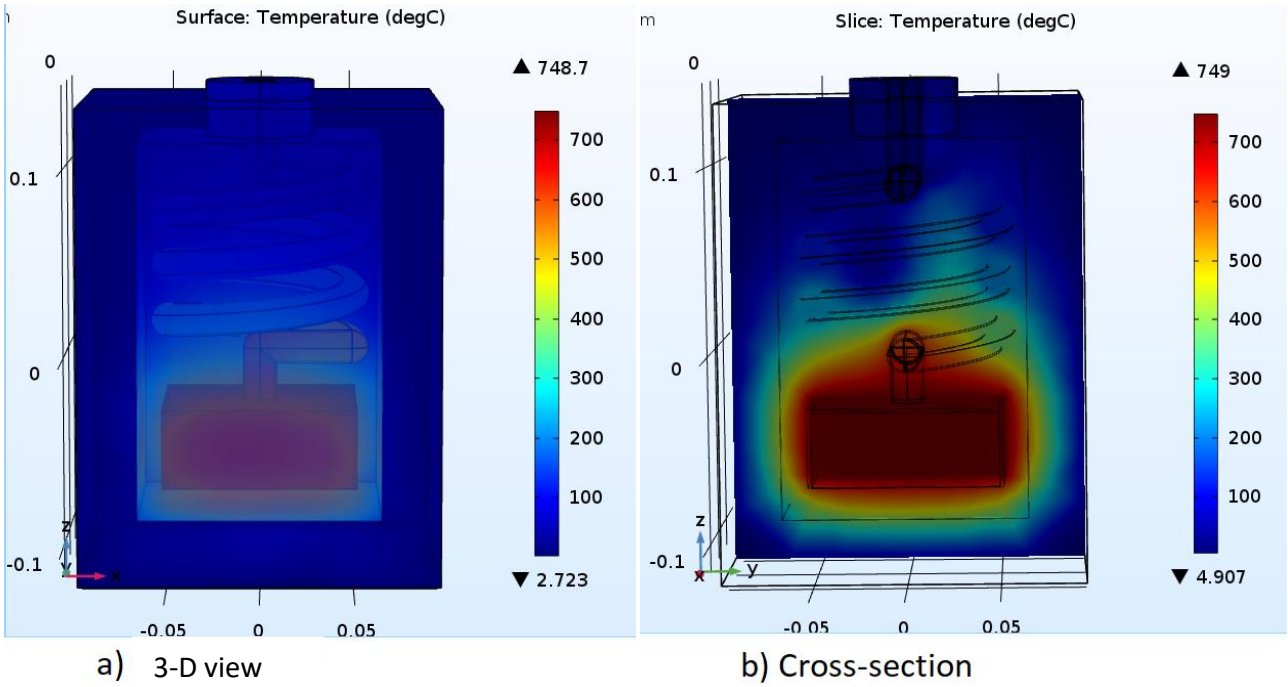

Figure 19 – 3-D (a) and cross-section (b) represent the temperature distribution of the helix geometry

This model has been designed in 3D using the helix geometry. In the first picture (Figure 19a) is shown the 3D view and in the second one (Figure 19b) the cross-section, both of them represent the gradient of temperature. As before, there is a heat power defined as a heat source in the stack domain. The air enters in the inner region and flows out in the outer region.

The thermal Dirichlet boundary condition is in the inner region.

In this model the heat exchanger has more surface area to exchange the heat. In fact, compared to the previous model. it is clear that the air when arrives at the stack is well preheated, and the air that flows out of the system is well cooled. Moreover, the power supplied to maintain the temperature at the operating conditions is less than before, having kept the size of the stack and the insulation properties constant with respect to the previous model in Figure 17.

The stack is releasing heat as the system operates in fuel cell mode; to provide sufficient cooling, the amount of air that flows through the system is much higher than the stoichiometric amount needed for 60 W of heat power inside the stack.

❖ GEOMETRY n°2:

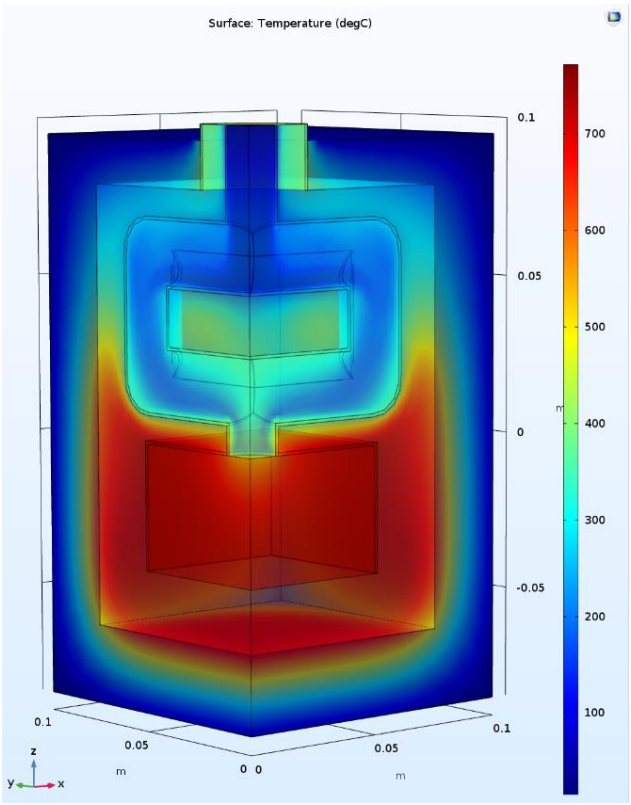

Figure 20 - Temperature distribution of the second geometry

Table 4 - Operating conditions of the counter-current pipe

Geometry parameters		
Outer radius of the pipe	2.2	cm
Inner radius	1	cm
Height of the air box	14	cm
Width and depth of the air box	15	cm
Width and depth of the insulation	20	cm
Height of the insulation	18	cm
Thickness of the pipes	0.1	cm
Height of the stack	4	cm
Side of the stack	10	cm
Thickness of the SS layer	0.2	cm

Operating conditions		
T_{in}	20	°C
T_a	20	°C
$\dot{m}_{in}$	0.0001	kg/s
h_{conv}	15	$\frac{W}{K \cdot m^2}$
P_{stack}	65	W
$Molar\ mass\ of\ the\ flow\ rate: air$	28.84	$\frac{kg}{kmol}$

Figure *20* represents another model of a heat exchanger, it is in 3D and this is a quarter of the entire geometry because it has been simplified due to symmetry reasons.

From these two models it is possible to notice that in the helix one the power needed in order to maintain the temperature of operation is a bit lower than in the second one, even if the insulation of this geometry is thicker. Moreover, the temperature of the air that comes out in the second one is higher and the inlet air is less heated up, this means that in the helix model there is a better heat exchange.

Looking at these pictures, it is clear that the helix configuration performs better as a heat exchanger. Therefore, it has been decided to adopt the helix configuration and to try to make the design more compact. This choice can be justified looking at the Figure 19; in fact, as it is possible to notice, in the highest part of the air box the temperature gradient is smaller, and therefore the heat exchange is minimal.

The geometry has been studied have a free tetrahedral mesh, physics controlled with a coarse size.

3.3 CASE 3: RSOC under operation

Three different models have been studied, in order to investigate three possible steady state operating scenarios.

The first one has been implemented in fuel cell mode, therefore, with an exothermic behavior of the stack; the second one in electrolysis mode, in which the stack is absorbing heat; and the third one in idle mode, where no reaction occurs and the stack must be kept at the operation temperature. Therefore, the three models must have the same geometry, but different operating conditions, which have been obtained through some theoretical calculations.

3.3.1 Theoretical calculations

Fuel cell mode

Afterwards, using the thermodynamic data for the reaction $Fe + ½O_2 \longrightarrow FeO$ in the range of temperature of 600 ÷ 800 ℃ , the mass flow rate of oxygen required by the reaction and the size of the stack has been calculated assuming these data:

Table 5 - Data assumed for the electrochemical calculations for the fuel cell mode

Parameters	Value	Units
ASR	0.5	Ωcm^2
P	1	kW
i	0.5	A/cm^2
S	100	cm^2
AU	0.5	–
h_{cell}	0.2	cm
$n_{f_{O2}}$	4	–
$n_{f_{Fe}}$	2	–

- S is the base area of the stack
- AU is the air utilization

- P is the power produced
- h_{cell} is the height of each cell

Firstly, having the current density greater than zero, the system has been calculated in galvanic mode. Through the Nernst equation the open circuit voltage has been calculated using the Gibbs free energy at 700°C , and then the voltage of the cell:

$$OCV = -\frac{\Delta g_{react}}{F \cdot n_{f_{Fe}}} = 1.046\ V \tag{58}$$

$$V = OCV - i \cdot ASR = 0.796\ V \tag{59}$$

In this way it is possible to size the stack calculating the height and the number of cells of the stack:

$$n_{cell} = \frac{P}{V \cdot i \cdot S} = 25 \tag{60}$$

$$h_{stack} = n_{cell} \cdot h_{cell} = 5\ cm \tag{61}$$

- h_{stack} is the height of the stack

Afterwards, the stoichiometric and the real air mass flow rate have been calculated using Faraday´s law, which gives a relationship between the molar flow rate of species reacting at electrodes and the current flowing:

$$\dot{m}_{o_2\,stoich} = \frac{I \cdot n_{cell}}{F \cdot n_{F_{O2}}} = \frac{50 \cdot 25}{96485 \cdot 4} = 0.0032\ \frac{mol}{s} \tag{62}$$

$$\dot{m}_{O2\,real} = \frac{\dot{m}_{O2\,stoich}}{AU} = 0.0065\ \frac{mol}{s} \cdot 32\ \frac{g}{mol} = 0.2073\ \frac{g}{s} \tag{63}$$

$$\dot{m}_{air\,stoich} = \frac{\dot{m}_{o_2\,stoich}}{0.21} = 0.0154\ \frac{mol}{s} \cdot 28.84 \frac{g}{mol} = 0.4448\ \frac{g}{s} \tag{64}$$

$$\dot{m}_{air\,real} = \frac{\dot{m}_{air\,stoich}}{AU} = 0.8896\ \frac{g}{s} \tag{65}$$

Moreover, the heat is generated inside the cell by the reaction and the overvoltage effects.

$$|Q_{th}| = |Q_{reaction}| + |Q_{irreversibilities}| \tag{66}$$

In case of galvanic cell the entropy of the reaction is negative, therefore there will be generation of a heat flux $T \cdot \Delta s_{react}$.

As a consequence, in fuel cell mode there is only heat generating phenomena, so it has an exothermic behavior.

$$|Q_{reaction}| = -\frac{T \cdot \Delta s_{react}}{F \cdot n_{f_{Fe}}} \cdot I \cdot n_{cell} = 396.27\ W \tag{67}$$

$$|Q_{irreversibilities}| = I \cdot n_{cell} \cdot \sum_{j} \eta_j = 312.5\ W \tag{68}$$

$$-T \cdot \Delta s_{react} = \Delta g_{react} - \Delta h_{react} \tag{69}$$

$$Q_{th} = \left(-V - \frac{\Delta h_{react}}{F \cdot n_F}\right) \cdot I \cdot n_{cell} = 708.8\ W \tag{70}$$

A polynomial expression has been used for a temperature dependent enthalpy and Gibbs free energy, the data are referred to the reaction $Fe + ½O_2 \longrightarrow FeO$.

$$\Delta h_{react} = -0.0365 \cdot T^2 + 60.12 \cdot T - 2.87e5 \tag{71}$$

$$\Delta g_{react} = 60 \cdot T - 2.63e5 \tag{72}$$

For the Gibbs free energy, a first order polynomial is accurate, for the enthalpy is necessary a second order polynomial. The temperature used in the polynomial are in [K].

Electrolysis mode

The same calculations have been done for the stack working in electrolysis mode, but in this case the geometry is no longer an unknown quantity. The range of temperature and the thermodynamic data are the same.

The reaction that has been taken into consideration is again $FeO \rightarrow Fe + ½O_2$, the data that have been used are as follows:

Table 6 - Data assumed for the electrochemical calculations for electrolysis mode

Parameters	Value	Units
ASR	0.5	Ωcm^2
i	-0.5	A/cm^2
S	100	cm^2
n_{cell}	25	$-$
h_{cell}	0.2	cm
$n_{f_{O2}}$	4	$-$
$n_{f_{Fe}}$	2	$-$

The open circuit voltage has been calculated as before with the Nernst equation, the operation voltage of each cell has been calculated taking into account the overvoltage effects.

$$OCV = \frac{\Delta g_{react}}{F \cdot n_{f_{Fe}}} = 1.046\ V \tag{73}$$

$$V = OCV - i \cdot ASR = 1.296\ V \tag{74}$$

The thermoneutral voltage is a dimension that in electrolysis mode is taken into account, it represents the voltage at which the heat released for the irreversibility equals the heat needed to support the reaction, the closer the voltage of operation is to the thermoneutral one, the more the system is working at high efficiency.

$$V_{tn} = \frac{\Delta h_{react}}{F \cdot n_{f_{Fe}}} = 1.363\ V \tag{75}$$

As already said, working in electrolysis mode the entropy of the reaction is positive, consequently there will be the absorption of a heat flux $T \cdot \Delta s_{react}$.

As a result, there is generation of heat by the overvoltage effects and heat absorption needed from the reaction in order to occur. For this reason, it is possible for the cell to have either an exothermic or an endothermic behavior.

$$|Q_{th}| = |Q_{reaction}| - |Q_{irreversibilities}| \tag{76}$$

$$|Q_{reaction}| = \frac{T \cdot \Delta s_{react}}{F \cdot n_{f_{Fe}}} \cdot I \cdot n_{cell} = 396.27\ W \tag{77}$$

$$|Q_{irreversibilities}| = I \cdot n_{cell} \cdot \sum_{j} \eta_j = 312.5\ W \tag{78}$$

$$T \cdot \Delta s_{react} = -\Delta g_{react} + \Delta h_{react} \tag{79}$$

$$|Q_{th}| = (V_{tn} - V) \cdot I \cdot n_{cell} = 83.78\ W \tag{80}$$

For the electrolysis mode, if the heat produced for the irreversibility is higher than the one needed to supply the reaction, the system works in exothermic behavior, if it is lower the system works in endothermic behavior. In this case:

$$|Q_{reaction}| > |Q_{irreversibilities}| \tag{81}$$

As a consequence, it is possible to say that the stack has an endothermic behavior, this means that is necessary to supply heat to the stack in order to maintain operating temperature.

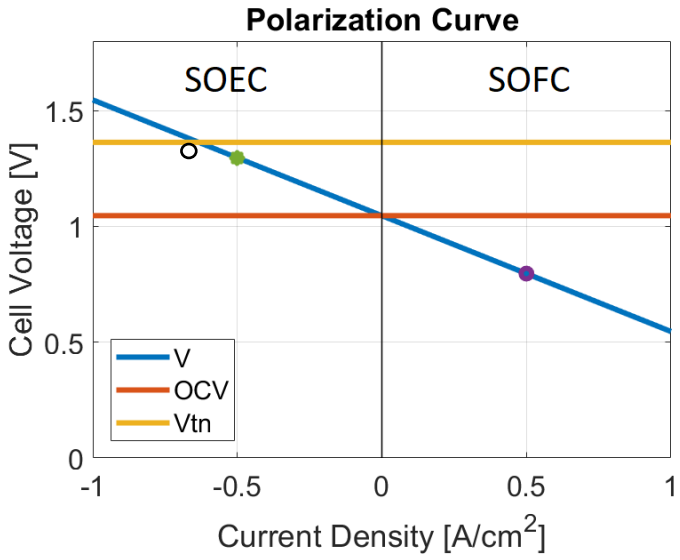

Figure 21 – i-V curve

This picture (Figure 21) represents the polarization curve of the cell that is taken into account, as said before, with positive current density the system works in fuel cell mode and with negative current density it works in electrolysis mode. Where the V- line meets that of the thermoneutral voltage, for the electrolysis mode is the condition of maximum efficiency. This point, which is highlighted by the black circle, splits the SOEC part of graph in two areas, one concerning the exothermic behavior, for $i < i_{tn}$, and the other one concerning the endothermic behavior, for $i > i_{tn}$. The green and the purple dots represent the conditions examined for electrolysis and fuel cell mode respectively.

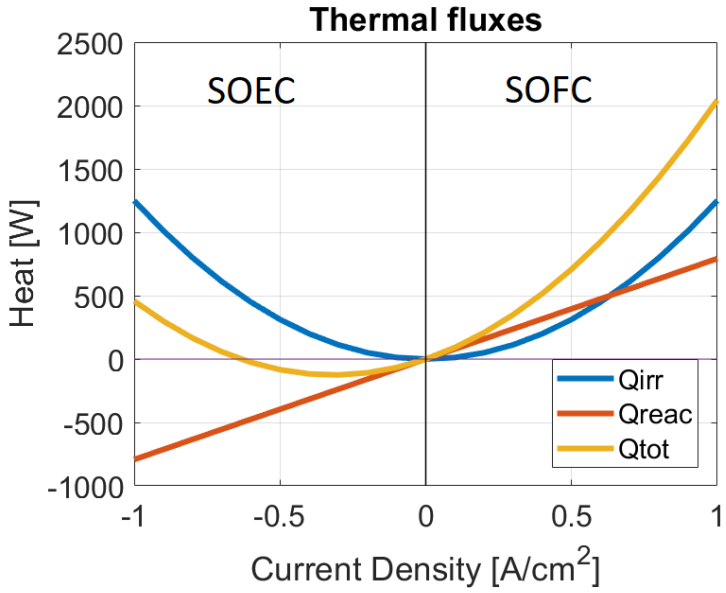

Figure 22 - Heat variation according to the current

When the system is in thermoneutral condition the total heat is equal to zero.

Lastly has been calculated the mass flow rate, in electrolysis mode is not considered the air utilization because is not needed an excess of air.

$$\dot{m}_{o_2} = \frac{I \cdot n_{cell}}{F \cdot n_{F_{O2}}} = \frac{50 \cdot 25}{96485 \cdot 4} = 0.0032 \frac{mol}{s} \cdot 32 \frac{g}{mol} = 0.1036 \frac{g}{s} \quad (82)$$

$$\dot{m}_{air} = \frac{\dot{m}_{o_2}}{0.21} = 0.0154 \frac{mol}{s} \cdot 28.84 \frac{g}{mol} = 0.4448 \frac{g}{s} \quad (83)$$

The input electrical power required is calculated as follows:

$$P = V \cdot i \cdot S \cdot n_{cell} = -1.620 \ kW \quad (84)$$

3.3.2 Geometry description

The helix of the geometry has been compacted more, as most of the heat is exchanged in the region closer to the stack.

Moreover, looking at the previous electrochemical calculations, it is clear that in electrolysis mode there is only absorption of heat but there is no way to supply it, thus a heater has been added to the model (until now, only exothermic fuel-cell mode was modeled where no heater was needed). Therefore there will be a heat source inside the heater in electrolysis mode in order to sustain the reaction and to keep the temperature of operation. This heater has been built as an effective porous media made of stainless steel and it has been located on the stack, so the pipe of the heat exchanger goes through it.

The heater has been added above the stack (Figure 23), in order to exploit the conductive heat transfer, and to well pre-heat the air that enters in the stack from the helix. In this case, the Stainless Steel layer is located around the heater and the side walls of the stack, because it also the heater has been defined as a porous media.

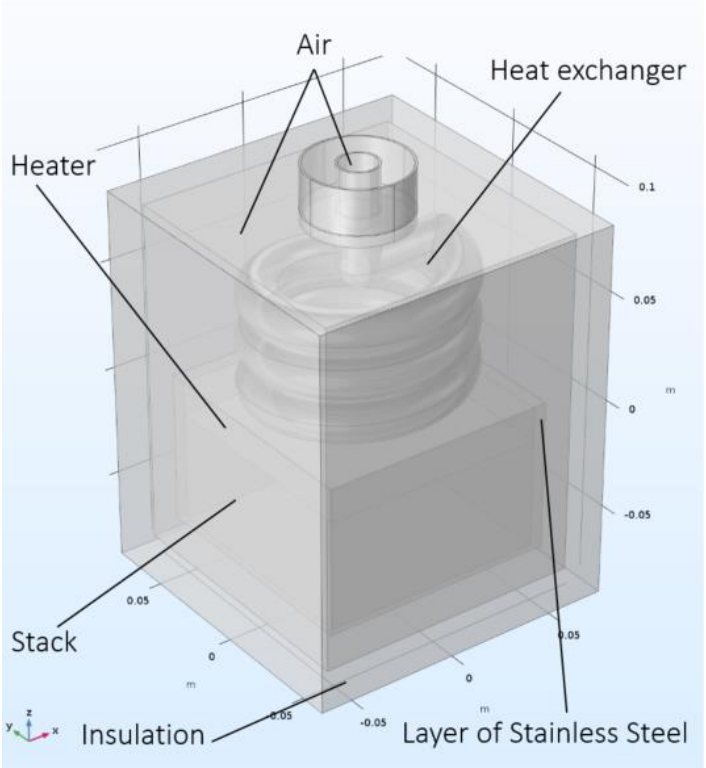

Figure 23 - 3D geometry of the model

Maintaining the same model with the previous data, the temperature of the stack in fuel cell mode was too high, therefore the parametric sweep has been done for some data, both for the fuel cell and for the electrolysis mode, in order to get the best configuration.

3.3.3 Parametric studies

The main difficulty encountered in the construction of these models, has been to find a way to cool the stack in fuel cell mode, otherwise too hot. For this reason, parametric studies have been performed in order to study which parameters can be used to control the heat and the temperature of the system.

Here below are the graphs that show the parametric sweep for both electrolysis and fuel cell mode with the same ranges of the parameters except for the overblow.
The parameters that have been fixed are:

- Insulation thickness equal to 0.02 m for both fuel cell and electrolysis mode
- Insulation thermal conductivity equal to 0.1 $W/m/K$ for fuel cell mode and equal to 0.04 $W/m/K$ for electrolysis mode
- Overblow equal to 10 for fuel cell mode and 2 for electrolysis mode
- Convective heat transfer coefficient outside the system equal to 40 $W/m^2/K$ for fuel cell mode and equal to 20 $W/m^2/K$ for electrolysis mode

The fixed value of the convective heat transfer coefficient is different for fuel cell and electrolysis, this is due to the fact that cooling is required in the fuel cell mode. This means that in real life during fuel cell mode a forced convection is necessary, in fact, increasing the velocity of the air supplied to the outside walls of the system, the value of the heat transfer coefficient increases as well. Instead, in electrolysis mode there is no need of forced convection, this means lower velocity of the outside air and lower value of convective heat transfer coefficient.

The y-axis T represents the average temperature in the stack volume, the aim is to cool the stack in fuel cell mode and to heat it up in electrolysis mode, so the final configuration will be a tradeoff between the two modes of operation.

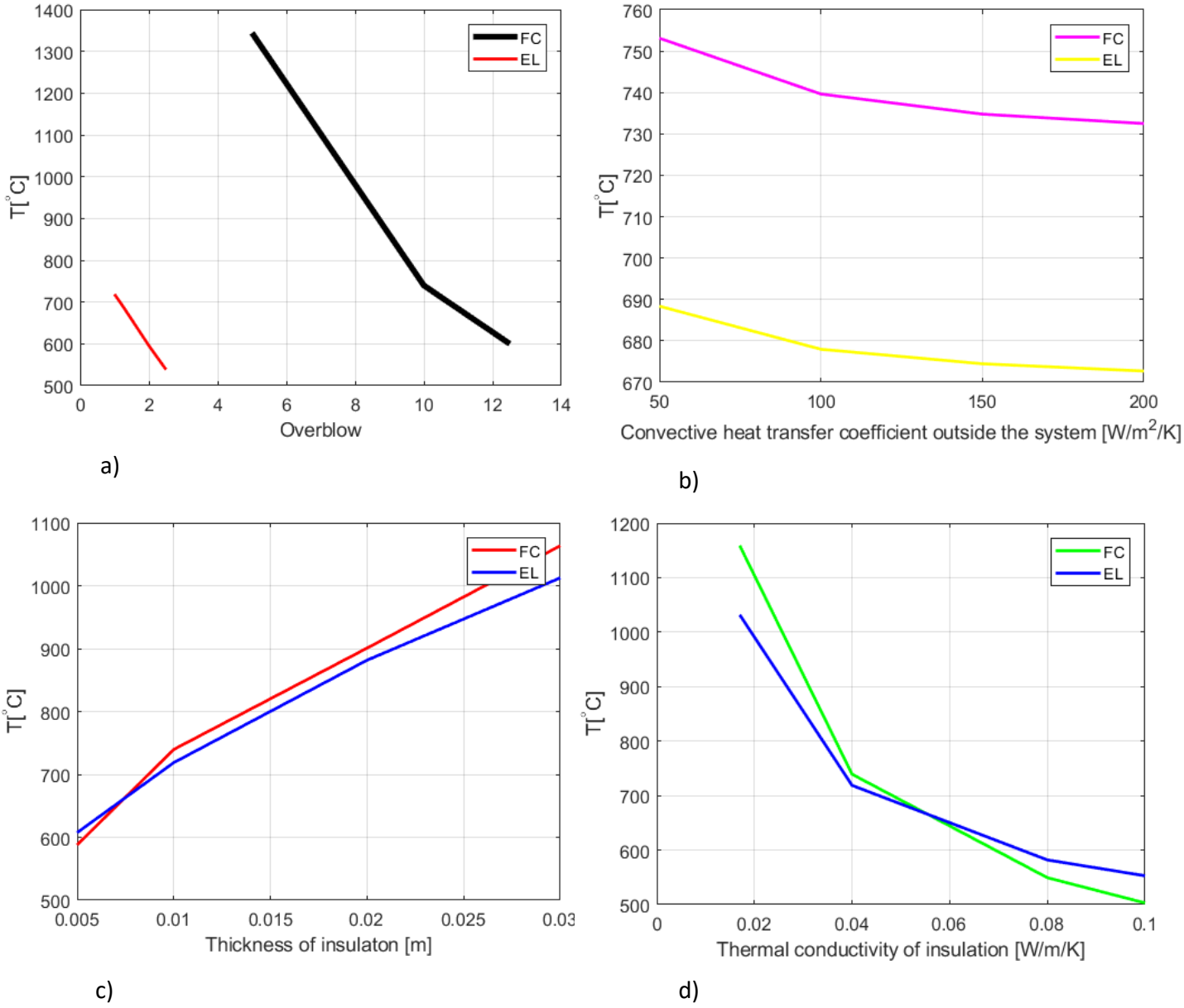

Figure 24 - Parametric sweep for the overblow (a), the convective heat transfer coefficient (b), the thermal conductivity (c), and the thickness of the insulation (d)

From these images (Figure 24), it is possible to notice that the overblow is the strongest parameter able to cool down the stack in fuel cell mode.

Starting from these graphs, the configurations for electrolysis and fuel cell mode have been chosen, maintaining the geometry constant in the two models.

The next section presents the three different models with the parameters based on the graphs above.

In table 7 are shown the geometric parameters of the models, and all the values are in cm.

Table 7 - Geometric parameters of the model constant for the three mode of operation

Parameter	Value
Inner radius	0. 8
Outer radius	2.2
Height of the stack	5
Side of the stack	10
Thickness of the SS layer	0.3
Thickness of the pipes	0.1
Thickness of the insulation layer	1
Height of the heater	1.5
Side of the heater	10
Major radius of the helix	3.5
Minor radius of the helix =Inner radius	0.08
Axial pitch of the helix	2
Width and depth of the air box	12
Height of the air box	14.5

3.3.4 Model description

Fuel cell mode

The model has been adapted to the parametric sweep, the geometry of the stack required, the mass flow rate, and the heat released or absorbed.
Therefore since the heat management and the flow rate requested differ for fuel cell mode and electrolysis mode, different models have been built.

In the fuel cell mode the direction of the flows has been reversed, in fact, the air enters in the system in the outer region, where is fixed the Dirichlet boundary condition of 20°C; it goes down, it enters in the stack from below where is absent the layer of stainless steel, and goes up in the pipe. The heat generation has been imposed as a general heat source of 709 W inside the stack, a strong convective heat flux on the external walls has been set with air at room temperature, and the air utilization has been strongly increased in order to cool the system.

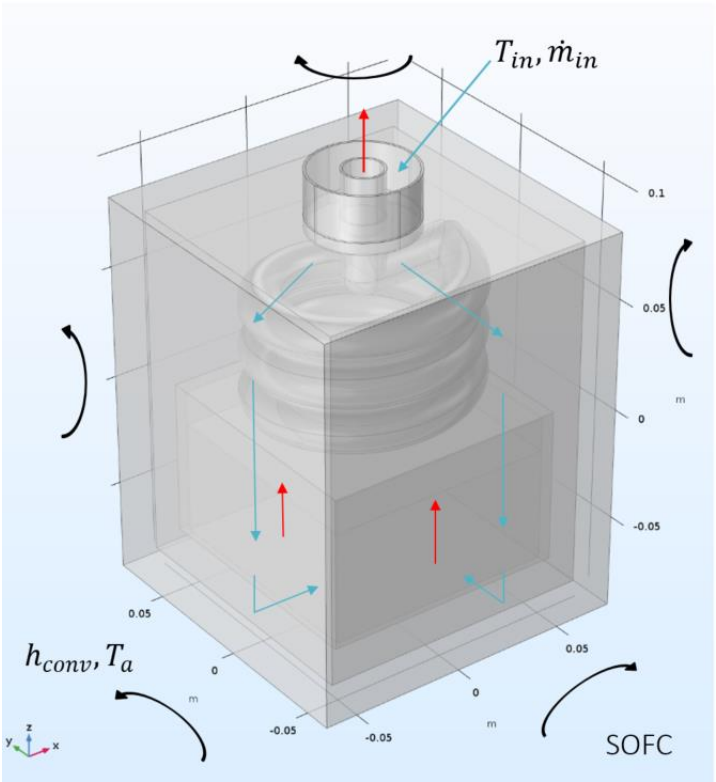

Figure 25 - Operating condition in Fuel cell mode

The initial condition for the flow are set as:

- $U_z = -1, U_x = 0,\ U_y = 0$ for the outer pipe and the outer channel of air
- $U_z = 1, U_x = 0,\ U_y = 0$ for the inner pipe (the helix) and the stack

The initial condition for the heat transfer is imposed at 20℃.

Dirichlet boundary condition has been imposed at the fluid inlet in the outer pipe. In order to make these models converge, the study is in steady state and it has been split in two steps, one for the fluid flow physics with a direct (MUMPS) segregated step solver, and the other one for the heat transfer with a direct (PARDISO) Fully Coupled solver. The computational time for the solution of the first step was much higher than that of the second one.

Table 8 - Operating and boundary conditions for the FC model

Operating conditions		
Parameter	Value	Units
T_{in}	20	℃
T_a	20	℃
$\dot{m}_{in}$	4.45e-3	kg/s
$Overblow$	10	$-$
h_{conv}	100	$\frac{W}{K \cdot m^2}$
Q_{stack}	709	W
Q_{heater}	0	W
$Fluid\ material: O_2$		
$Molar\ Weight$	32	$\frac{kg}{kmol}$
k_{ins}	0.04	$\frac{W}{K \cdot m}$

Electrolysis mode

In the electrolysis model, the air enters the inner pipe, then the air goes down through the helix, and through the stack that is a porous media; finally it comes out from the stack from below and goes up again in the outer region exchanging heat with the incoming air. The heat absorbed has been imposed on the stack as a general source of -84 W in the heat transfer physics, based on equation (80).

In electrolysis mode the heater has a heat source inside of it that should supply heat to the stack, the power in the heater is more than the heat absorbed by the stack because it is needed to support the reaction, but also it should keep the stack at the temperature of operation, considering heat losses through the insulation and in the heat exchanger.

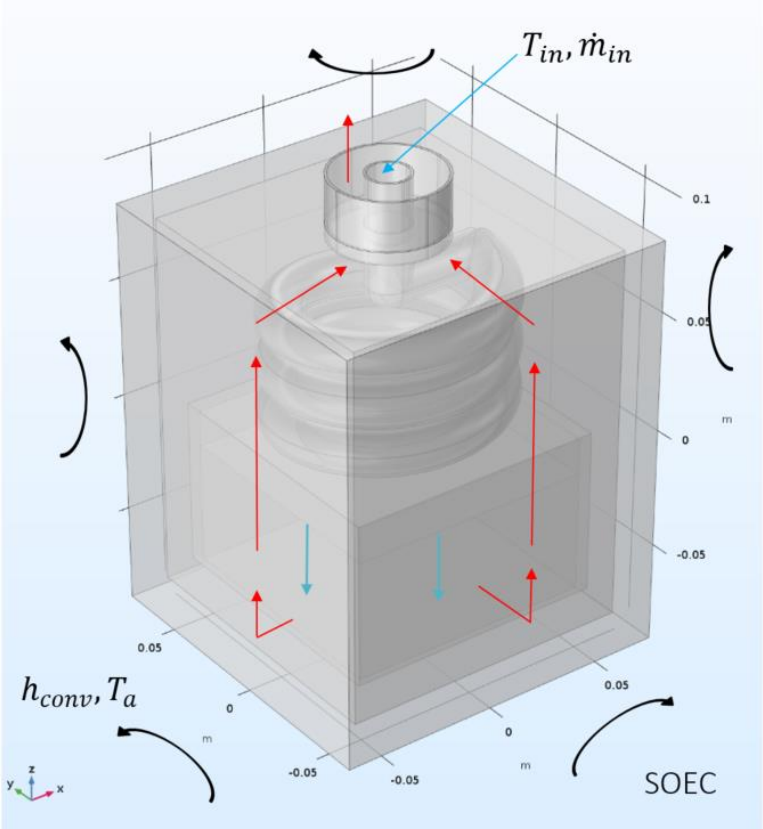

Figure 26 - Operating condition in Electrolysis mode

The initial condition for the flow are set as:

- $U_z = 1, U_x = 0,\ U_y = 0$ for the outer pipe and the outer channel of air
- $U_z = -1, U_x = 0,\ U_y = 0$ for the inner pipe (the helix) and the stack

The initial condition for the heat transfer is imposed at 20℃.

Dirichlet boundary condition of 20°C has been set at the fluid inlet in the inner pipe. In this case, the mass flow rate corresponds only to the oxygen and the overblow is taken equal to 1, thus the flow rate is only the stoichiometric amount of Oxygen.

The study is steady state and it has been split in two steps as before, and the solvers were kept the same.

The fluid flow physics has a segregated step scheme with a direct (MUMPS) solver, instead the heat transfer in porous media physics is solved with a direct solver (PARDISO) in fully coupled scheme.

Table 9 - Operating and boundary conditions for the electrolysis mode model

Operating conditions		
Parameter	Value	Units
T_{in}	20	°C
T_a	20	°C
$\dot{m}_{in}$	1.0364e-4	kg/s
$Overblow$	1	$-$
h_{conv}	20	$\frac{W}{K \cdot m^2}$
Q_{stack}	-84	W
Q_{heater}	210	W
$Fluid\ material: O_2$		
$Molar\ Weight$	32	$kg/kmol$
k_{ins}	0.04	$W/(K \cdot m)$

Idle mode

The idle case model has been built (Figure 27), in which no air is needed since no reaction occurs, therefore, the inlet and the outlet of the fluid in the free flow physics have been disabled; a heat source has been imposed in the heater to maintain the temperature of operation of the stack in order to avoid thermal cycles in idle periods.

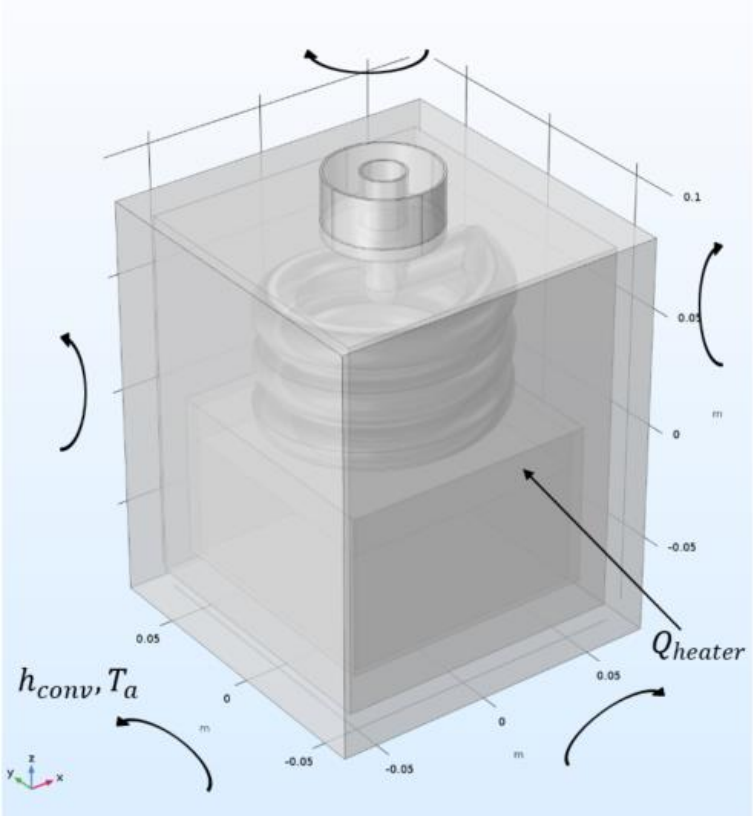

Figure 27 - Operating condition in idle mode

The initial condition is set at 20 °C on the whole domain. In this model there is only the heat transfer physics, no fixed temperature has been set, thus in all the boundaries around the system has been imposed a convective heat flux. Therefore the boundary condition of Dirichlet is not set, but instead that of Neumann.

This model is solved in just one step, with a direct (MUMPS) Fully Coupled solver.

Table 10 - Operating and boundary conditions for the idle mode model

Operating conditions		
Parameter	Value	Units
h_{conv}	15	$\frac{W}{K \cdot m^2}$
T_a	20	°C
Q_{heater}	110	W
k_{ins}	0.04	$\frac{W}{K \cdot m}$

3.3.5 Results

EXOTHERMIC FUEL CELL MODE

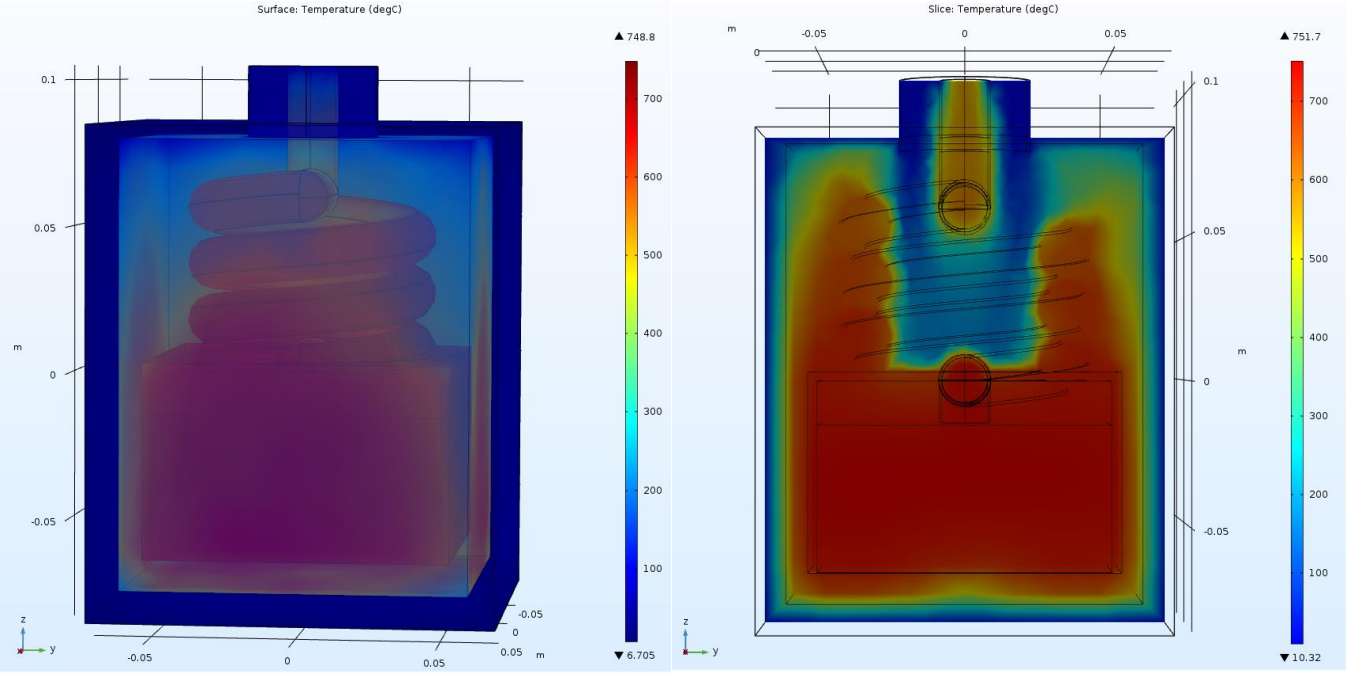

Figure 28 – 3-D view (a) and cross section (b) of the model working in fuel cell mode

The ASR is assumed as constant and not depending on the temperature.

The Figure 28 represents the heat maps of the model in fuel cell mode, the first image (Figure 28a) is the 3D view, second one (Figure 28b) is the cross-section of the model, both of them show the temperature distribution.

Looking at them it is possible to notice that the air that enters in the stack is completely pre-heated, but the air that comes out is at 500°C, so it is not well cooled by the time it reaches the outlet. The heater, in this case, does not have any heat source, it behaves like a sensible heat storage.

The convective heat transfer coefficient for the convection on the external walls is very high, which means that the convection is forced, therefore, a further component is needed outside the system (e.g. a fan). Also the overblow of air is very strong, in order to cool as much as possible.

Moreover, the insulation thickness is very thin, because if the system is too insulated the cell will overheat since the heat is unable to get out.

As it is possible to see from the cross-section of the model, there is an almost-still air in the center of the helix that is not exchanging heat optimally, thus the pipes of the helix should be more detached from each other to allow more air to pass and then exchange heat (shown in Appendix A.1-2).

ENDOTHERMIC ELECTROLYSIS MODE

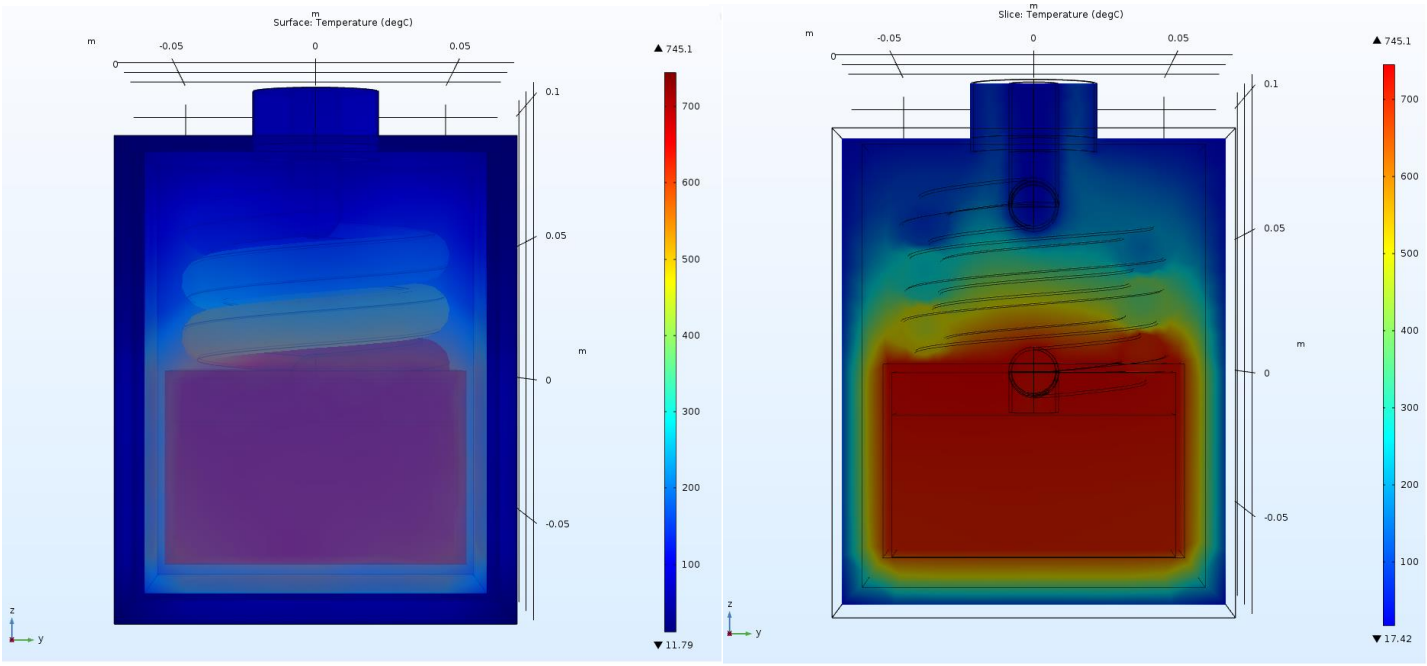

Figure 29 – 3-D view (a) and cross section (b) of the model working in electrolysis mode

In the Figure 29 are represented the cross-section and 3D view of the geometry; they show the temperature distribution in the whole domain for the base case of the model with the corresponding parameters for electrolysis mode.

The heat that has been supplied in the heater (210 W) is quite high if compared to the heat needed for the reaction (84 W), this is because the system is not very well insulated; in fact, the thickness of the insulation is very thin and as a consequence there are a lot of losses towards outside. The choice of the thin insulation was a tradeoff between the cooling needs in exothermic fuel-cell mode and this endothermic electrolysis mode, as mentioned earlier when discussing the parameter variations.

In this model, the air that enters in the stack is completely pre-heated, and the air at the outlet is at ~65°C, so it is almost completely cooled.

IDLE MODE

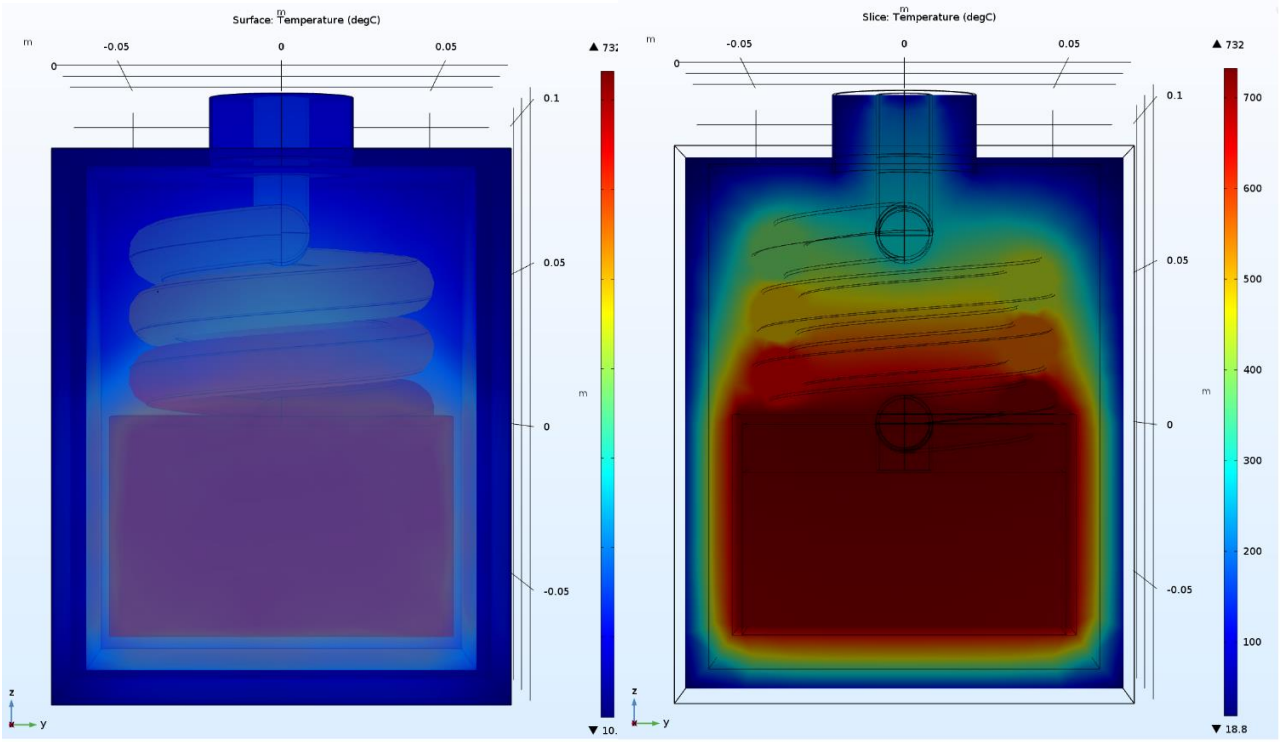

Figure 30 – 3D view (a) and cross section (b) of the model in idle mode

It is possible to notice from Figure 30, that the cooling in the upper part of the pipe is less impactful with respect to the other models. In this model it has been applied only Neumann boundary conditions on the external walls, thus just convective heat flux with a low convective heat transfer coefficient; for this reason the impact of the cooling is less than in the model with Dirichlet boundary conditions. The fixed boundary condition has been disabled because the air at 20 °C is not entering, in fact, in the idle case there is no reaction, therefore, there is no mass flow rate in inlet or in outlet and the initial values of the velocity is 0 in the whole domain.

The heat supplied (110 W), is the heat required by the system to keep the stack at the operation temperature, in fact, the amount of heat is much less than in the electrolysis mode since there is no absorption of heat by the endothermic electrolysis reaction.

3.4 CASE 4: Integrating PCMs

Afterwards, the heater has been replaced by a PCM in order to make the system self-sustained and to improve the thermal management of the SOIARB, making it more isothermal and avoiding thermal cycles during idle periods.

The phase change taken into consideration is liquid-solid, since the gas-liquid transition is impractical due to the resulting high pressures or high volumes. In a phase change transition, structural and mechanical properties of the material in question change.

The PCM absorbs the heat released from the stack in fuel cell mode, melting and turning the heat released into latent heat, which is absorbed by the stack in electrolysis mode as the PCM solidifies again.

The two materials which are taken into consideration are Aluminum metal and Magnesium Chloride, chosen based on their appropriately high melting points and high latent heat of fusion.

Adding the PCM to the model, the system has been switched from steady-state to transient. The PCM is a feature of the Heat Transfer module of the Comsol software [20].

3.4.1 Aluminum

The Aluminum is an inorganic PCM and it is a metal, it has a very high thermal conductivity, which allows fast charge or discharge rates.

Volume has more importance than the mass in design process of a system, and the volumetric latent heat of Aluminum is very high. On the other hand, Aluminum is more expensive with respect to the Magnesium Chloride.

According to [22], 79-80% of the total energy stored by a TES of Aluminum, with a 100 ℃ range of temperature that includes the melting point, it is attributed to the latent heat.

The melting temperature of the Aluminum is lower than the target RSOC operation temperature of ~700 °C, so the stack has to work at lower temperature, but this increases the ASR and as a consequence the stack cost.

Data of Aluminum according to [22] :

Table 11 - Physical and thermal properties of Aluminum

Physical and Thermal properties of Al			
Parameters		Value	Units
Density	Solid (at 25℃)	2700	$\frac{kg}{m^3}$
	Liquid (at 660℃)	2375	$\frac{kg}{m^3}$
Melting Temperature		660	℃
Heat of Fusion		397	$\frac{kJ}{kg}$
Specific Heat Capacity	Solid (at 500℃)	1.85	$\frac{kJ}{kgK}$
	Liquid (at 660℃)	1.177	$\frac{kJ}{kgK}$
Thermal Conductivity		237	$\frac{W}{mK}$

It is possible to calculate the volumetric latent heat of the material:

$$E_{Al} = \bar{\rho} \cdot Q_{latent} = \quad 1007.4 \qquad MJ/m^3 \tag{85}$$

EXOTHERMIC FUEL CELL MODE

First the fuel cell mode has been studied with the PCM height H=0.015 m, the contact surface area of the PCM and the stack is maintained constant, equal to S=100 cm^2.

The first study has been done using the Aluminum as heat storage medium, therefore it has been defined in the heat transfer in porous media physics as phase change material.
Moreover, it has been defined twice in the materials, once as a solid and once as a liquid; both of them have been assigned to the same domain overwriting it, and, as was mentioned previously, the phase transformation has been considered in the heat transfer physics.
The geometry and the operating parameters have been retained those of the model with the heater, except for the overblow that for this first model has been set equal to only 1, and the mass flow rate corresponds to the stoichiometric oxygen needed to sustain the reaction. This low overblow of pure oxygen can be compared with the value of 10 required for air before (see Table 8) to provide sufficient cooling.
In the fluid flow physics the phase change material's domain is defined as porous media. The initial conditions have been set a:

- $U_z = -1, U_x = 0,\ U_y = 0$ for the outer pipe and the outer channel of air
- $U_z = 1, U_x = 0,\ U_y = 0$ for the inner pipe (the helix) and the stack

The initial value for the heat transfer physics is 20 ℃ for all domains except for the stack and the PCM, which has been set at 650 ℃; this value has been chosen because the transient in fuel cell mode starts with the PCM completely solidify, therefore it is needed a temperature under the melting point (660 ℃).
The phase change material velocity field has been imposed zero in all directions $U_z = 0, U_x = 0,\ U_y = 0$; the transition interval between phase 1 and phase 2 is $\Delta T_{1\to 2} = 10\ K$; the phase one has been coupled with the properties of the solid Aluminum; the phase two has been coupled with the properties of the liquid Aluminum; the ratio of specific heats has been assumed $\gamma = 1.1$ for both phases.
The study is transient and it has been split in two steps, one for each physics; both steps has been solved with a fully coupled scheme and a direct method (PARDISO).

The image below (Figure 31), is taken at the 925 s, thus during the phase change and it shows the distribution of the latent heat (first color-ramp column) only in the PCM domain, and of the temperature (second color-ramp column) in rest of the domain.

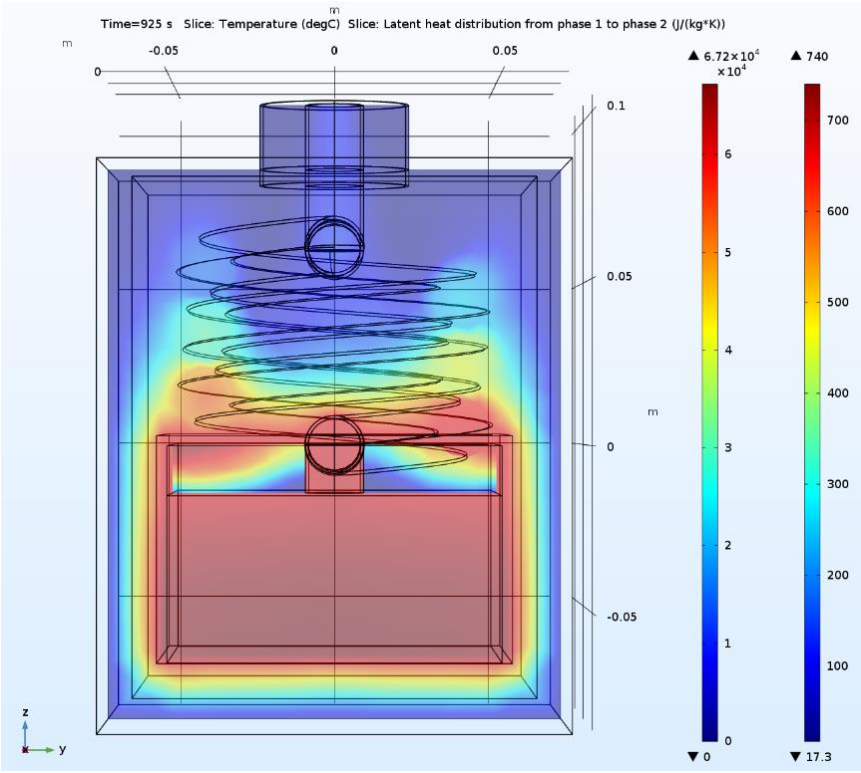

Figure 31 - Temperature and latent heat distribution in the cross section of the model working in FC mode, Image taken at 925 s in the simulation.

From Figure 31 it is possible to notice that the heat is well exchanged, in fact, the air that enters in the stack from below is completely pre-heated, and the air that flows out is completely cooled down.

The upper part of the domain is melting, but the lower part is not, this is due to the fact that the lower region is closer to the stack, and consequently to the heat source, as a result, it melts first, and since the picture is taken at 925 s, which is after the peak of latent heat, the lower part of the PCM is already melted.

Moreover, the PCM is defined as porous media in the Free Flow physics, as a consequence, the air from the stack can flow into the PCM and warm it up. After the first region has melted, the latent heat distribution moves to the upper region.

In the PCM volume, the temperature is the melting one. In the second column of the image, the maximum temperature is greater than 660 °C because the stack is always producing heat and therefore its temperature is higher than that inside the PCM.

At the end of the transient (~1000 s), the whole PCM is melted, but the stack is still releasing heat, so the temperature of the stack increases again. To store a higher amount of energy the volume of the phase change material should be higher.

In the figure below (Figure 32), the y-axis temperature represents the average temperature in the stack and in the PCM volume.

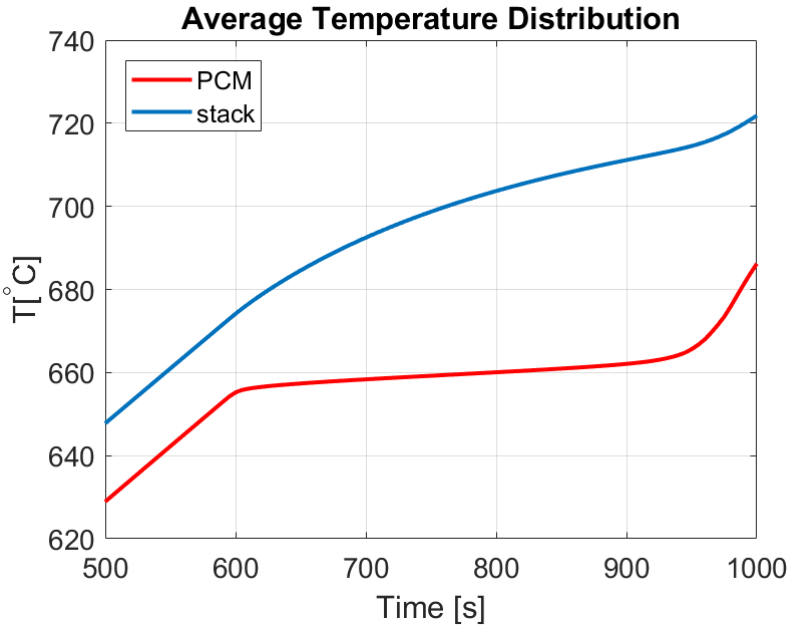

Figure 32 - Temperature evolution over time in the Al-PCM volume and in the stack volume

As it is possible to notice from the picture above (Figure 32), there is a big difference of temperature between the stack and the PCM (about 40°C). The x-axis of the image starts at 500 seconds because in the first part of the transient there is a decrease of temperature until 450°C for the PCM and until 550°C for the stack; then the system starts to heat up until the melting point. The phase change lasts for 400 seconds (from 590 s to 990 s) and in this time frame the PCM curve has a flat behavior for the whole phase change, as expected, whereas the stack curve has a less steep slope but it is not isothermal.

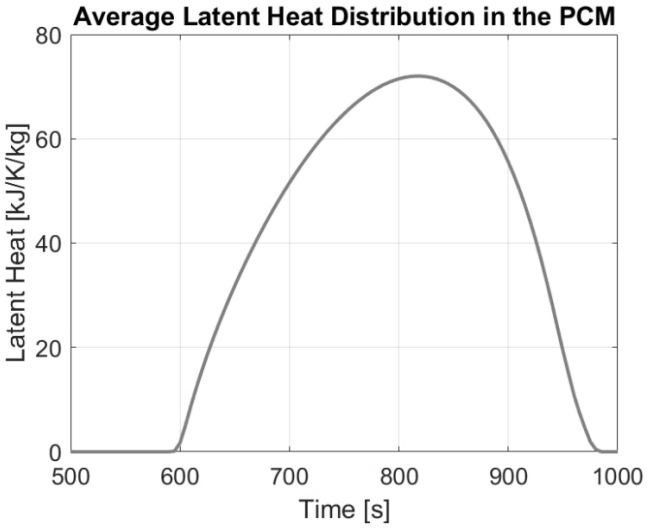

Figure 33 - Latent heat evolution over time in the AL-PCM volume and in the stack volume, in electrolysis mode.

Figure 33 shows the variation of the latent heat capacity over time. The y-axis latent heat is the average in the PCM volume. As it is possible to notice the transient in which is present the latent heat corresponds to the flat trend of the temperature in the previous graph. The total amount of stored energy is:

$$E_{Al} = \bar{\rho} \cdot Q_{latent} \cdot S \cdot H = 403 \ \ kJ \tag{86}$$

ENDOTHERMIC ELECTROLYSIS MODE

The simulation has been made using Aluminum, which has been defined in the heat transfer in porous media physics as phase change material; the velocity field is imposed equal to zero in all directions in that domain. The initial temperature of the PCM and of the stack has been imposed at 685°C, while the remaining geometry has initial condition of 20°C. These initial conditions have been set because the PCM is supposed to supply energy, so it should be already melted when the electrolysis operation starts.

In the fluid flow physics the initial conditions have been set:

- $U_z = -1, U_x = 0, \ U_y = 0$ for the outer pipe and the outer channel of air
- $U_z = 1, U_x = 0, \ U_y = 0$ for the inner pipe (the helix) and the stack

As in the previous model, two materials have been defined as Aluminum, one for each phase with the different properties, both with the same domain selected.

The study is time dependent and it has been divided into two steps, each step studies only one physics, the scheme solver for both steps is fully coupled, the solver for the fluid flow physics is direct (MUMPS) and for the heat transfer is direct (PARDISO).

Figure 34 shows the cross-section of the system working in electrolysis mode, it represents the transient simulation at 600 s, the first color-ramp column is the gradient of the latent heat in $\left[\frac{J}{kg*K}\right]$, and the second one is the range of temperature in [℃] .

From this picture it is possible to notice that the heat is well exchanged, as in the previous case, in fact, the inlet air is completely pre-heated, and at the outlet the air flows out at ~ 50℃, thus almost completely cooled.

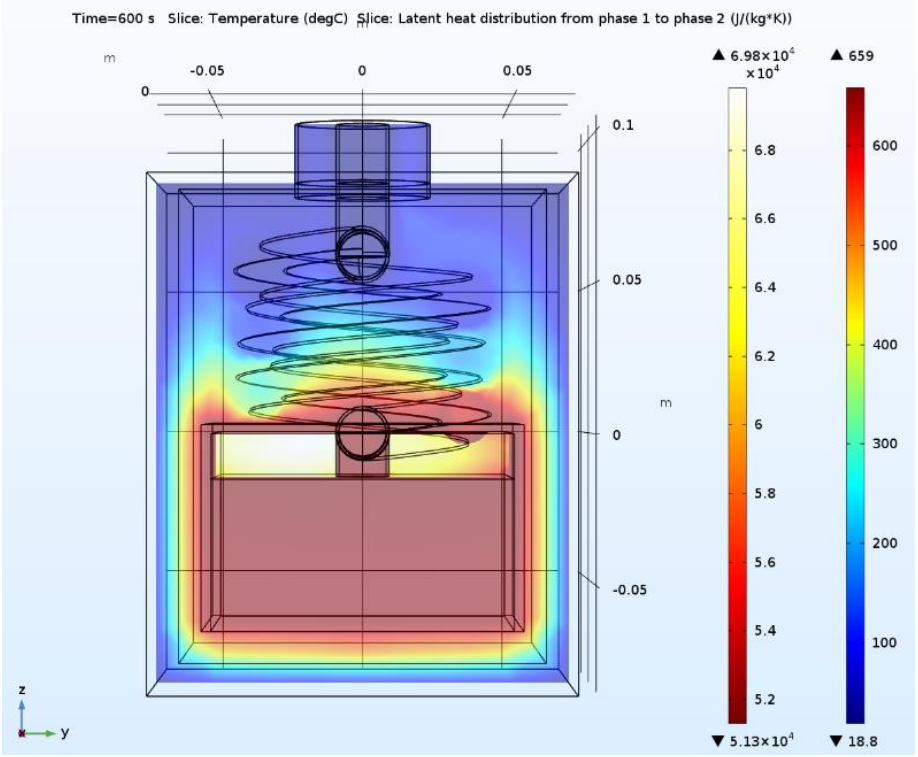

Figure 34 - Temperature and latent heat distribution in the cross section of the model that works in electrolysis mode, the image is taken at 600 s in the simulation.

In the figure below (Figure 35), the y-axis temperature represents the average temperature in the stack and in the PCM volume.

The transient lasts 800 s, much longer than in the fuel cell mode case. This can be explained by the fact that the thermal power released by the battery in exothermic mode is much higher in absolute value than the amount of heat absorbed by the stack in electrolysis mode of operation. For the same reason the difference between the two temperatures is much less than before, it is around 12°C, and the stack curve is flatter than in the fuel cell model.

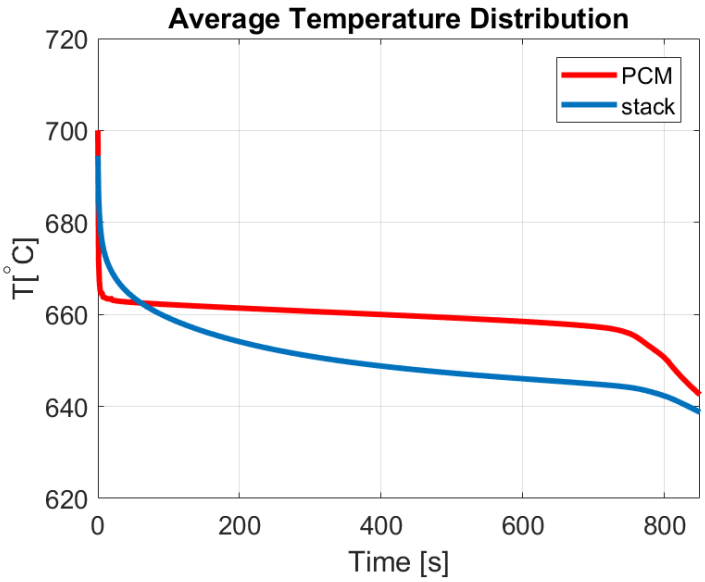

Figure 35 - Temperature evolution over time in the AL-PCM volume and in the stack volume. The system works in electrolysis mode

The temperature of the stack is always lower than that of the PCM, except for the first seconds in which the stack temperature is higher due to a higher thermal inertia of the Stainless Steel with respect to the Aluminum.

Afterwards, the PCM temperature is higher because it is the thermal sink and the stack is only absorbing heat. The temperature starts to decrease around 760 s, when the PCM is completely solidified.

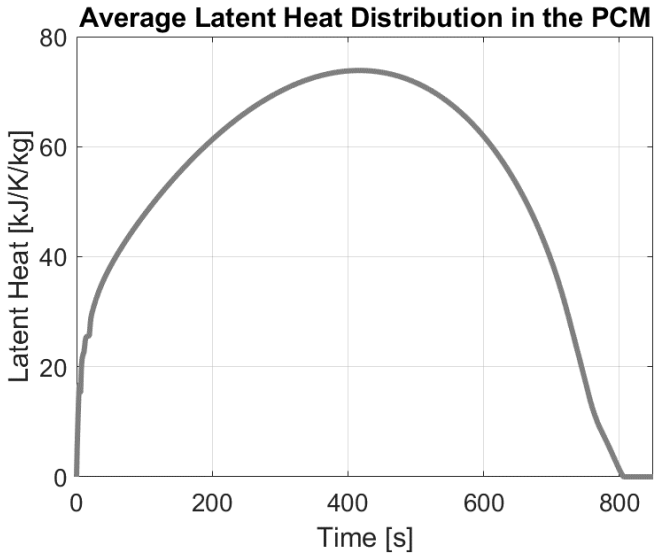

Figure 36 - Latent heat evolution over time in the AL-PCM volume and in the stack volume, in electrolysis mode

3.4.2 Magnesium Chloride

The Magnesium Chloride is an inorganic compound with formula $MgCl_2$, this material has been taken into account because it has a very high heat of fusion and it has the melting temperature very close to the target operating temperature of RSOC.
On the other hand, the $MgCl_2$ has a very low thermal conductivity, so it has to be combined with a higher-thermal-conductivity material, and it will need more heat transfer surface area.

Data of $MgCl_2$ according to [23]:

Table 12 - Physical and thermal properties of Magnesium Chloride [23]

Physical and Thermal properties of $MgCl_2$			
Parameters		Value	Units
Density	Solid (at 25℃)	2325	$\frac{kg}{m^3}$
	Liquid (at 714℃)	1680	$\frac{kg}{m^3}$
Melting Temperature		714	℃
Heat of Fusion		454	$\frac{kJ}{kg}$
Specific Heat Capacity		0.7602+1.65671*10^(-4)*T	$\frac{kJ}{kgK}$
Thermal Conductivity	at 714℃	0.46	$\frac{W}{mK}$

Energy density of the material:

$$E_{MgCl2} = \bar{\rho} \cdot Q_{latent} = 909.135 \quad \frac{MJ}{m^3} \tag{87}$$

The specific latent heat of the Magnesium Chloride is higher than the Aluminum one, but the latter has a higher density and, consequently, the total energy stored by Aluminum in a fixed volume is greater than that of the $MgCl_2$.

EXOTHERMIC FUEL CELL MODE

The simulation has been made using Magnesium Chloride, which has been defined in the "heat transfer in porous media" physics as phase change material.

As before, it has been defined twice in the materials, once as solid and once as liquid, with the respective properties, selecting the same domain for both materials.

The velocity field of the PCM is imposed equal to zero in all directions. The transition interval between the two phases has been set $\Delta T_{1\to 2} = 10\ K$, ratio of specific heats has been fixed $\gamma = 1.1$ for both phases.

The initial value of the temperature has been set at 20℃ in the whole domain except for the PCM and the stack, which have been set at 690℃, this value has been chosen because it is under the melting point of the PCM, and the PCM must be solid at the beginning of the fuel cell mode simulation.

The initial values for the fluid flow are the following:

- $U_z = -1, U_x = 0,\ U_y = 0$ for the outer pipe and the outer channel of air
- $U_z = 1, U_x = 0,\ U_y = 0$ for the inner pipe (the helix) and the stack

The study is time dependent and it has been split in two steps, one for each physics; both steps has been solved with a fully coupled scheme and a direct method (PARDISO). In the time depending solver of the second physics it has been fixed the maximum step equal to 5 seconds.

Total amount of stored energy from the PCM:

$$E_{MgCl2} = \bar{\rho} \cdot Q_{latent} \cdot S \cdot H = 136.37\ \ kJ \tag{88}$$

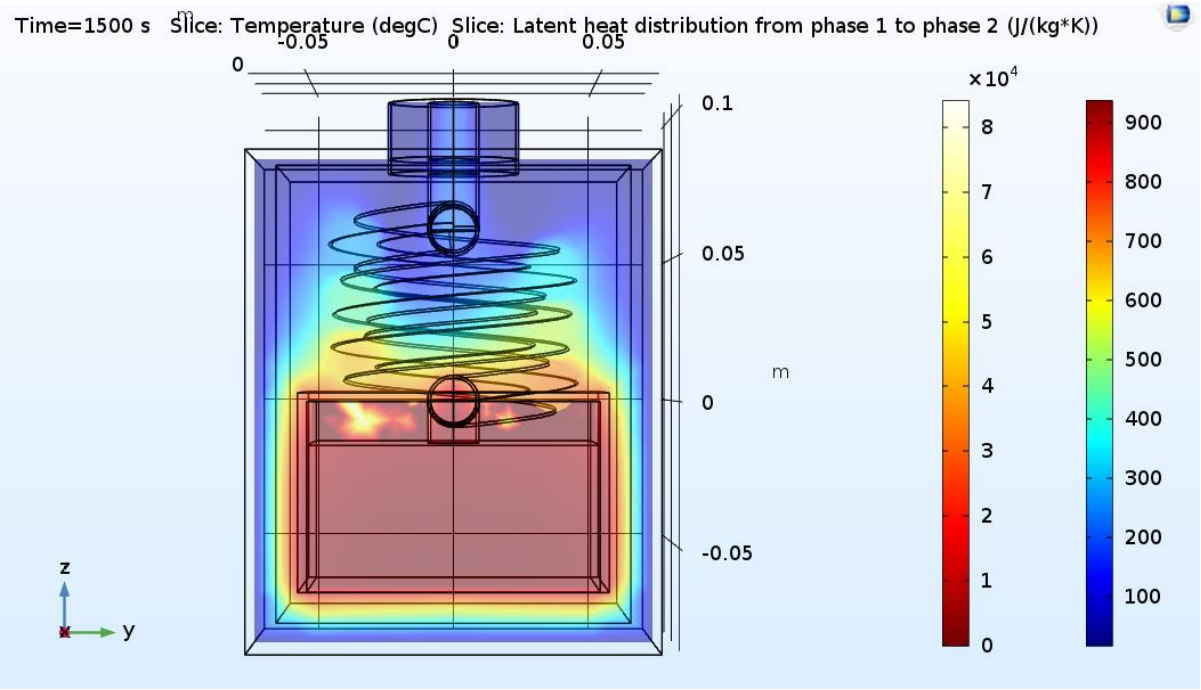

Figure 37 - Latent heat and temperature distribution in the cross section of the model that works in fuel cell mode, the image is taken at the second 1500

In the Figure 37 it is possible to notice, that the maximum temperature of the system is much higher than the melting one (maximum temperature = 940°C, melting temperature = 714°C), this means that the stack is overheated; the oxygen flows out at 160°C.

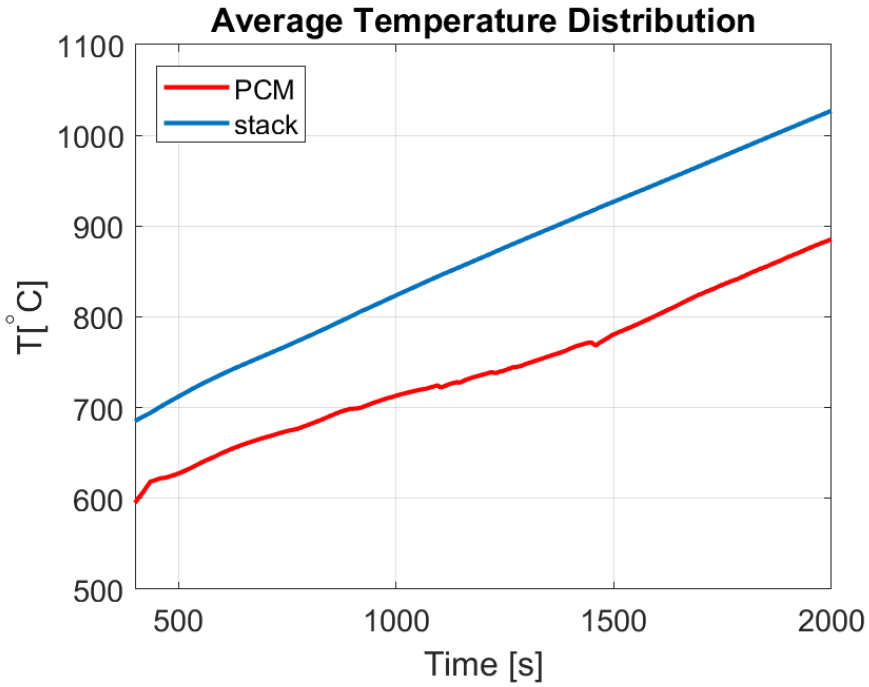

Figure 38 - Temperature evolution over time in the $MgCl_2$-PCM volume and in the stack volume. The system works in fuel cell mode

The Figure 38 represents the temperature over the time in the stack and PCM volumes. As it is possible to see, there is no flat trend, the curves increase almost linearly with the increasing of the time.

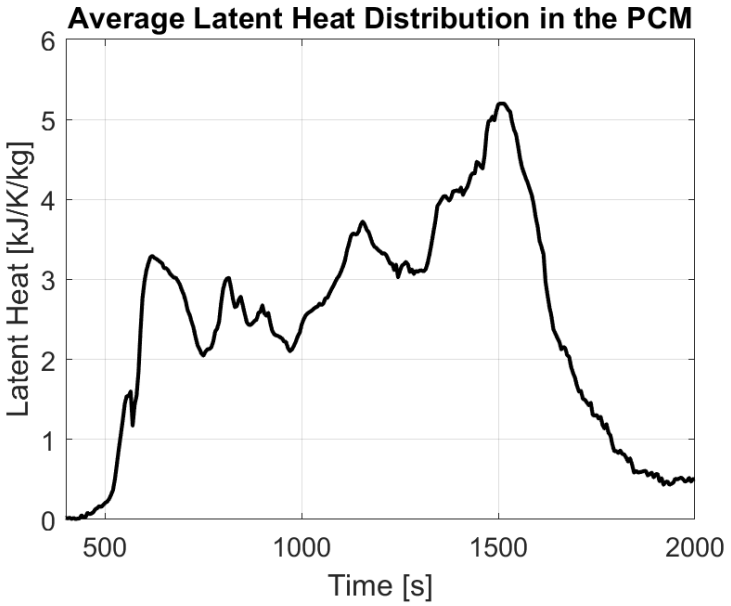

Figure 39 - Latent heat evolution over time in the $MgCl_2$-PCM volume and in the stack volume, in fuel cell mode

As it is possible to notice in Figure 39, the variation of latent heat of the Magnesium Chloride over the time is completely different from the Aluminum one, it is less uniformly. Moreover, the maximum value of the latent heat is lower than the Aluminum one, but the transient is longer. This is due to the lower thermal conductivity of the $MgCl_2$, in fact, the heat exchanged is less and, as a consequence, the material does not melt uniformly, requiring more time to melt all its volume. Therefore, the amount of latent heat is distributed during the transient, and so the peak is lower than the one of Aluminum.

ENDOTHERMIC ELECTROLYSIS MODE

An electrolysis mode simulation has also been done with the $MgCl_2$, in this case the initial value of temperature for the PCM and the stack is imposed at 750°C.

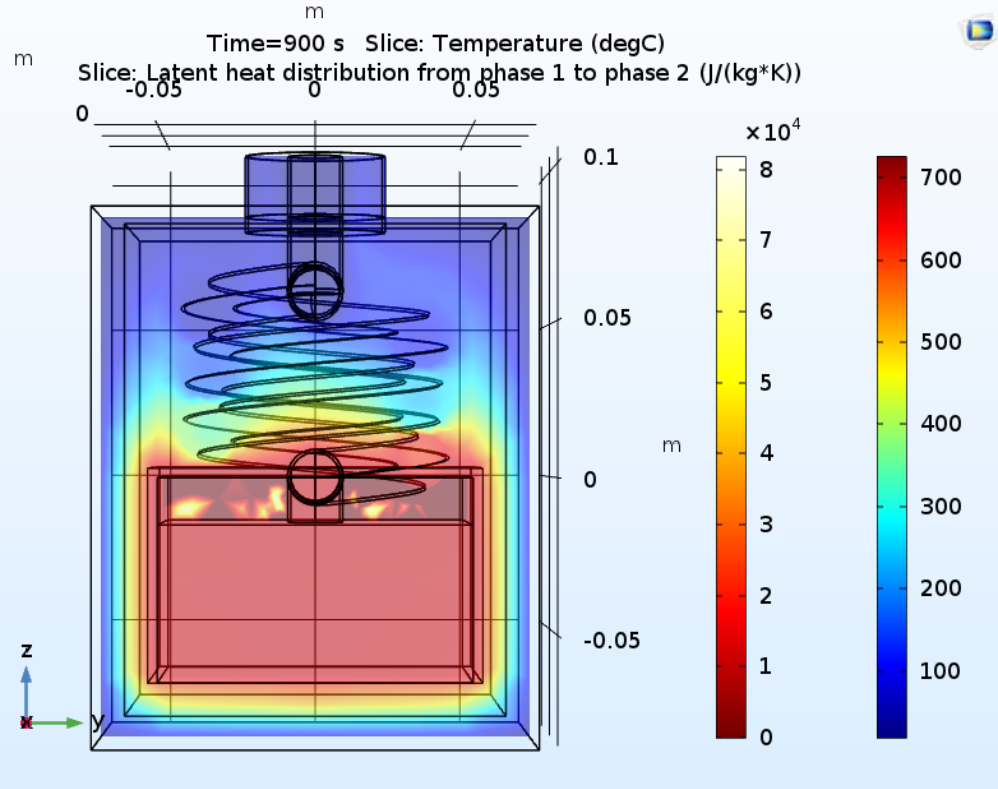

Figure 40 - Temperature and the latent heat distribution in the cross section of the model that has Magnesium Chloride as PCM, the system works in electrolysis mode

In this case, the cross-section has been taken at 900 s. $MgCl_2$ solidification lasts for ~1500 seconds, much more than the case with Aluminum as PCM. This phenomenon could be explained by the fact that $MgCl_2$ has a very low thermal conductivity (0.46 $W/(m \cdot K)$) with respect to the Aluminum one (238 $W/(m \cdot K)$) so the heat is not well transferred, as a consequence the low thermal conductivity increases the total heat transfer time required to melt or solidify the entire PCM.

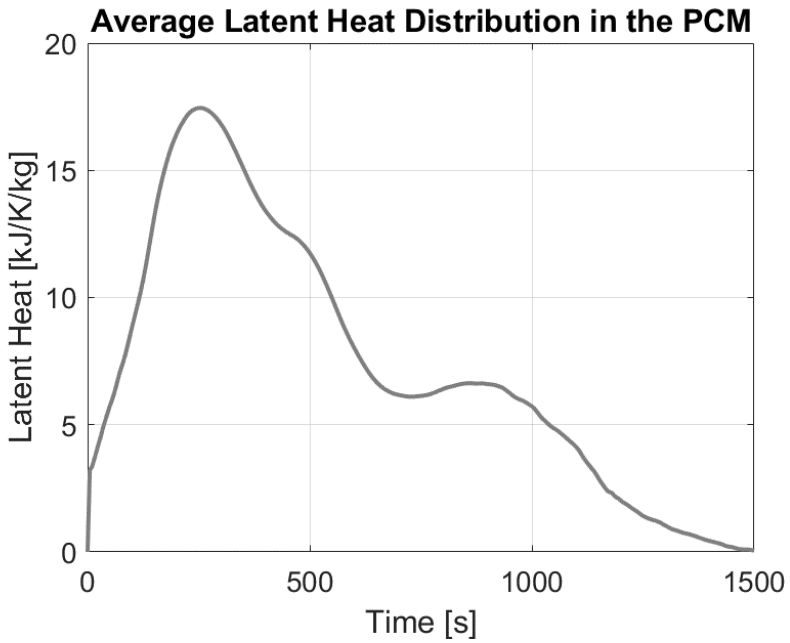

Figure 41 - Latent heat evolution over time in the $MgCl_2$-PCM volume and in the stack volume in electrolysis mode

As expected, the maximum value of latent heat is lower than the Aluminum one.

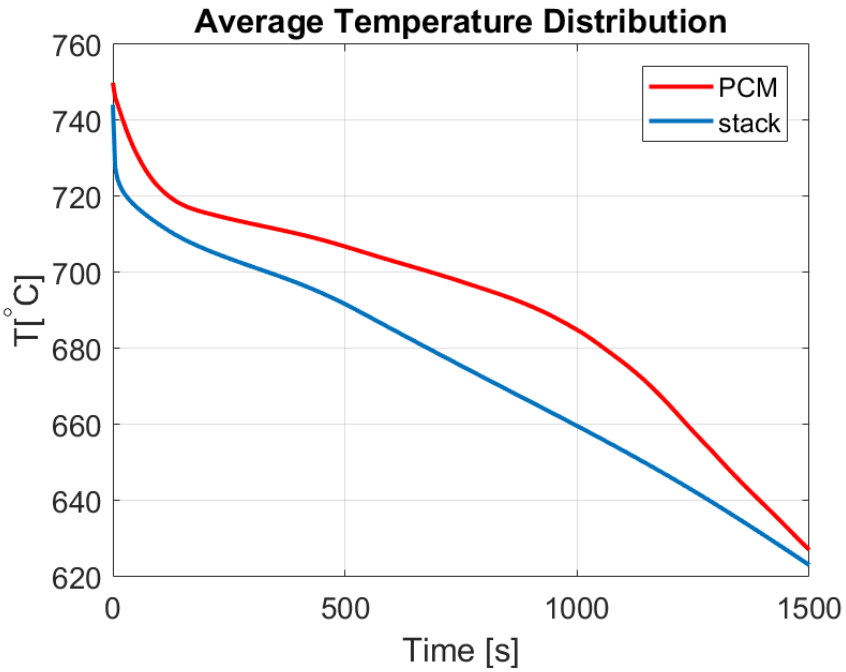

Figure 42 - Temperature evolution over time in the $MgCl_2$-PCM volume and in the stack volume in electrolysis mode

The trend of the temperature is not constant as in the other model with the Aluminum (Figure 32), but it decreases as the latent heat diminishes, and thus with the continuous solidification of the PCM.

The stack curve is decreasing almost linearly, this means that the PCM cannot sustain the electrolysis operation, in fact the temperature gradient of the stack during the transient is ≈100°C.

The slope of the PCM curve is less steep near the melting point, but it is not isothermal.

From Figure 42 it is possible to notice a different behavior from the model with Aluminum as PCM, in fact, the Magnesium Chloride is not a thermal sink at constant temperature; it is decreasing its temperature over the time.

Therefore, to investigate the challenge of using Magnesium Chloride, a simpler model has been built, a cylinder of Magnesium Chloride with a strong heat flux on the external walls, and the behavior has been studied by varying different parameters.

As expected, increasing the thermal conductivity of the material, the curve of the temperature change considerably:

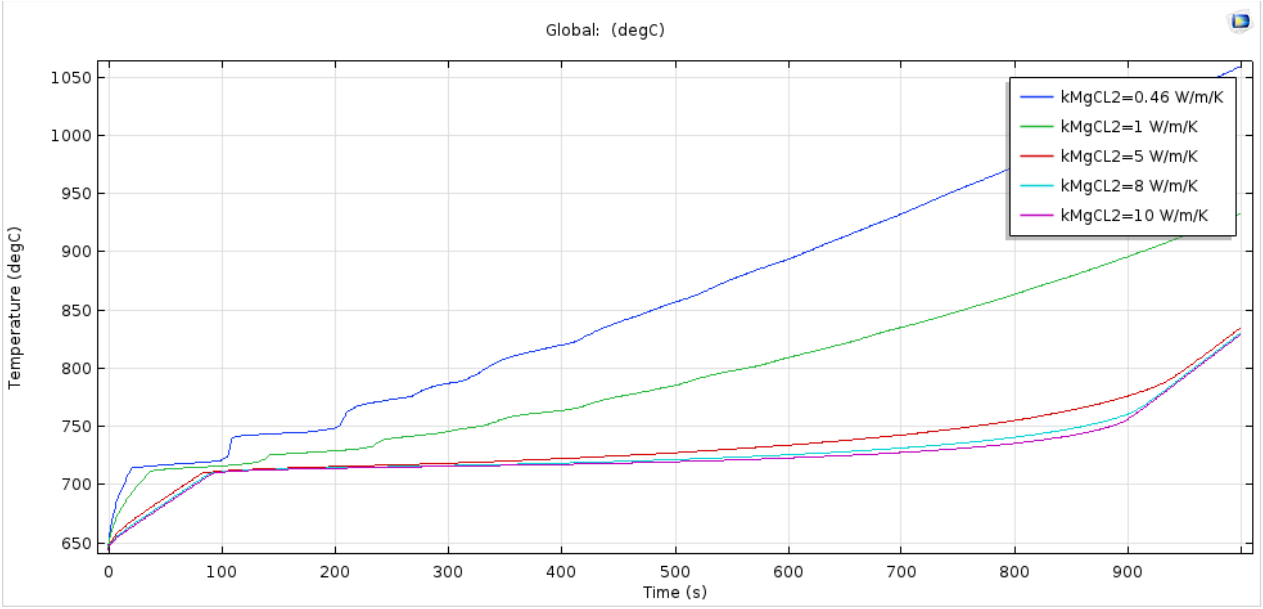

Figure 43 – Parametric sweep varying the thermal conductivity of the Magnesium Chloride in a simpler model

Thus, if Magnesium Chloride is used, it is necessary to increase the thermal conductivity of the material. There are several methods to do this, it is possible to use finned tubes, or to disperse the salt with particles with high thermal conductivity.

4. RESULTS

Both modes of operation have been analyzed (electrolysis and fuel cell modes) for both the PCMs that have been taken into consideration. As shown in the graphs of the temperature in the previous section, the Aluminum guarantees a better thermal stability.

It is possible to use Magnesium Chloride via mixing it with a higher thermal conductive material. This in turn, increases the heat transfer, and consequently a more uniform temperature distribution would be achieved. An alternative solution is to add more air pipes through the PCM. These solutions would decrease the volumetric latent heat capacity of the PCM, therefore a larger volume of PCM would be needed.

As a result, it has been decided to continue to analyze only the case with Aluminum. Figure 44 shows the temperature of the PCM and of the stack for an entire cycle charge-discharge of the battery.
This image has been done by putting together the plots of two independent simulations, one for each operating mode, so the simulation has not been performed reversibly.

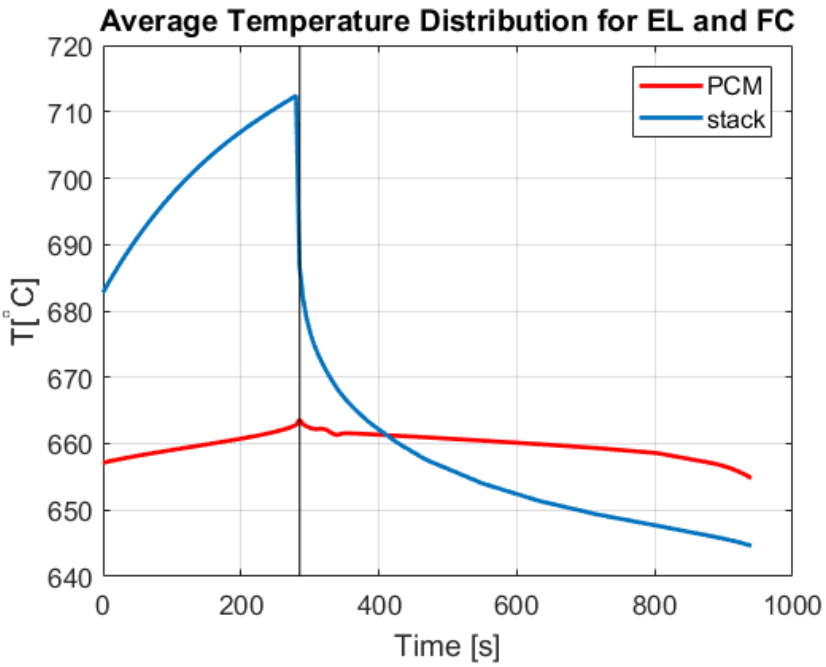

Figure 44 – Temperature variation over time during discharge and charge

The graph is divided by a black vertical line, which separates the two modes of operation. The left part of the graph represents the fuel cell mode of operation, which means discharge for the

battery but charge of the PCM that melts. The right part of the plot represents the temperature of the battery working in electrolysis mode, where the phase change material solidifies. The stack is no longer releasing but it is absorbing heat, this is the explanation for the immediate temperature change in proximity of the black line. Moreover, as mentioned before, the transient in electrolysis (EL) is longer than that of fuel cell (FC), since the amount released heat in FC is higher than the absorbed amount in EL. For the same reason the slope of temperature is steeper in FC mode than that of the EL mode.

The PCM temperature, as expected, has a flat behavior and it remains close to the melting point with small variations.

The amount of heat that is stored in the PCM is calculated as follows:

$$\phi_{stored} = Q_{latent} \cdot \bar{\rho} \cdot H \cdot S = 151.1\ kJ \tag{89}$$

- H is the height of the PCM

$$Q_{stored} = \frac{\phi_{stored}}{\Delta t} = 539.7\ W \tag{90}$$

- Δt is the duration of the phase change , in this case Δt=280 s

In the following equation the heat fraction is calculated as the ratio between the heat that is effectively absorbed by the PCM and the total heat released by the stack; the complementary of this fraction represents the heat lost by the system.

$$heatfraction = \frac{Q_{stored}}{Q_{stack-FC}} = 0.761 = 76.1\ \% \tag{91}$$

- $Q_{stack-FC}$ is the power heat released by the stack ≈ 709 W

4.1 Efficiency Analysis

In order to study the results of the model, the main parameter that has been taken into account is the round-trip energy storage efficiency of the system.

The round-trip efficiency of the system without the PCM and with only the heater:

$$\eta = \frac{P_{produced}}{P_{required} + Q_{heater}} = \frac{1000}{1620 + 210} = 0.546 = 54.6\ \% \tag{92}$$

- $P_{produced}$ is the power produced by the stack in discharge mode

- $P_{required}$ is the power required by the stack in charge mode
- Q_{heater} is the amount of power to sustain the reaction and the temperature of operation during the charge.

Integrating the PCM to the stack, the amount of heat supplied by the heater is covered by the heat released by the PCM during the EL mode. In fact, the system is self-sustainable, and the efficiency in this case is calculated as follows:

$$\eta = \frac{P_{produced}}{P_{required}} = \frac{1000}{1620} = 0.617 = 61.7\ \% \tag{93}$$

By integrating the phase change material the efficiency is enhanced, however, this efficiency is still lower than what was expected. Therefore, the variation of efficiency and power with different current densities has been studied.

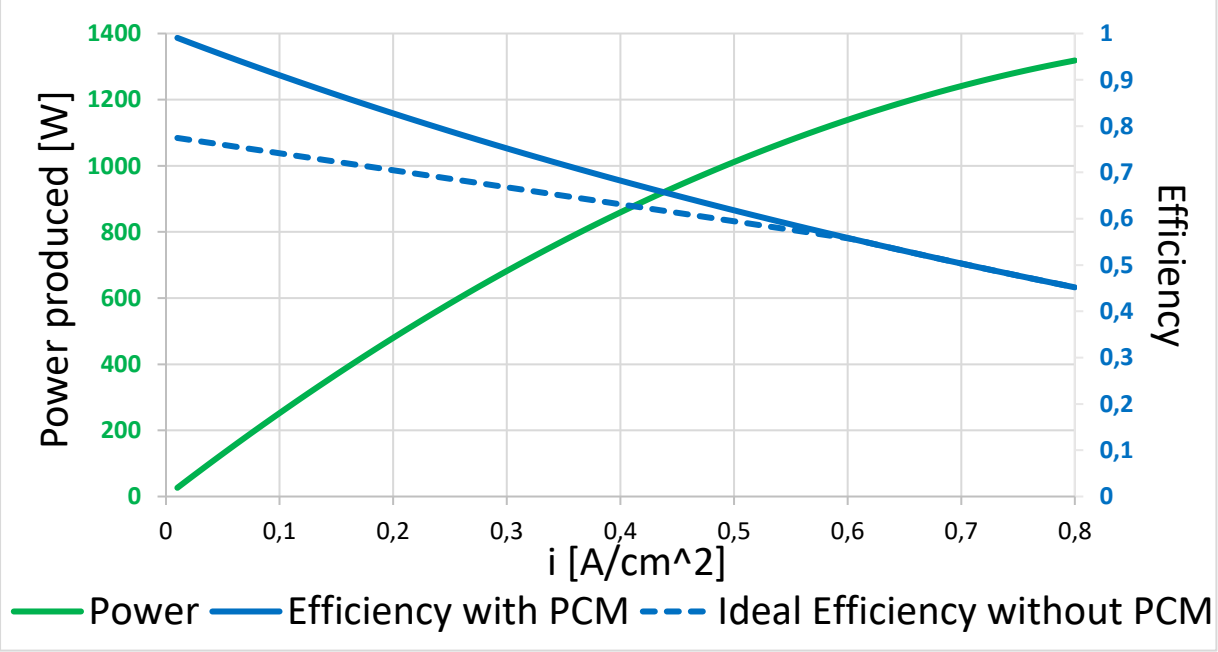

Figure 45 – Electric power produced and efficiency as a function of current density

The efficiency with PCM in Figure 45 is calculated assuming that all the heat needed by the stack in electrolysis mode is supplied by the thermal storage. The dashed line represents the ideal efficiency when a heater is used instead of the PCM. The ideal efficiency is computed by assuming that the heat required by the heater to sustain the reactions is the same as the theoretical needed by the stack, i.e. without taking heat losses into account. Therefore both efficiencies are calculated in ideal cases.

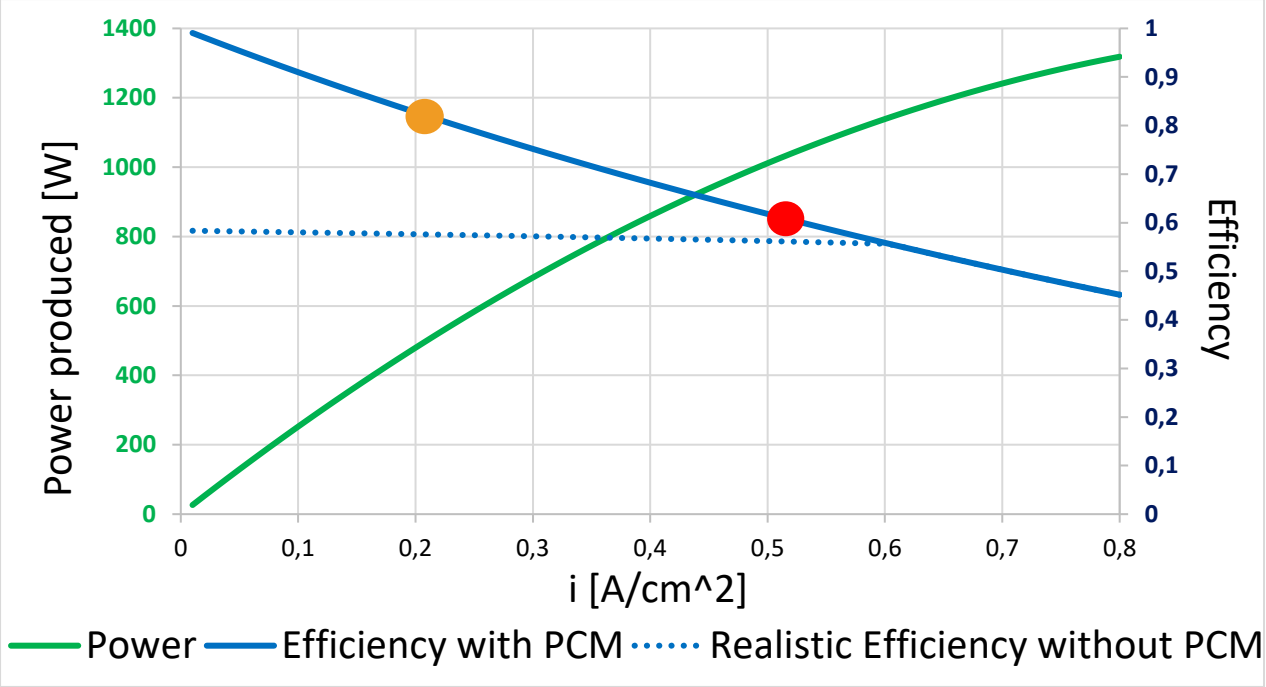

Figure 46 – Electric power produced and efficiency as a function of current density with the two operating conditions

In Figure 46, the efficiency with PCM is the same as in Figure 45. Instead, the efficiency without PCM is calculated assuming that the heat supplied by the heater is 2.5 times greater than the theoretical one required by the stack. This number is assumed constant for all the current densities, and it has been chosen by referring to the first model with the heater, where the heat source in the heater domain was 210 W, and the heat required by the stack was 84 W, thus, the ratio between these two values is 2.5.

As it is possible to see from the picture (Figure 46), the efficiency decreases with the increase of the current density, instead the electrical power increases with the current density. The blue line is the efficiency and, of course, the dashes curve that represents the efficiency without the PCM is always lower than the other one. The efficiency difference between with and without PCM increases with lower current densities because this means higher endothermicity, which can be covered by the PCM.

The red dot corresponds to the operating conditions taken into account, but the efficiency is not very high.

The orange dot instead, corresponds to a new operating conditions (i=0.2 A/cm^2) in which the efficiency is higher, but, on the other hand, to lower current density corresponds lower power produced. Therefore, in order to increase the efficiency while maintaining constant power production, a new configuration must be analyzed.

4.2 New configuration with higher roundtrip efficiency

The OCV and the thermoneutral voltage are constant because they depend on the Gibbs free energy and on the enthalpy of the reaction $Fe + ½O_2 \longrightarrow FeO$, and they vary only as a function of the temperature. Therefore, the reference temperature to calculate the OCV and the thermoneutral voltage is the melting point of the PCM, which is 660°C.

4.2.1 Fuel cell mode

Firstly the calculations for fuel cell mode has been done.

Table 13 – Data assumed for the electrochemical calculations for the fuel cell mode

Parameters	Value	Units
ASR	0.5	Ωcm^2
$P_{produced}$	1	kW
i	0.2	A/cm^2
S	100	cm^2
AU	1	–
h_{cell}	0.2	cm
$n_{f_{O2}}$	4	–
$n_{f_{Fe}}$	2	–
Δg_{react}	−204396,7	J/mol
Δh_{react}	−262684,6	J/mol

The open circuit voltage has been calculated following the Nernst equation:

$$OCV = -\frac{\Delta g_{react}}{F \cdot n_{f_{Fe}}} = 1.059\ V \tag{94}$$

$$V = OCV - i \cdot ASR = 0.909\ V \tag{95}$$

It is possible to size the stack deciding the number of cells needed in order to produce 1 kW of electric power.

$$n_{cell} = \frac{P}{V \cdot i \cdot S} = 52 \tag{96}$$

$$h_{stack} = n_{cell} \cdot h_{cell} = 10.4 \ cm \tag{97}$$

The height of the stack is more than the double with respect to the previous configuration.

Mass flow rate have been calculated using Faraday´s law:

$$\dot{n}_{O_2\,stoich} = \frac{i \cdot S \cdot n_{cell}}{F \cdot n_{F_{O2}}} = \frac{0.2 \cdot 100 \cdot 52}{96485 \cdot 4} = 0.002695 \ \frac{mol}{s} \tag{98}$$

$$\dot{m}_{O_2\,stoich} = \dot{n}_{O_2\,stoich} \cdot MW_{O2} = 0.002695 \ \frac{mol}{s} \cdot 32 \frac{g}{mol} = 0.086231 \ \frac{g}{s} \tag{99}$$

In case of fuel cell mode of operation, the stack will release the heat generated by the overvoltages and by the occurrence of the reaction.

$$|Q_{reaction}| = -\frac{T \cdot \Delta s_{react}}{F \cdot n_{f_{Fe}}} \cdot I \cdot n_{cell} = 314.14 \ W \tag{100}$$

$$|Q_{irreversibilities}| = I \cdot n_{cell} \cdot \sum_j \eta_j = 104 \ W \tag{101}$$

$$Q_{th} = \left(-V - \frac{\Delta h_{react}}{F \cdot n_F}\right) \cdot I \cdot n_{cell} = 418.14 \ W \tag{102}$$

4.2.2 Electrolysis mode

The reaction taken into account in electrolysis mode is $FeO \rightarrow Fe + ½O_2$.

Table 14 - Data assumed for the electrochemical calculations for electrolysis mode

Parameters	Value	Units
ASR	0.5	Ωcm^2
n_{cell}	52	$-$
i	-0.2	A/cm^2
S	100	cm^2
AU	1	$-$
h_{cell}	0.2	cm
h_{stack}	10.4	cm
$n_{f_{O2}}$	4	$-$
$n_{f_{Fe}}$	2	$-$
OCV	1.059	V
Δg_{react}	204396,7	J/mol
Δh_{react}	262684,6	J/mol

The open circuit voltage remains constant in the two modes of operation. The voltage is calculated as before, but it has a higher value in electrolysis mode because the current density is negative.

$$V = OCV - i \cdot ASR = 1.159\, V \quad (103)$$

$$V_{tn} = \frac{\Delta h_{react}}{F \cdot n_{f_{Fe}}} = 1.361\, V \quad (104)$$

The stack has already been sized in the section before, in fact, now the unknown is the power required by the stack in order to sustain the reaction of electrolysis.

$$P_{required} = V \cdot i \cdot S \cdot n_{cell} = 1205.6\, W \quad (105)$$

Working in electrolysis mode, the reaction will absorb heat and the overvoltages will produce heat. The difference between these two amounts of heat is the heat required by the stack to

make the reaction occur. The stack will have an endothermic behavior because the reduction of the current density increases the endothermicity of the system.

$$|Q_{th}| = |Q_{reaction}| - |Q_{irreversibilities}| \tag{106}$$

$$|Q_{reaction}| = \frac{T \cdot \Delta s_{react}}{F \cdot n_{f_{Fe}}} \cdot I \cdot n_{cell} = 314.14 \ \ W \tag{107}$$

$$|Q_{irreversibilities}| = I \cdot n_{cell} \cdot \sum_{j} \eta_j = 104\ W \tag{108}$$

$$|Q_{th}| = (V_{tn} - V) \cdot I \cdot n_{cell} = 210.14\ W \tag{109}$$

As expected, in order to produce the same amount of electrical power, the heat required by this configuration is much higher than the previous case.

However, since the stack has a higher volume than before, it will lose more heat through the external walls.

Therefore, for this configuration the efficiency is recalculated:

$$\eta = \frac{P_{produced}}{P_{required}} = \frac{1000}{1205.6} = 0.83 = 83\ \% \tag{110}$$

In this operation conditions the round-trip efficiency of the system has been enhanced from 61.7% to 83 %.

The difference of efficiency between the system with and without the PCM, would be higher than before because electrolysis mode is now more endothermic.

It is assumed that the heat required for the heater to sustain the reaction is ~2.5 times greater than the heat effectively needed by the stack, this number, as already explained in the section 4.1 Efficiency Analysis, has been chosen by referring to the first Comsol model in Figure 29; therefore, the efficiency of the system without the PCM would be:

$$\eta = \frac{P_{produced}}{P_{required} + Q_{heater}} = \frac{1000}{1205.6 + 2.5 \cdot 210} = 0.578 = 57.8\ \% \tag{111}$$

4.2.3 Model description

The new model geometry is represented in the following figure (Figure 47):

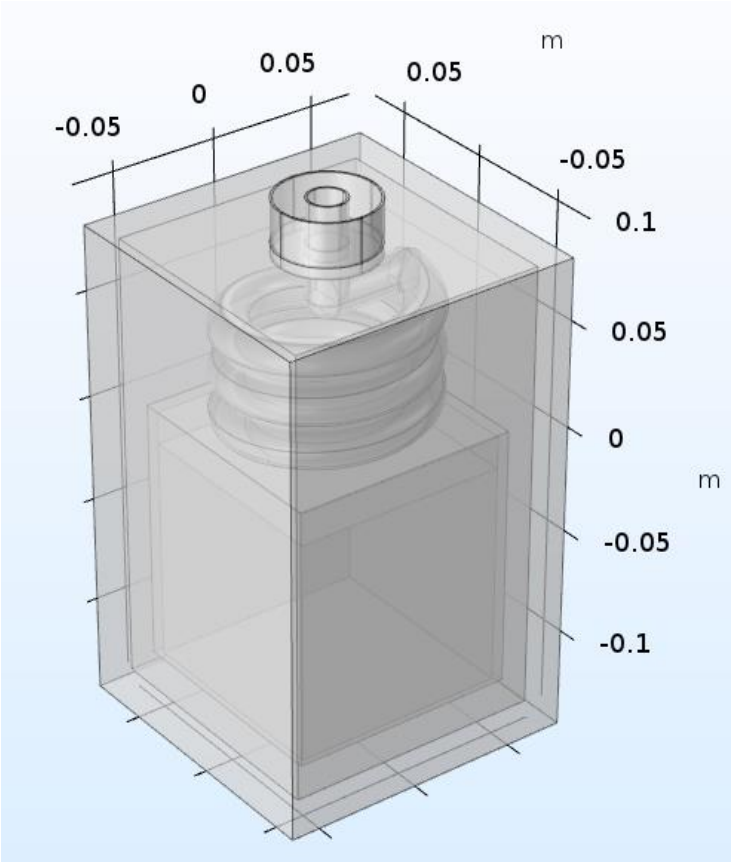

Figure 47 – 3-D geometry of the new configuration

The geometric parameters are the same of the previous model except for the height of the stack.

A heat source $Q_{stack-FC}$ has been put in the stack to simulate the exothermic behavior in fuel cell mode, and the same has been done for electrolysis mode with $Q_{stack-EL}$, but in this case the heat source is negative.

The material of the fluid is oxygen and the mass flow rate is just the stoichiometric amount needed for the reaction.

In fuel cell mode the fluid flow initial conditions have been set:

- $U_z = 1, U_x = 0,\ U_y = 0$ for the outer pipe and the outer channel of air
- $U_z = -1, U_x = 0,\ U_y = 0$ for the inner pipe (the helix) and the stack

The initial values of the temperature is 640 ℃ in the stack and PCM domain, the rest of the domains are set at 20℃.

In electrolysis mode the fluid flow physics the initial conditions have been set:

- $U_z = -1, U_x = 0,\ U_y = 0$ for the outer pipe and the outer channel of air
- $U_z = 1, U_x = 0,\ U_y = 0$ for the inner pipe (the helix) and the stack

The initial temperature of the PCM and of the stack has been imposed at 685℃, while the remaining geometry has initial condition of 20℃.

For both modes of operation the study is time dependent and it has been divided into two steps, each step studies only one physics, the scheme solver for both steps is fully coupled, the solver for the fluid flow physics is direct (MUMPS) and for the heat transfer is direct (PARDISO). In the time-dependent solver of the heat transfer in porous media the maximum size of the step has been fixed at 3 seconds.

Table 15 - Operating conditions for both FC and EL

Operating conditions		
Parameter	Value	Units
T_{in}	20	℃
T_a	20	℃
$\dot{m}_{in}$	8.62e-4	kg/s
$Overblow$	1	$-$
$h_{conv-FC}$	100	$\frac{W}{K \cdot m^2}$
$h_{conv-EL}$	20	$\frac{W}{K \cdot m^2}$
$Q_{stack-FC}$	418	W
$Q_{stack-EL}$	-210	W
$Fluid\ material: O_2$		
$Molar\ Weight$	32	$kg/kmol$

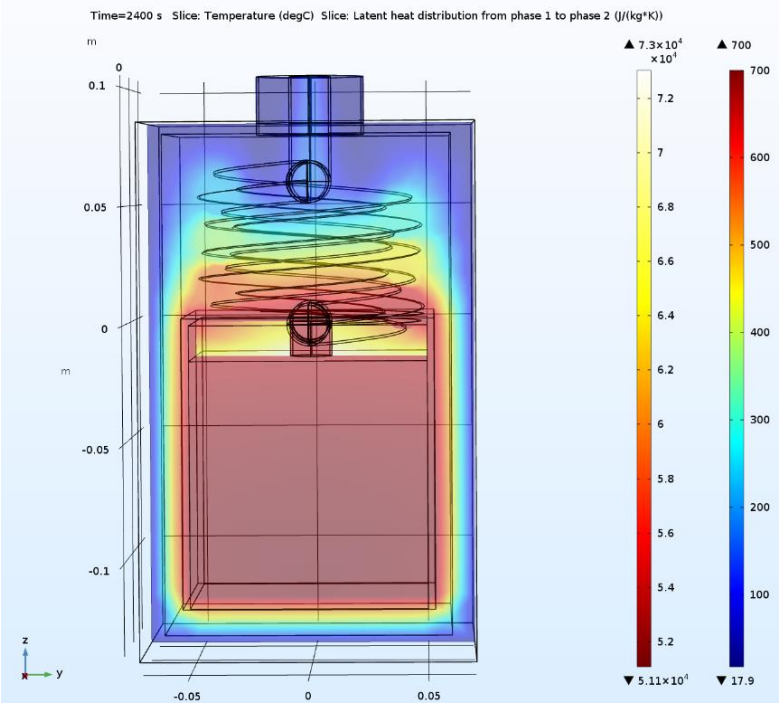

Figure 48 – Cross-section of the 3D model that shows the latent heat and the temperature distribution in FC

The figure above (Figure 48) shows the distribution of temperature and latent heat in the cross-section of the model, which work in FC mode of operation. The picture has been taken at 2400 s, because before the phase change there are 2000 s of transient in which the model first cools down and then it heats up again.

The heat is well exchanged and the temperature of the fluid at the outlet is ~150°C.

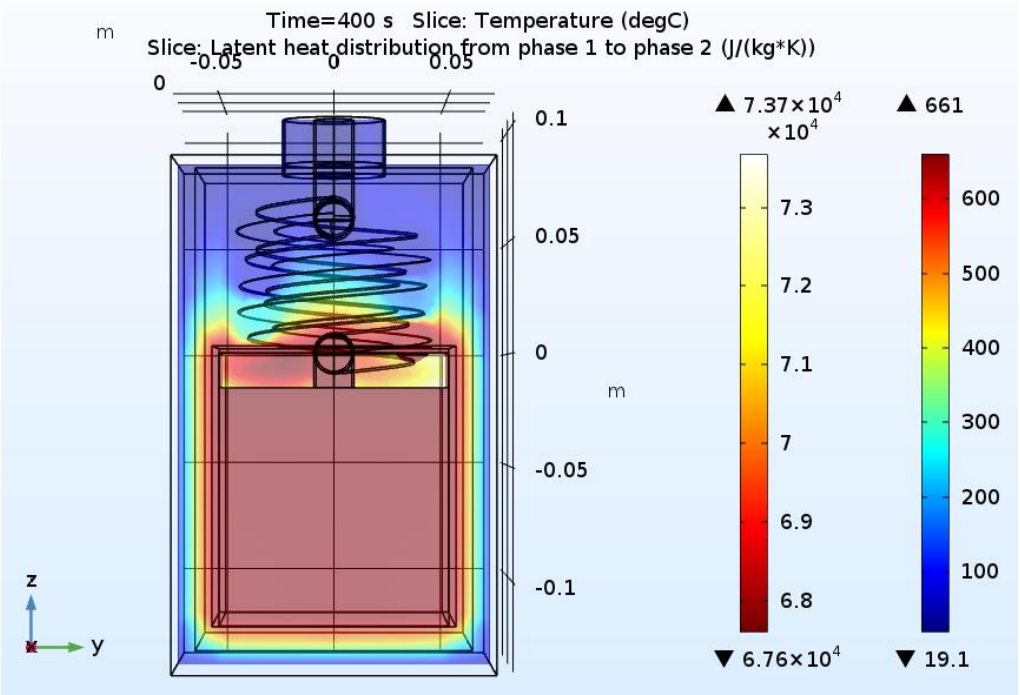

Figure 49 - – Cross-section of the 3D model that shows the latent heat and the temperature distribution in EL

In this image the model is working in electrolysis mode, in fact, as it is possible to see the maximum value of temperature corresponds to the melting point of fusion. In this model the air flows out at 20°C, so at ambient temperature, this means that all the heat has been exchanged.

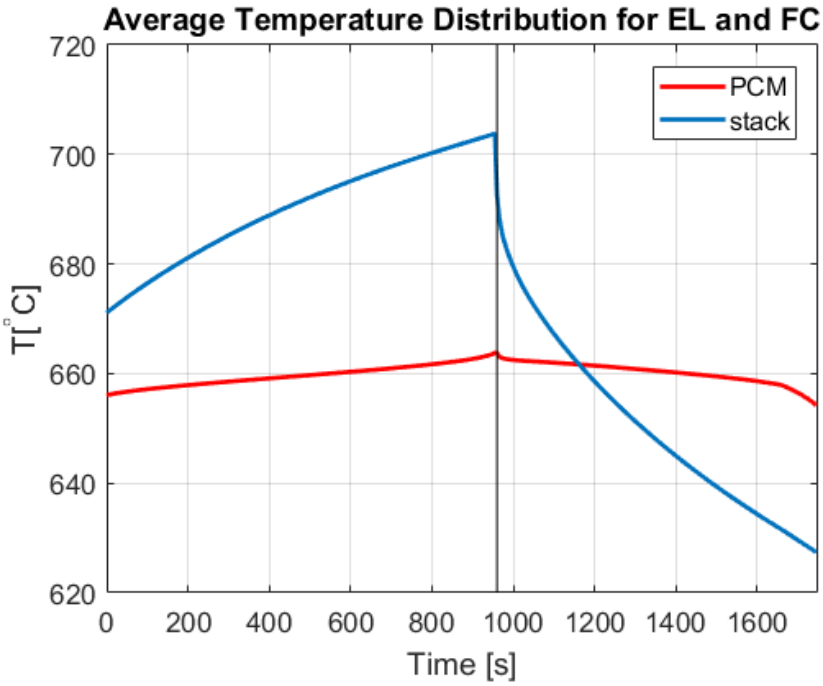

Figure 50 - Temperature variation over time during discharge and charge

In this graph (Figure 50) the PCM and the stack temperature are shown in the left part of the graph in discharge mode of operation of the battery, and in the right part in charge mode of operation. In this case the time of melting lasts 950 seconds instead the solidification lasts 785 seconds. As before (Figure 44), the simulation has not been performed reversibly, but two different simulations for each mode of operation have been ran and then put together in a single graph, in order to represent a discharge-charge cycle of reversible operation.

Moreover, the temperature of the stack in FC mode has a slope less steep than before because the heat released is less, contrariwise in EL mode the slope is steeper because the heat absorbed is much higher than before.

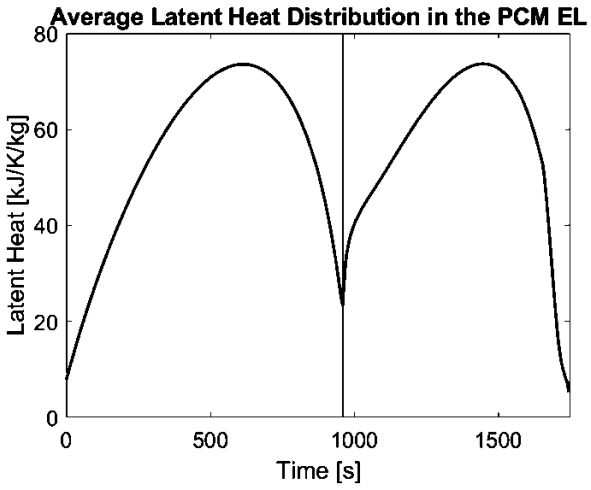

Figure 51 – Latent heat variation over time during discharge and charge

Figure 51 represents the variation of the latent heat in the PCM domain, the black line again splits the plot in two parts, the left curve is the melting phase and the right one is the solidification phase.

The power that is stored in the PCM is:

$$\phi_{stored} = Q_{latent} \cdot \bar{\rho} \cdot H \cdot S = 151.1\ kJ \tag{112}$$

$$Q_{stored} = \frac{\phi_{stored}}{\Delta t} = 159\ W \tag{113}$$

- Δt in this case it is equal to 950 seconds

The fraction of the heat released by the stack that is effectively absorbed:

$$heatfraction = \frac{Q_{stored}}{Q_{stack-FC}} = 0.38 = 38\ \% \tag{114}$$

As expected, this value is lower than the previous case because a higher amount of heat is lost through the walls around the stack.

For this reason, a further simulation has been done increasing the thickness of the insulation from 1 to 2 cm. Moreover, the material of the insulation, and therefore the thermal conductivity, has been changed, the silica aerogel has been used with a thermal conductivity of k=0.017 W/m/K, in order to reduce the heat losses towards the external walls

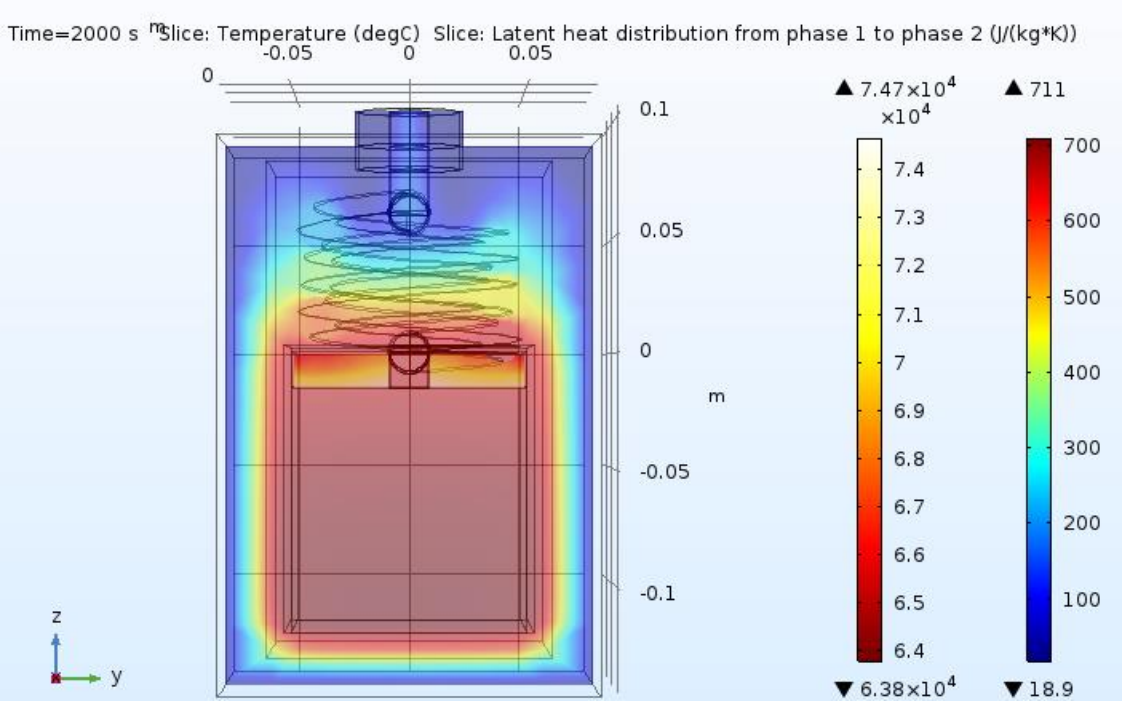

Figure 52 – Cross-section of the 3D model with the insulation thicker and with lower thermal conductivity that shows the latent heat and the temperature distribution in FC

The Figure 52 represents the temperature and the latent heat distribution in the model working in fuel cell mode, it is possible to see from the second column that the maximum temperature reached is 711 °C, so the stack is not overheated; the air that flows out is at ≈ 160 °C.

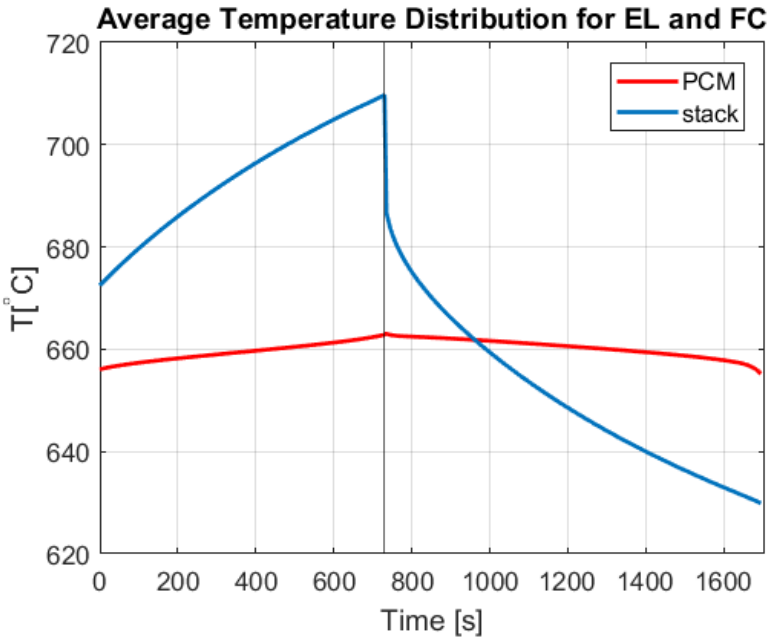

Figure 53 - Temperature variation over time during discharge and charge of the model with the insulation thicker and with lower thermal conductivity

In Figure 53 is represented the temperature in the PCM and the stack volume, the graphs is split in two parts by a black line: the left part corresponds to the fuel cell mode of operation, the right part to the electrolysis mode. As already explained, the plot in Figure 53 is the result of two different simulations that have been put together, in order to represent a discharge-charge cycle of reversible operation.

The phase change in fuel cell mode lasts 730 s, less than the model with weaker insulation because less heat is lost and then more heat is stored. The phase change in electrolysis mode lasts 965 s, more than before, and, moreover, the temperature decrease is less significant as expected.

The power stored in the PCM in this model:

$$Q_{stored} = \frac{\phi_{stored}}{\Delta t} = 207\ W \tag{115}$$

- Δt in this case it is equal to 730 seconds

The fraction of the heat released by the stack that is effectively absorbed by the PCM:

$$heatfraction = \frac{Q_{stored}}{Q_{stack-FC}} = 0.495 = 49.5\ \% \tag{116}$$

The heat fraction stored in this model, as expected, is increased with respect to the last model.

4.3 Sizing of the components

Finally, the amount of Aluminum phase change material and of Iron that is needed per hour of storage capacity, has been analyzed.

The power is the parameter linked to the RSOC that is maintained constant, the energy was varied by increasing the volume of iron and so the total enthalpy of the iron oxide reduction reaction. The ratio of the power of the stack and the energy stored by the Iron is the energy over power ratio and it determines the hours of storage capacity.

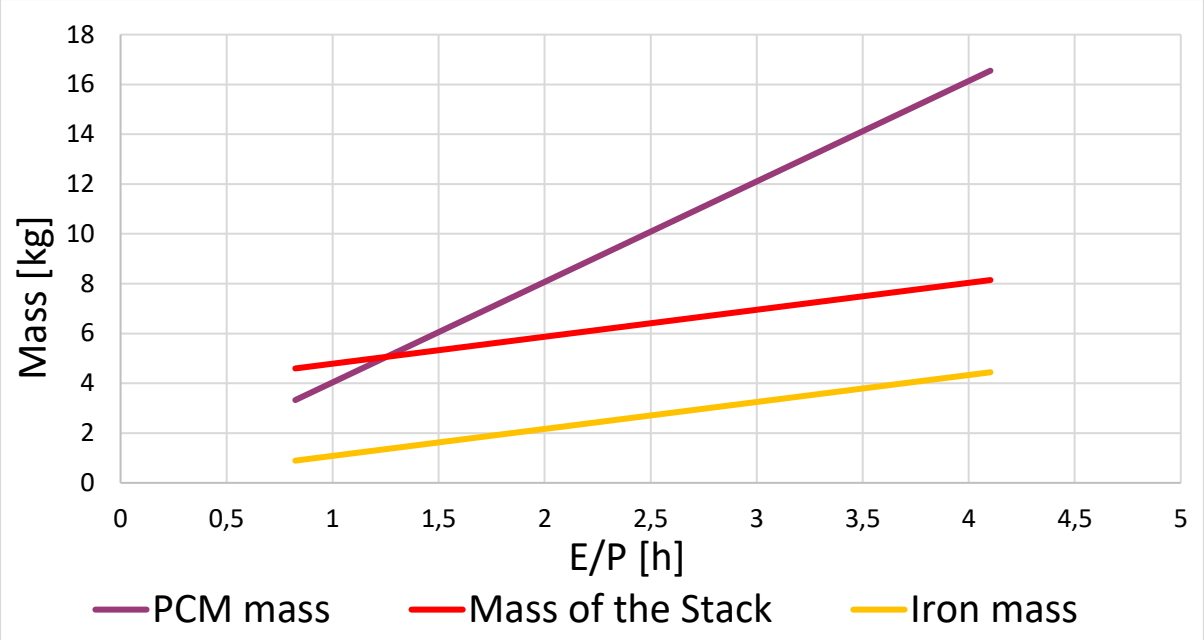

Figure 54 – PCM and Iron mass variation as a function of the energy over power ratio

As it is possible to notice from the plot above (Figure 54) the lines red and yellow, which corresponds to the Iron mass and to the mass of the stack, have the same slope. This is because the mass of the RSOC stack not including the Iron, is constant.

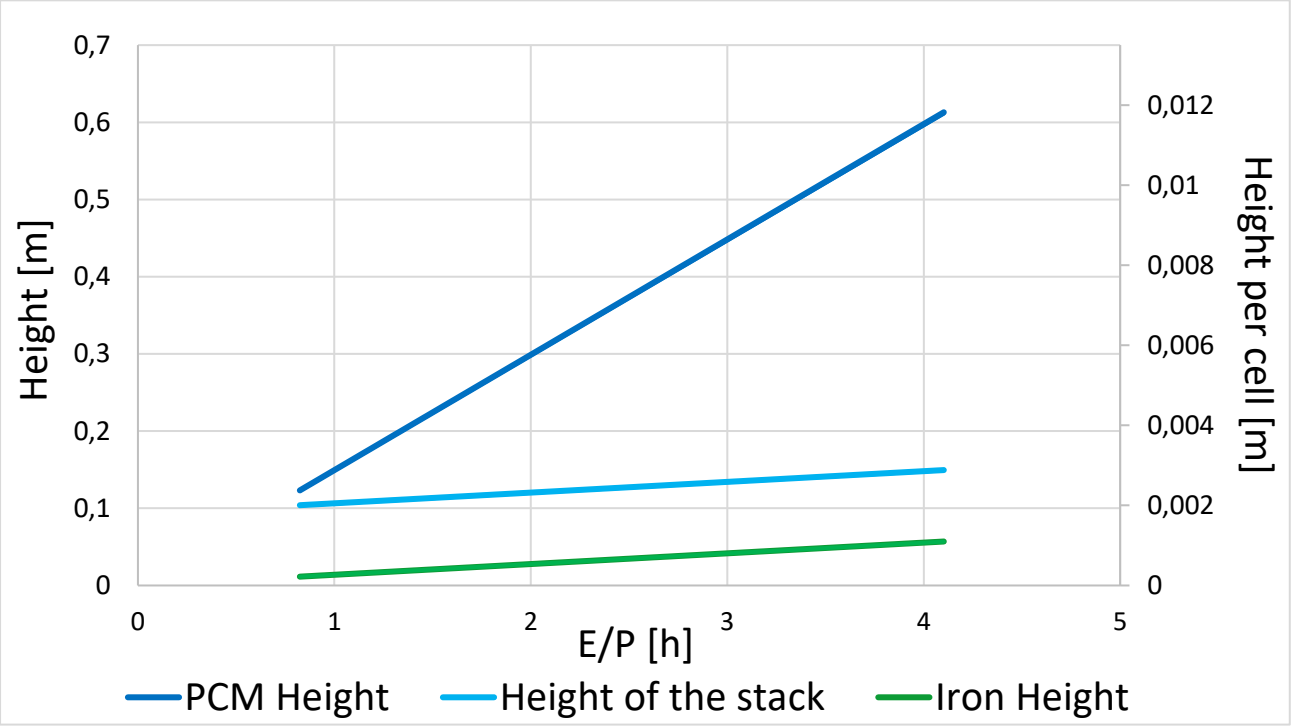

Figure 55 - PCM and Iron height as a function of the energy over power ratio

Figure 55 shows the PCM and Iron height, with the fixed footprint area of 100 cm^2. The left y-axis is the total height for a stack, and the right y-axis is the height for each cell. These graphs have been done for the operation conditions of the last configuration (i=0.2 A/cm^2, ncell=52). Clearly, the amount of Aluminum required is higher than that of the Iron. Moreover, the increase of the amount of Aluminum with the increment of the energy over power ratio is much more significant, in fact, in the graph the slope of the curve is steeper than the Iron one.

Afterwards, the cost of Iron and Aluminum per kWh of storage capacity has been calculated. The average cost of Aluminum plates it has taken equal to 4.05 $/kg [25]. For the electric storage medium, it has been looked for the cost of an iron oxide, Fe_2O_3, and the average cost has been taken equal to 1.3 $ / kg [26].

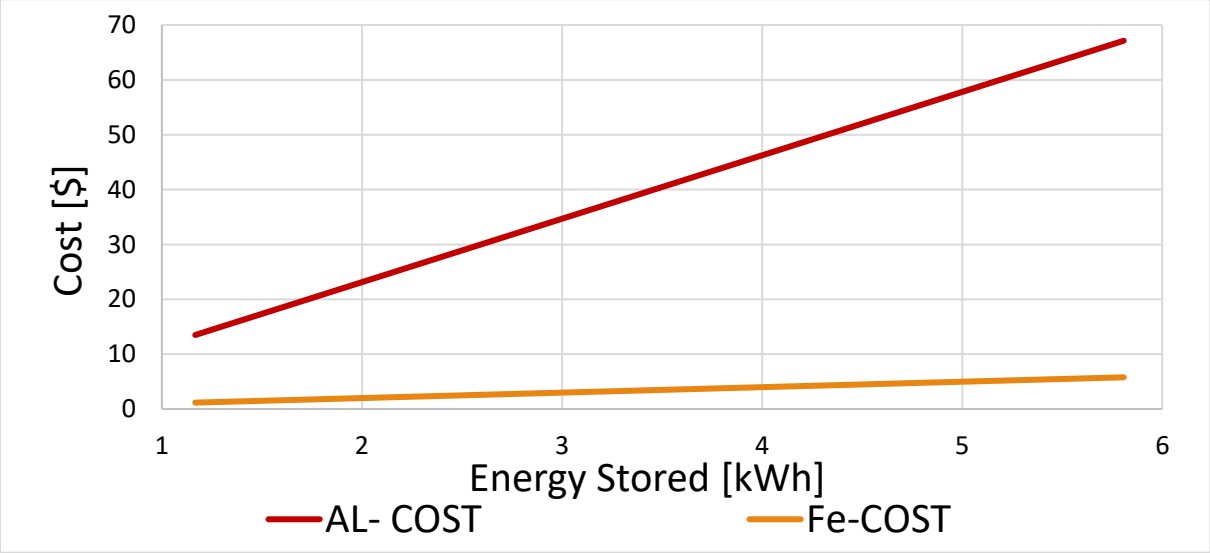

Figure 56 – Cost of the Aluminum and the Iron per kWh stored

Cost of Aluminum is higher than that of the Iron, and, as shown in Figure 54, a larger amount of PCM is needed with respect to the Iron. For these reasons, in Figure 56, the Aluminum cost is much more impactful than that of the Iron, which is not significantly changing with the variation of the energy stored.

The cost per kWh of storage capacity is a constant value, for the Aluminum is equal to 11.56 $ / kWh, and for the Iron oxide is equal to 0.994 $ / kWh.

5. CONCLUSIONS

The theme of this thesis was the integration of a latent thermal storage to a high temperature rechargeable oxide battery comprised of a RSOC stack and a bed of Iron/Iron oxide as thermochemical storage medium. The goal was to build a 3D Multiphysics model and use it to design a battery system that could store electrical energy with high round-trip efficiency.

The model built is a compact system in an insulated box constituted by the stack, the thermal storage and a heat exchanger. Therefore, the balance of plant has been minimized using a simple heat exchanger and integrating the heat storage (the PCM) in direct contact with the stack, which is the heat sink or source depending on the mode of operation.

Firstly, a system without PCM was designed to be able to work in both modes of operation (fuel cell and electrolysis), and, after that, to study the tradeoffs in operation and system design. In fact, the model should keep the heat inside the system during the endothermic and isothermal periods, for this reason, an electric heater has been built-in, which supplies heat if the stack is operating in endothermic or idle mode. In this operating conditions the use of insulation is recommended in order to keep the system hot. On the other hand, the system should shed the heat during exothermic operating mode, in order to not overheat the stack, this is made by using a thin insulation and by letting the heat out by overblowing. Parametric studies have been performed in order to design the best configuration in terms of geometry and operating conditions; after that, it is possible to say that the strongest parameter able to cool the system in fuel cell mode is the overblow.

Integrating the PCM instead of the heater, the overblow could be eliminated in fuel-cell (discharge) mode. Otherwise the oxygen overblow needed to be 40 times higher to provide sufficient cooling. This reduction in overblow was possible because the PCM absorbs and stores the heat generated; this means lower cost for feeding the pump because there is no need to overblow.

Moreover, with the phase change material, the round-trip efficiency increased from 58% to 83%, considering that all the heat needed by the electrolysis is supplied by the PCM, and this seems to be a big improvement for the system. On the other hand, in the last configuration the heat captured in the PCM during fuel cell mode was only the 50 % of the heat released by the

stack, because the rest goes out through insulation and gas outlet, for this reason a better insulation should be added in the last model. Instead, in the model with a more compact stack operating at higher current density, the fraction of heat stored was 85 %.

Finally, the amount of Iron and Aluminum needed per hour of storage capacity was analyzed, and it has been noticed that the increase of the quantity of Aluminum is much more significant than that of the Iron, e.g. in order to have 3 hours of storage capacity, 3.3 kg of Iron and 12.5 kg of Aluminum are needed.
Moreover, Iron is also cheaper than Aluminum, and since the amount of Aluminum needed is higher, the Iron cost is almost negligible; in fact, the cost per kWh storage capacity for the Aluminum is equal to 11.56 $ / kWh, and for the Iron oxide is equal to 0.994 $ / kWh; this means that 92% of the cost comes from the Aluminum. For this reason, using a cheaper material as PCM, could be an interesting improvement of the system.

5.1 Future Work

In this project there is more than one aspect that should be improved.

First of all, in the last model, with higher efficiency and higher insulation, the storage capacity is very short (≈ 10 min), so upscaling the PCM would be necessary to increase the storage capacity, and so to have a longer duration storage.

Moreover, in the last section, a comparison of the cost between Aluminum and Iron has been done, but it would be interesting to understand how heavy is the impact of the cost of these two materials over the whole cost, therefore do an economic analysis and understand the feasibility and the percentage of success of the system in the market.

Furthermore, if the Aluminum has a strong impact on the whole cost of the system, it would be interesting to perform an analysis with a cheaper PCM, like $MgCl_2$, increasing its thermal conductivity combining it with a higher thermal conductivity material.

Eventually, a further research topic could be to study a new configuration of the system in order to decrease the variation of the temperature between fuel cell and electrolysis mode, making the stack more isothermal.

6. REFERENCES

[1] H. Ohmori, S. Uratani, and H. Iwai, “Numerical simulation of gas diffusion effects on charge/discharge characteristics of a solid oxide redox flow battery,” *J. Power Sources*, vol. 208, pp. 383–390, 2012.

[2] H. Ohmori and H. Iwai, “2-D Simulation of Heat and Mass Transfer Effects on Charge/Discharge Characteristics of a Solid Oxide Redox Flow Battery,” *ECS Trans.* , vol. 57, no. 1, pp. 233–242, 2013.

[3] X. Jin, X. Zhao, and K. Huang, “A high-fidelity multiphysics model for the new solid oxide iron-air redox battery part I: Bridging mass transport and charge transfer with redox cycle kinetics,” *J. Power Sources*, vol. 280, pp. 195–204, 2015.

[4] C. M. Berger *et al.*, “Calcium-Iron Oxide as Energy Storage Medium in Rechargeable Oxide Batteries,” *J. Am. Ceram. Soc.*, vol. 99, no. 12, pp. 4083–4092, 2016.

[5] W. W. Drenckhahn *et al.*, “A Novel High Temperature Metal - Air Battery,” *ECS Trans.* , vol. 50, no. 45, pp. 125–135, 2013.

[6] N. Xu, X. Li, X. Zhao, J. B. Goodenough, and K. Huang, “A novel solid oxide redox flow battery for grid energy storage,” *Energy Environ. Sci.*, vol. 4, no. 12, p. 4942, 2011.

[7] C. M. Berger *et al.*, “Development of storage materials for high-temperature rechargeable oxide batteries,” *J. Energy Storage*, vol. 1, no. 1, pp. 54–64, 2015.

[8] L. S. W. Brauna, V. Erfurt, F. Thaler, N. H. Menzler, R. Spatschek, “Kinetic Study of Iron Based Storage Materials for the Use in Rechargeable Oxide Batteries (ROB),” vol. 75, no. 43, pp. 59–73, 2017.

[9] X. Jin, X. Zhao, J. Tong, F. Yasmeen, R. E. White, and K. Huang, “Energy efficiency of an

intermediate-temperature solid oxide iron-air redox battery," *J. Energy Storage*, vol. 3, pp. 1–9, 2015.

[10] X. Jin and K. Huang, "Multiphysics modeling of solid-oxide iron–air redox battery: analysis and optimization of operation and performance parameters," *Sci. Bull.*, vol. 61, no. 17, pp. 1345–1354, 2016.

[11] H. Ohmori, H. Iwai, K. Itakura, M. Saito, and H. Yoshida, "Numerical prediction of system round-trip efficiency and feasible operating conditions of small-scale solid oxide iron-air battery," *J. Power Sources*, vol. 309, pp. 160–168, 2016.

[12] X. Jin, X. Zhao, C. Zhang, R. E. White, and K. Huang, "Computational Analysis of Performance Limiting Factors for the New Solid Oxide Iron-air Redox Battery Operated at 550 °C," *Electrochim. Acta*, vol. 178, pp. 190–198, 2015.

[13] S. Kasai, "Hydrogen electrical energy storage by high-temperature steam electrolysis for next-millennium energy security," *Int. J. Hydrogen Energy*, vol. 39, no. 36, pp. 21358–21370, 2014.

[14] W. Zhao *et al.*, "High temperature calorimetry and use of magnesium chloride for thermal energy storage," *Renew. Energy*, vol. 50, pp. 988–993, 2013.

[15] Hasnain S.M., "Review on sustainable thermal energy storage technologies, Part I: heat storage materials and techniques," *Energy Convers. Manag.*, vol. 39, no. 11, pp. 1127–1138, 1998.

[16] A. Rubin and D. C. Davide, "L'Accumulo Dell'Energia Termica: Stato Dell'Arte E Studio Di Sistemi E Soluzioni Per La Media Temperatura," 2012.

[17] A. Kylili, M. Theodoridou, I. Ioannou, and P. A. Fokaides, "Numerical heat transfer analysis of Phase Change Material (PCM) -enhanced plasters," pp. 1–7, 2016.

[18] M. Sensoli, J. Steinar, F. Rinaldi, and P. V. Hendriksen, “Power to gas to power conversion systems with thermal energy storage , possible applications for reversible Solid Oxide Cells,” 2015.

[19] J. P. Verma, “why counter current flow heat exchanger is better than co-current flow heat exchanger,” 2016. [Online]. Available: https://www.quora.com/profile/Jai-Prakash-Verma-JP/Posts/why-counter-current-flow-heat-exchanger-is-better-than-co-current-flow-heat-exchanger.

[20] Comsol Multiphysics, “Modeling Materials through a Phase Transition: Using COMSOL Multiphysics and Applying Physics First Principles Techniques,” *Comsol.Com*, 2007.

[21] V. Farolfi Mauro Bruno Correlatore and I. Marco Guerzoni, “Simulazione e misura della dispersione del calore in una scheda elettronica di front-end per rivelatori di fisica nucleare -Sessione II,” 2009.

[22] L. D. Solomon, “The Use of Sodium Chloride & Aluminum as Phase Change Materials for High Temperature Thermal Energy Storage Characterized by Calorimetry The Use of Sodium Chloride & Aluminum as Phase Change Materials for High Temperature Thermal Energy Storage Characteri,” 2013.

[23] D. Singh, T. Kim, W. Zhao, W. Yu, and D. M. France, “Development of graphite foam infiltrated with MgCl2for a latent heat based thermal energy storage (LHTES) system,” *Renew. Energy*, vol. 94, pp. 660–667, 2016.

[24] Massimo Santarelli, Dispense del corso: “Polygeneration and advanced energy systems” , Politecnico di Torino, 2016.

[25] http://zyaluminum.com/Mill-Aluminum-Plate-54-124-1.html, Jinan Zhaoyang

[26] https://www.alibaba.com/showroom/iron-oxide-brown-686.html

APPENDIX

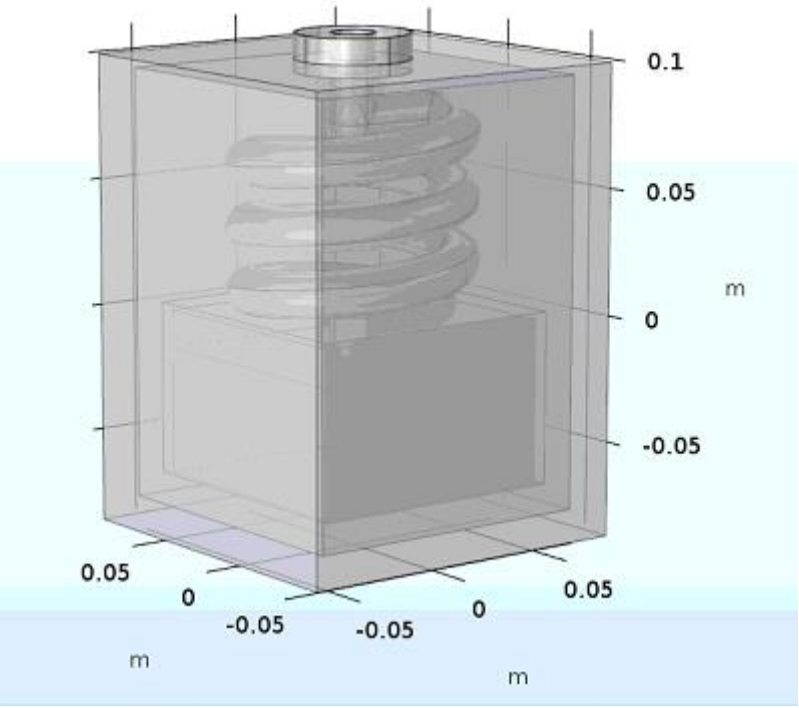

Figure A.1- Model with the pipes of the helix more detached from each other57

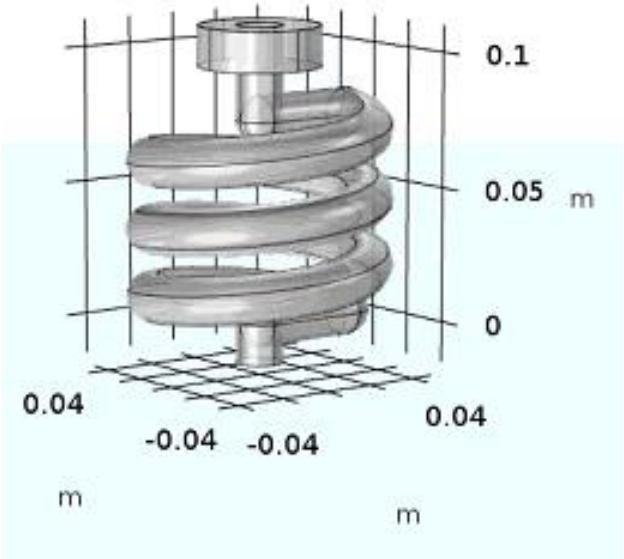

Figure A.1- The helix with the pipes more detached from each other58